

*The higher the hill
The harder the climb
The better the view*

Members of the jury

Prof. dr. S. Hendrix, Universiteit Hasselt, Diepenbeek, Belgium, *chairman*

Prof. dr. M. Ameloot, Universiteit Hasselt, Diepenbeek, Belgium, *promoter*

Prof. dr. I. Lambrichts, Universiteit Hasselt, Diepenbeek, Belgium, *co-promoter*

Prof. dr. J.-M. Rigo, Universiteit Hasselt, Diepenbeek, Belgium

Prof. dr. L. Michiels, Universiteit Hasselt, Diepenbeek, Belgium

Prof. dr. M. Nesladek, Universiteit Hasselt, Diepenbeek, Belgium

Prof. dr. P. Vanden Berghe, Katholieke Universiteit Leuven, Leuven, Belgium

Prof. dr. J. B. Phillips, University College London, London, United Kingdom

Dr. W. Martens, Universiteit Hasselt, Diepenbeek, Belgium

Preface

The human body is amazing. It is continuously processing information from the environment, balancing energy levels, fighting infections, and so much more. From the smallest molecule to interacting systems, each part contributes to overall functioning and harmony. Even though the body possesses an impressive capacity to heal itself, there are limitations. In order to overcome these restrictions, experts from different disciplines have been operating hand in hand to rebuild tissues and organs. What was considered science fiction a few decades ago is becoming reality today. From artificial skin to blood vessels and cartilage, the field of tissue engineering is rapidly evolving from bench to bedside.

In this dissertation, a novel cell-based tissue engineering approach to facilitate peripheral nerve regeneration is discussed. The theoretical background of peripheral nerve injury and the choice for human dental pulp stem cells (hDPSCs) and collagen type I hydrogels as a basis for artificial nerve conduits is reviewed and justified in the general introduction. The following four chapters elaborate on specific aspects of the development and implementation of this engineered neural tissue, from the molecular to the tissue level with both standard and advanced label-free microscopy techniques. Finally, in the general discussion all the findings are combined and put in perspective to answer the proposed research questions.

Table of Contents

Preface	I
Table of Contents	III
List of Figures	VIII
List of Tables	X
List of Abbreviations	XI

Chapter 1 Introduction and Aims **1**

1.1 Peripheral nervous system	2
1.1.1 Schwann cell development	2
1.1.2 Peripheral nerve injury	4
1.2 Mesenchymal stem cells	8
1.2.1 Dental pulp stem cells	8
1.3 Role of DPSCs in neural regeneration	13
1.3.1 DPSCs for CNS repair	13
1.3.2 DPSCs for PNS repair	17
1.4 Scaffolds for neural tissue engineering	18
1.4.1 Hydrogels	18
1.4.2 Cell-matrix interactions	21
1.5 Label-free optical imaging	23
1.5.1 Two-photon excitation autofluorescence	23
1.5.2 Second harmonic generation	24
1.6 Aims of the study	26

Chapter 2 In vitro differentiation of human dental pulp stem cells into Schwann cells **29**

2.1 Abstract	30
2.2 Introduction	31
2.3 Materials and methods	33
2.3.1 Materials and products	33
2.3.2 Isolation and differentiation of hDPSCs into Schwann-like cells	33

IV

2.3.3	Collection of conditioned medium	33
2.3.4	Isolation of primary Schwann cells	34
2.3.5	Immunocytochemistry	34
2.3.6	Ultrastructural analysis: transmission electron microscopy (TEM)	35
2.3.7	Enzyme-linked immunosorbent assay (ELISA)	35
2.3.8	Neonatal dorsal root ganglion (DRG) neuron cell cultures: 2-dimensional (2D) experiments	35
2.3.9	Survival assay	36
2.3.10	Neurite regeneration assay	36
2.3.11	Adult DRG cell cultures: 3-dimensional (3D) experiments	36
2.3.12	Myelination in hydrogel	37
2.3.13	TEM of cellular hydrogels	37
2.3.14	Generation of EngNT using d-hDPSCs	37
2.3.15	Seeding of dissociated DRG neurons on top of EngNT	38
2.3.16	Analysis of angle of deviation	38
2.3.17	Statistical analysis	38
2.4	Results	40
2.4.1	Morphology and immunophenotype of d-hDPSCs <i>in vitro</i>	40
2.4.2	Secretion of neurotrophic factors by hDPSCs and d-hDPSCs	42
2.4.3	d-hDPSCs are aligned in EngNT and guide neurite outgrowth <i>in vitro</i>	44
2.4.4	Ultrastructural evaluation of myelination capacity of d-hDPSCs	45
2.5	Discussion	48

Chapter 3 The potential of Schwann cell differentiated human dental pulp stem cells as a treatment for peripheral nerve injury 53

3.1	Abstract	54
3.2	Introduction	55
3.3	Materials and methods	58
3.3.1	Materials and products	58
3.3.2	Cell culture in 2D and 3D	58
3.3.3	Collection of conditioned medium and ELISA	58

3.3.4	Alamar Blue cell proliferation assay	59
3.3.5	Transwell migration assay	59
3.3.6	Tube formation assay	60
3.3.7	Preparation of EngNT containing d-hDPSCs	60
3.3.8	Surgical repair of rat sciatic nerve	61
3.3.9	Transmission electron microscopy	61
3.3.10	Immunostaining	62
3.3.11	Confocal microscopy	62
3.3.12	Statistical analysis	63
3.4	Results	64
3.4.1	Expression of VEGF-A by hDPSCs and d-hDPSCs <i>in vitro</i>	64
3.4.2	Angiogenic properties of d-hDPSCs <i>in vitro</i>	64
3.4.3	Nerve repair	68
3.4.4	Blood vessels and myelin	70
3.5	Discussion	73

Chapter 4 Label-free mapping of microstructural organization in cellular hydrogels using ICS **77**

4.1	Abstract	78
4.2	Introduction	79
4.3	Materials and methods	82
4.3.1	Materials and products	82
4.3.2	Cell culture	82
4.3.3	Aligned cellular hydrogels	82
4.3.4	Hydrogel contraction assay	83
4.3.5	Microscopy	83
4.3.6	ACF analysis	84
4.3.7	Validation of ICS analysis for orientation parameters κ and μ	86
4.3.8	Statistical analysis	86
4.4	Results	87
4.4.1	Differential hydrogel contraction on macro and micro scale	87
4.4.2	Validation of orientation parameters	89

4.4.3	Local changes in hydrogel architecture during cell-mediated alignment	92
4.5	Discussion	94
4.6	Supplementary figure	98

Chapter 5	Molecular mechanisms of collagen type I hydrogel contraction by hDPSCs and d-hDPSCs	99
------------------	--	-----------

5.1	Abstract	100
5.2	Introduction	101
5.3	Materials and methods	103
5.3.1	Materials and products	103
5.3.2	Isolation, culture and differentiation of hDPSCs	103
5.3.3	Collagen contraction assay	103
5.3.4	Isolation of primary Schwann cells	103
5.3.5	RNA extraction and RT-PCR	103
5.3.6	Immunocytochemistry	104
5.3.7	Western blot	106
5.3.8	Inhibition hydrogel contraction	107
5.3.9	Statistical analysis	108
5.4	Results	109
5.4.1	Differential contraction of collagen type I hydrogels by hDPSCs and d-hDPSCs	109
5.4.2	Expression of integrins by hDPSCs and d-hDPSCs at mRNA level	110
5.4.3	Expression of integrins by hDPSCs and d-hDPSCs at protein level	111
5.4.4	Integrin β 1 plays a major role in the contraction process of hDPSCs and d-hDPSCs in a collagen type I hydrogel	114
5.5	Discussion	116

Chapter 6	General discussion and outlook	121
------------------	---------------------------------------	------------

	Can hDPSCs differentiate toward Schwann cells in vitro?	124
--	---	-----

Does EngNT containing d-hDPSCs promote peripheral nerve regeneration <i>in vivo</i> ?	127
Can SHG microscopy and ICS analysis be used to map local changes in self-aligning cellular collagen type I hydrogels?	128
What is the contractile capacity of hDPSCs and d-hDPSCs and which integrins are involved?	129
Conclusion	130
Chapter 7 Nederlandse samenvatting	133
<hr/>	
Kunnen hDPSCs <i>in vitro</i> differentiëren tot Schwann cellen?	135
Wordt perifeer zenuwherstel bevorderd door EngNT dat d-hDPSCs bevat?	138
Kunnen <i>second harmonic generation</i> (SHG) microscopie en <i>image correlation spectroscopy</i> (ICS) analyse gebruikt worden om lokale veranderingen in zelfalignerende cellulaire collageen type I hydrogelen in kaart te brengen?	140
Wat is de contractiele capaciteit van hDPSCs en d-hDPSCs en welke integrines zijn hierin betrokken?	141
Algemene conclusie	142
Reference list	143
Curriculum Vitae	163
Dankwoord	169

List of Figures

Figure 1.1	The Schwann cell lineage	3
Figure 1.2	Wallerian degeneration and nerve regeneration following PNI	5
Figure 1.3	Structure of fibrillary collagen	19
Figure 1.4	Two-photon excitation autofluorescence (TPEA) and second harmonic generation (SHG)	23
Figure 2.1	Phenotyping hDPSCs after Schwann cell differentiation	39
Figure 2.2	Ultrastructural characteristics of hDPSCs and d-hDPSCs	40
Figure 2.3	Neurotrophic factor secretion by hDPSCs and d-hDPSCs	41
Figure 2.4	d-hDPSC alignment in EngNT guides neurite outgrowth in coculture	43
Figure 2.5	Ultrastructural analysis of myelination capacity of d-hDPSCs	44
Figure 3.1	Expression of the angiogenic factor VEGF-A by hDPSCs and d-hDPSCs <i>in vitro</i>	61
Figure 3.2	Effect of hDPSCs and d-hDPSCs on endothelial cell proliferation	62
Figure 3.3	Effect of hDPSCs and d-hDPSCs on endothelial cell migration	63
Figure 3.4	Effect of hDPSCs and d-hDPSCs on endothelial tubulogenesis	64
Figure 3.5	Quantification of nerve repair by repair devices and allografts	66
Figure 3.6	Comparison of number of blood vessels and myelinated fibers	68
Figure 4.1	Hydrogel contraction assay with hDPSCs or d-hDPSCs	86
Figure 4.2	Validation of ICS analysis of SHG images to quantify fibril orientation	89
Figure 4.3	Detection of local changes in cell-mediated hydrogel alignment by ICS analysis	91

Figure 4.4	Centre versus edge microstructural changes during hydrogel contraction	96
Figure 5.1	Hydrogel contraction profile for hDPSCs and d-hDPSCs	107
Figure 5.2	Expression of integrins by hDPSCs and d-hDPSCs at mRNA level	108
Figure 5.3	Expression of collagen type I binding integrins $\alpha 1$, $\alpha 2$ and $\beta 1$ in hDPSCs and d-hDPSCs	110
Figure 5.4	Differential expression of the collage type I binding integrin subunits $\alpha 1$, $\alpha 11$ and $\beta 1$ after differentiation	111
Figure 5.5	Effect of integrin $\alpha 1$ or $\beta 1$ inhibition on hydrogel contraction by hDPSCs and d-hDPSCs	113

List of Tables

Table 1.1	Therapeutic applications of dental pulp (stem) cells for nerve repair	14
Table 5.1	RT-PCR protocol	103
Table 5.2	Overview of primers used for RT-PCR	103
Table 5.3	Overview of primary and secondary antibodies used for immunocytochemistry	104
Table 5.4	Overview of primary and secondary antibodies used for western blot	105
Table 5.5	Overview of blocking antibodies and isotype controls used for inhibition of hydrogel contraction	106
Table 6.1	<i>In vitro</i> morphological, ultrastructural, cytochemical and functional properties of hDPSCs and d-hDPSCs compared to repair Schwann cells.	121
Table 6.2	Functional properties of d-hDPSCs in EngNT in vitro and in vivo	124

List of Abbreviations

2D	two-dimensional
3D	three-dimensional
α MEM	minimal essential medium, alpha modification
ACF	autocorrelation function
BDNF	brain-derived neurotrophic factor
b-FGF	basic fibroblast growth factor
b-NGF	nerve growth factor beta
BME	β -mercaptoethanol
CNS	central nervous system
d-hDPSCs	human dental pulp stem cells differentiated toward Schwann cells
DAPI	4',6-diamidino-2-phenylindole
DMEM	Dulbecco's modified Eagle medium
DMSO	dimethyl sulfoxide
DRG	dorsal root ganglion
ECM	extracellular matrix
EngNT	engineered neural tissue
ELISA	enzyme-linked immunosorbent assay
FBS	fetal bovine serum
GDNF	glial-derived neurotrophic factor
GFAP	glial fibrillary acidic protein
hDPSCs	human dental pulp stem cells
ICS	image correlation spectroscopy
MBP	myelin basic protein
MFI	mean fluorescence intensity
MSCs	mesenchymal stem cells
NCCs	neural crest cells
NGF	nerve growth factor
NFs	neurotrophic factors
NRG	neuregulin1
NT-3	neurotrophin 3
P	postnatal

p0	protein zero
p75NTR	p75NTR neurotrophin receptor
PBS	phosphate buffered saline
PDGFaa	platelet-derived growth factor AA
PFA	paraformaldehyde
PLL	poly-L-lysine
PLP	proteolipid protein
PNI	peripheral nerve injury
PNS	peripheral nervous system
RA	all <i>trans</i> -retinoic acid
RT	room temperature
RT-PCR	reverse-transcription polymerase chain reaction
S100s	S100 calcium binding protein
SCPs	Schwann cell precursors
SEM	standard error of mean
SHG	second harmonic generation
SOX10	SRY (Sex Determining Region Y)-Box 10
TEM	transmission electron microscopy
TPEA	two-photon excitation autofluorescence
VEGF	vascular endothelial growth factor

Chapter 1

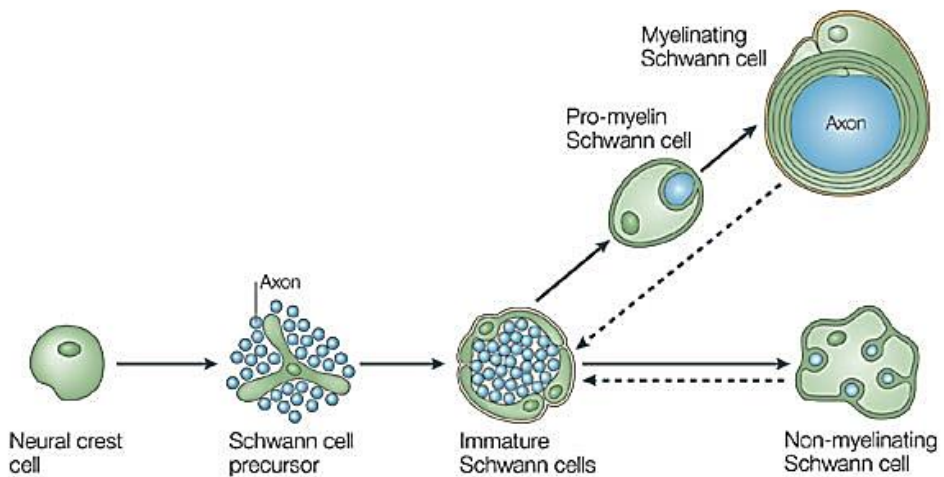
Introduction and Aims

1.1 Peripheral nervous system

The peripheral nervous system (PNS) connects the central nervous system (CNS), namely the brain and spinal cord, to the rest of the body via ganglia and sensory and motor nerves. In general, these nerves are composed of three connective tissue sheaths that provide support and protection: the epineurium, perineurium and endoneurium [1]. The epineurium is the outermost layer comprised of loose connective tissue and blood vessels to supply the nerve. It envelops the nerve and has extensions that encompass the fascicle. Each fascicle is enclosed by a ring of dense perineurium, which consists of an inner layer of perineurial cells and an outer layer of organized collagen fibres. The innermost sheath, the endoneurium, is built out of loose vascular connective tissue (primarily collagen type I), fibroblasts and extracellular fluid, occupying the space between the nerve fibres within the fascicle. Inside these endoneurial tubules, axons are accompanied by Schwann cells, that either myelinate or just surround the axon [1, 2].

1.1.1 Schwann cell development

Schwann cells are the main glial cells of the PNS and are crucial for normal nerve function. An overview of the Schwann cell lineage is given in Figure 1.1. They develop from neural crest cells (NCCs), which emerge at the dorsal part of the closing neural tube during vertebrate embryogenesis. Depending on their migratory track, neural crest cells give rise to for example neurons, melanocytes, fibroblasts, smooth muscle cells and glial cells. Although the mechanisms of this glial differentiation from neural crest cells are poorly understood, the factors SRY (Sex Determining Region Y)-Box 10 (SOX10) and neuregulin 1 (NRG1) are implicated in this process [3]. The resulting Schwann cell precursors (SCPs) differ from NCCs in three main ways: (i) SCPs are associated with axons instead of the extracellular matrix (ECM), (ii) SCPs express other markers such as Cadherin 19, protein zero (P0) and proteolipid protein (PLP) and (iii) SCPs respond differently to a variety of factors involved in cell survival, proliferation and differentiation. SCPs provide essential neurotropic support and are important for normal fasciculation. The conversion of SCPs to immature Schwann cells occurs later in embryonic development and is thought to be regulated by factors such as integrin



Copyright © 2005 Nature Publishing Group
Nature Reviews | Neuroscience

Figure 1.1: The Schwann cell lineage. Schematic illustration of the main cell types and developmental transitions involved in Schwann cell development. Reprinted by permission from Macmillan Publishers Ltd: *Nature Reviews Neuroscience*, Jessen *et al.* [4], Copyright © 2005.

β 1, laminin and p75NTR [4]. Along with increased proliferation, immature Schwann cells are characterized by the expression of S100 calcium binding protein (S100), glial fibrillary acidic protein (GFAP) and the secretion of autocrine survival signals such as insulin-like growth factor 2, neurotrophin 3 (NT-3), platelet-derived growth factor- β , leukaemia inhibitory factor and lysophosphatidic acid [4]. In presence of a basal lamina, irregular axon-Schwann cell bundles are surrounded by blood vessels and ECM. The fate of these immature Schwann cells lies in the size of the axons with which they associate. During a process called radial sorting, immature Schwann cells segregate axons based on their diameter. While multiple small diameter axons are loosely ensheathed by mature non-myelinating Schwann cells or Remak cells, large diameter axons ($>1 \mu\text{m}$ in diameter) associate in a 1:1 ratio with pro-myelinating Schwann cells that set the stage for the formation of a multi-layered myelin sheet, thereby becoming myelinating Schwann cells. A most remarkable feature of these mature Schwann cells is that their differentiation

states are reversible, i.e. they can dedifferentiate into immature Schwann cells. The PNS benefits from this adult plasticity of Schwann cells as this enables regeneration of peripheral nerves following injury [3-7].

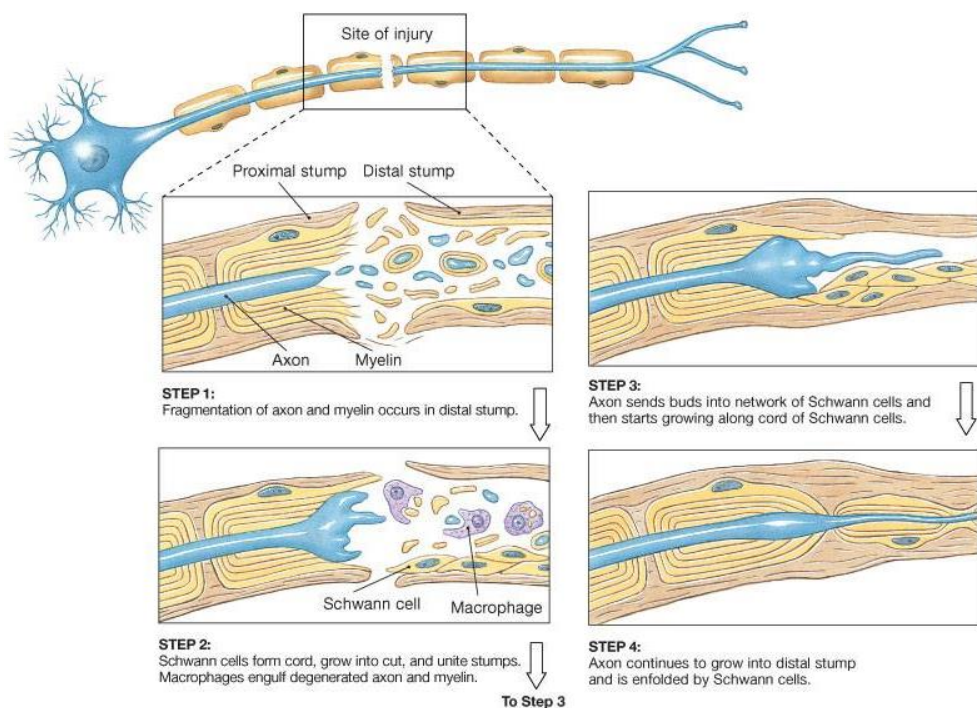
1.1.2 Peripheral nerve injury

Peripheral nerve injury (PNI) represents a major clinical concern worldwide. PNI causes pain and restriction in daily activities of affected individuals and has significant socio-economic impact. With approximately 300,000 cases per year in Europe, unintentional trauma due to for example motor vehicle accidents, sports injuries or lacerations is the most frequent cause of PNI [8]. In addition, damage to peripheral nerves can also be induced by medical procedures (e.g. surgery, radiotherapy,...) or chemical agents (e.g. drug abuse, natural toxins,...). In contrast to the central nervous system, the PNS possesses an intricate ability for repair and regeneration, in which Schwann cells play an important role.

Spontaneous peripheral nerve repair

Following axonal injury, Schwann cells lose their differentiated morphology and re-enter the cell cycle [9]. This process is not only accompanied by downregulation of myelin-associated genes such as Krox20, P0, myelin basic protein (MBP), and myelin associated glycoprotein, but also by an upregulation of immature Schwann cell markers p75NTR, GFAP and neuronal cell adhesion molecule [9-11]. Besides reversal of myelin differentiation, pathways are activated to create a novel phenotype within a few hours after injury, thereby initiating the process of anterograde degeneration or Wallerian degeneration (Figure 1.2). Schwann cells activate several mechanisms to clear the axonal and myelin debris: they enhance their phagocytic activity as indicated by the increased levels of lysosomes and macrophage-2 antigens [12] and produce an enormous amount of cytokines, leading to the infiltration of monocytes into the site of injury [10, 13]. At the same time, they upregulate the expression of several neurotrophic factors like nerve growth factor (NGF), brain-derived neurotrophic factor (BDNF), glial-derived neurotrophic factor (GDNF), basic fibroblast growth factor (bFGF), neurotrophin 3 (NT-3) and vascular endothelial growth factor (VEGF) to promote neuronal survival and axon growth [14]. Furthermore, Schwann cells transform morphologically into cells with long parallel processes, forming the bands of

Büngner within their endoneurial tubes. The aligned Schwann cells and their ECM, consisting primarily of collagen type I, provide indispensable tracks for guided axonal regrowth, thereby allowing for optimal regeneration from the proximal to the distal end of the injury. The molecular programming that transforms mature Schwann cells to these repair Schwann cells (which are different from SCPs and immature Schwann cells) is controlled by the transcription factor *c-Jun*, which promotes downregulation of the myelin program and upregulation of genes involved in nerve repair (e.g. GDNF, BDNF, p75NTR and N-Cadherin) [9, 10, 14]. Finally, to complete the repair process, repair Schwann cells eventually transform again into the native myelinating cells required to envelop the regenerated axons and allow for functional recovery [3]. Successful spontaneous regeneration, however, is amongst others affected by the severity of the nerve lesion.



Copyright © 2003 Pearson Education, Inc., publishing as Benjamin Cummings.

Figure 1.2: Wallerian degeneration and nerve regeneration following PNI. Reprinted from Pearson Education, Inc., publishing as Benjamin Cummings. Copyright © 2003.

PNI classification

Classification of PNI depends on the degree of structural damage, symptoms and prognosis. The two mostly used models are those described by Seddon [15] and Sunderland [16]. While Seddon introduced the terms neurapraxia, axonotmesis and neurotmesis to classify PNI, Sunderland defined two extra categories between axonotmesis and neurotmesis to obtain a five degree classification. Neurapraxia (1st degree) is the mildest form of injury as it represents a temporary impulse conduction block. Often resulting from mechanical compression, it is characterized by demyelination and local ischemia. Since the continuity of the axon is preserved, the prognosis of such lesions is very good and spontaneous recovery occurs within weeks to months. In axonotmesis (2nd degree), there is additional axonal injury that is typically crush or stretch-related but all connective tissue sheets are unharmed. The distal axonal stump undergoes Wallerian degeneration and the proximal axon spontaneously regenerates through the intact endoneurial tubes. Although it might take several months, reinnervation of the target and therefore full recovery of function is very likely. In 3rd degree injury, the Schwann cell basal lamina and the endoneurium are disrupted, which triggers the formation of intrafascicular scar tissue. Obstruction and misdirection of axons complicates the regenerative process but surgery is usually not needed. However, when also the perineurium is interrupted (4th degree), regenerating axons are no longer confined to their fascicle and many become disoriented and obstructed. With only limited functional recovery, surgical intervention is required. Neurotmesis or 5th degree injury is the most severe lesion since the nerve is completely discontinued. Although Wallerian degeneration is initiated, spontaneous recovery is rare and even after surgery functional outcome is substandard. A 6th degree injury has been described for mixed pattern injuries [17]. Since the intrinsic ability of the PNS to regenerate after injury is often a time-consuming and suboptimal process, many attempts have been made to treat PNI.

Treatments

The traditional therapy for PNI is surgical suturing of transected nerves, also referred to as neurorrhaphy or nerve coaptation. Primary end-to-end suturing is universally the treatment of preference. However, when tension-free joining of

the proximal and distal nerve stumps is precluded, autologous nerve grafting is regarded as the gold standard [18, 19]. Given the limited availability of donor tissue, often sensory nerve grafts are transplanted into a purely motor nerve deficits. The resulting morphometric mismatch is one of the main reasons for suboptimal recovery. Furthermore, patients might suffer from complications such as donor site morbidity, scarring and neuroma formation. Other autologous tissue grafts such as vein, muscle and tendon grafts exhibited similar results and limitations [20].

A clinically approved alternative to autografting is the use of hollow nerve guidance conduits. These tissue engineered channels of natural or synthetic nature provide directed mechanical support to the regenerating axons and serve as a barrier for undesirable fibrous tissue. Irrespective of the material used, these hollow conduits are restricted to nerve gaps of 4 cm in humans and fail to meet the efficacy and functional outcome of autologous nerve grafts [21]. This inferior regeneration can be attributed to the absence of endogenous components at the time of transplantation. Repopulating the construct with cells will not only provide extra physical cues but also trophic support for regenerating axons. Therefore, a great hope in the field of PNI treatments relies on the exploitation of cell-based therapies. The most obvious cells to use are Schwann cells as they play a crucial role in the endogenous repair of peripheral nerves. However, the use of primary Schwann cells is unfavorable as they must be harvested from another peripheral nerve and are slowly growing *in vitro* [21, 22]. In search of alternative cell sources, mesenchymal stem cells have shown to be promising candidates for regenerative medicine purposes [23].

1.2 Mesenchymal stem cells

Mesenchymal stem cells (MSCs) are multipotent or adult stem cells, meaning that they are capable of differentiating into cells of one germ layer. Since their discovery by Friedstein *et al.* about 50 years ago in the bone marrow [24], MSCs have gained considerable interest among stem cells researchers. To increase consistency in the isolation and characterization of these stem cells, the Mesenchymal and Tissue Stem Cell Committee of the International Society for Cellular Therapy has proposed in 2006 a set of minimal criteria to define human MSCs for research purposes [25]. First, when isolated and maintained under standard culture conditions, MSCs must be plastic-adherent. Secondly, a panel of different cell surface antigens should be used to identify MSCs in a cell population. These cells should express the surface molecules CD29, CD44, CD73, CD90 and CD105 and lack marker expression of CD11b, CD14, CD34, CD45, CD79a and HLA-DR. Thirdly, given their intrinsic multilineage differentiation potential, MSCs must be capable of differentiation toward osteoblasts, chondrocytes and adipocytes *in vitro*. Depending on the culture conditions, however, MSCs have been shown to be capable of generating various cells of non-mesodermal lineage [26]. For example, several studies described transdifferentiation of bone marrow MSCs toward neuroectodermal cell types, both neurons and glial cells [27-31]. Furthermore, even in an undifferentiated state these stem cells express neural proteins [32], thereby yielding great potential for bone marrow MSCs in the field of neural tissue engineering. Since the collection of bone marrow is invasive and painful, the use of an alternative source of MSCs is strongly encouraged. In the human body, MSCs are present in the stroma of almost every adult organ, including adipose tissue, umbilical cord and teeth [33-35].

1.2.1 Dental pulp stem cells

Dental pulp is an extensively vascularized and innervated connective tissue inside the pulp cavity of a tooth. During tooth development, migrating neural crest cells proliferate and condensate to form the dental papilla, which eventually differentiates into the dental pulp. It is surrounded by a layer of odontoblasts and physically confined in hard materials such as dentin, cementum and enamel. The main cell populations of the dental pulp, namely fibroblasts, odontoblasts and

immune cells, refer to the fundamental functions of the dental pulp: dentin production [36] and immune defense [37]. The observation that new odontoblasts were formed in response to severe tooth damage, suggested the existence of stem cells in the dental pulp [38, 39].

Gronthos *et al.* [40] were the first to isolate and characterize a population of mesenchymal-like stem cells within the dental pulp tissue of impacted third molars, labelled human dental pulp stem cells (hDPSCs). These hDPSCs are highly proliferative and possess self-renewal ability. They can be easily isolated from discarded wisdom teeth, which are considered to be medical waste, with few ethical issues. The two mostly used isolation methods, enzymatic digestion or tissue explants, yield similar hDPSC populations [41]. Their stem cell characteristics are retained upon cryopreservation, leading to the possibility to establish a stem cell bank [42-44]. Since so far no tumorigenic effects have been reported for DPSCs and these stem cells exhibit potent immunomodulatory and anti-inflammatory capacities [45, 46], autologous and allogeneic transplantation in the clinic might be facilitated [47]. Furthermore, under specific culture conditions, DPSCs can be induced to differentiate toward osteogenic, chondrogenic, adipogenic, odontogenic, myogenic, endotheliogenic, melanogenic, hepatogenic and neurogenic lineages [45, 48-55], emphasizing their therapeutic application possibilities to regenerate a wide variety of tissues. Although similar stem cell populations exist in the pulp of human exfoliated deciduous teeth (SHEDs) [56], the apical papilla (SCAPs) [57] and periodontal ligament (PDLSCs) [58], they fall outside the scope of this work and therefore will not be discussed further on.

Neural predisposition of DPSCs

It has been suggested that stem cells that developed from the neural crest have a predisposition to a neural fate [59]. In contrast to mesoderm-derived MSCs, DPSCs share their embryonic origin with cells from the PNS [60], so they could conceivably have more neurogenic potential. This intrinsic capacity to differentiate toward neurons or glial cells is already present in an undifferentiated state, given the constitutive expression of a range of neural proteins by DPSCs. The intermediate filaments nestin and vimentin, which are considered to be markers

of neural precursor cells and MSCs or glial precursor cells respectively, were detected in hDPSCs [48, 52, 61]. Other early neural markers demonstrated in undifferentiated DPSCs include A2B5 (neural stem cells and glial precursors) and doublecortin (neural precursor cells) [62]. Markers associated with mature neural phenotypes (e.g. neurons, Schwann cells, astrocytes or oligodendrocytes) such as β -III-Tubulin, neurofilament, GFAP, S100, p75NTR, NeuN, CNPase, synaptophysin and galactocerebroside are also expressed at basal levels by DPSCs [48, 61, 62]. Furthermore, several *in vitro* studies have reported the production and secretion of several neurotrophic factors including brain-derived neurotrophic factor (BDNF), glial-derived neurotrophic factor (GDNF) and nerve growth factor (NGF) by dental pulp cells, which enhanced the survival and neurite outgrowth of trigeminal [63], embryonic dopaminergic [64] and retinal ganglion [65, 66] neurons via paracrine signalling pathways.

Neural differentiation of DPSCs

Over the past decade, research exploring the neural differentiation potential of DPSCs has focused on neurogenesis. Arthur *et al.* [59] were the first to demonstrate that hDPSCs can differentiate into neuronal derivatives. In response to neuronal inductive stimuli, hDPSCs ceased proliferation and acquired a more mature neuronal phenotype *in vitro*. Although electrophysiological analysis revealed the presence of functional voltage-gated sodium channels [59], voltage-gated potassium channels, which are also essential for action potential generation and propagation, could not be detected. This shortcoming was handled by Kiraly *et al.* who developed a three-step neurodifferentiation protocol consisting of epigenetic programming, induction of neural differentiation and neuronal maturation [52], thereby holding potential for this population to develop into functionally active neuronal cells. When murine DPSCs were maintained in comparable yet moderately adjusted culture conditions, they not only expressed neurotransmitter-specific markers from both CNS and PNS cell types, but also functional voltage gated calcium channels [67]. Connexin-43 was detected in the resulting neuronal-like networks but no functional gap junctions were formed. Furthermore, spontaneous action potentials were not observed which could be attributed to the absence of voltage-gated sodium and potassium channels [67].

In line with these results, Aanismaa *et al.* reported differentiation of hDPSCs into neural precursors but not into mature functional neurons using this three-step protocol [68].

To determine the optimal conditions for neuronal differentiation of hDPSCs, a study comparing two neuronal induction protocols was performed [69]. According to chemical protocol, hDPSCs were exposed for 48 h to β -mercaptoethanol (BME) which has been reported to stimulate the formation of neurite-like processes [28]. In the second protocol, medium supplied with a cocktail of growth factors was added to hDPSCs for a period of 2 weeks. Based on morphology and neurogenic marker expression, Osathanon *et al.* concluded that the growth factor induction protocol should be the preferred method for neuronal differentiation of DPSCs since the chemical protocol induced false-positive neuronal differentiation [69]. Recently, Gervois *et al.* described a new method to induce neurogenic differentiation of hDPSCs [70]. Following neurosphere formation and neuronal maturation based on cAMP and NT-3 signaling, hDPSCs showed morphological features of neuronal cells, altered their secretome and acquired functional voltage-gated sodium and potassium channels. Furthermore, a subset of differentiated hDPSCs was able to fire a single action potential upon current stimulation.

An important note to make here is that in order to facilitate survival, plastic adhesion and expansion, culture media of DPSCs are usually supplemented with 2.5-20 % fetal bovine serum (FBS). The use of FBS is, however, not desirable because of contamination risk, the presence of xenogeneic proteins that can interfere with normal cell behavior or cause immune reactions, high batch-to-batch variation, limited availability and ethical issues [71, 72]. For all these reasons, the utility of FBS-cultured stem cells represents a major obstacle for human therapeutic applications. In attempts to circumvent these issues, serum-free culturing of hDPSCs [73] and its effect on neural differentiation [74, 75] has been evaluated. Although the stem cells were viable in these culture conditions and preserved their differentiation potential, more studies need to be conducted to evaluate the functionality of serum-free cultured DPSCs *in vitro* and *in vivo*.

In spite of significant progress on neuronal differentiation of DPSCs, attaining fully functional neurons has yet to be achieved. Only recently, the *in vitro* differentiation of hDPSCs toward a glial cell type has been described. By means of

transfection with the human Olig2 gene, Askari *et al.* induced hDPSCs to differentiate into oligodendrocyte progenitors [76].

1.3 Role of DPSCs in neural regeneration

As mentioned above, DPSCs seem to hold great potential in regenerating nerve tissue, either by paracrine effects on host cells or by differentiation toward neural cells.

Nosrat *et al.* [63] were pioneers in transplanting dental pulp cells into a hemisectioned spinal cord to study their neuroregenerative capacity. A comment that must be made here is that they used a heterogeneous population of cells as they grafted pieces of rat dental pulp tissue rather than purified DPSCs. Nonetheless, they demonstrated that in this rat model for spinal cord injury, motor neuron survival was promoted in presence of dental pulp cells [63]. In agreement with this study, others showed the neuroprotective effects of rat or human DPSCs in *in vitro* models of Alzheimer's and Parkinson's disease [64, 77, 78]. Via indirect coculture systems and the use of blocking antibodies, this enhanced survival of neurons could be related to the synthesis and release of neurotrophic factors such as NGF, BDNF and GDNF by DPSCs. Since various studies have reported the capacity of DPSCs to secrete a range of neurotrophic factors that promote neuronal survival and axon regeneration, it is believed that these cells hold great potential in the treatment of injuries to both the CNS and PNS. An overview of studies using DPSCs as a treatment for neurological disorders is given in Table 1.1.

1.3.1 DPSCs for CNS repair

Before assessing the therapeutic potential of DPSCs to repair CNS lesions *in vivo*, a study performed by Huang *et al.* evaluated the effect of implantation of undifferentiated DPSCs into the hippocampus of healthy mice. Via growth factor signaling, grafted DPSCs increased proliferation, recruitment and maturation of endogenous neuronal cells [79]. Not only neurotrophic factors but also chemokines produced by DPSCs can have beneficial effects on nerve regeneration. For example, the chemoattractant molecule CXCL12 induced migration of trigeminal axons and assisted in the homing of endogenous neural stem cells following transplantation of hDPSCs into the hindbrain of chicken embryos [80]. The integration of grafted DPSCs was also shown by Kiraly *et al.* Neuronally predifferentiated hDPSCs injected into the cerebrospinal fluid of newborn rats migrated to different brain regions and the lesioned cortex, where they retained

Table 1.1. Therapeutic applications of dented pulp (stem) cells for nerve repair.

Cell type	Transplantation method	Animal model	Model specifications	Recovery period	Main results	Ref.
Rhesus DPSCs	Injection of PBS-cell suspension	Mouse hippocampus	Healthy	30 days	Increased proliferation, recruitment and maturation of host neuronal cells	[79]
hDPSCs	Injection of cell suspension	Embryo chicken hindbrain	Healthy	2 days	Chemoattraction (CXCL12) of trigeminal ganglion axons toward implanted DPSCs	[80]
hDPSC-derived neuronal cells	Injection of medium-cell suspension	Rat cortical lesion	Cold lesion; Injection in cerebrospinal fluid	4 weeks	Grafted DPSCs integrate into host brain and show neuronal properties	[81]
Rat dental pulp tissue	1 mm ³ tissue pieces	Rat SCI	Hemisection	4 weeks	Increased motor neuron survival	[63]
Human dental pulp cells	Injection of medium-cell suspension	Mice SCI	Compression	8 weeks	Improved white matter preservation and tissue organization; Higher levels of tropic-factor expression; Improved locomotor function	[82]
hDPSCs	Injection of PBS-cell suspension	Rat SCI	Complete transection	8 weeks	Inhibition of host cell apoptosis; Promotion of axon regeneration via paracrine mechanisms; Replacement of lost cells by differentiation into mature oligodendrocytes	[62]
Rat DPSCs	Injection of PBS-cell suspension	Rat optic nerve injury	Compression	3 weeks	Increased retinal ganglion cells survival and axon regeneration	[65]

Cell type	Transplantation method	Animal model	Model specifications	Recovery period	Main results	Ref.
hDPSCs	Injection of medium-cell suspension	Rat stroke	Middle cerebral artery occlusion	4 weeks	Improved forelimb sensorimotor function; Targeted migration toward lesion and survival of hDPSCs; Preferential differentiation of hDPSCs into astrocytes	[83]
hDPSC subpopulation	Injection of saline-cell suspension	Rat stroke	Middle cerebral artery occlusion	4 weeks	Improved functional recovery; Differentiation of transplanted hDPSCs into dopaminergic neurons	[84]
hDPSC subpopulation	Injection of PBS-cell suspension	Rat stroke	Middle cerebral artery occlusion	3 weeks	Reduced infarction volume; Improved motor function; Increased neurogenesis and vasculogenesis	[85]
Rat dental pulp cells	Silicone tube with cellular collagen gel	Rat PNI	Facial nerve transection (7 mm)	6 weeks	Improved regeneration; Transplanted cells formed blood vessels and Schwann cells	[86]
Rat dental pulp cells	PGLA tube with cellular collagen gel	Rat PNI	Facial nerve transection (7 mm)	9 weeks	Improved regeneration; Resorbed PGLA tubes	[87]
hDPSC subpopulation	Collagen scaffold	Rat PNI	Sciatic nerve transection (5 mm)	5 weeks	Improved regeneration of myelinated fibers; Enhanced vascularization; Increased proliferation, migration and survival of host Schwann cells	[88]
hDPSC-derived oligodendrocyte precursor cells	Injection of medium-cell suspension	Mouse PNI	Local demyelination of sciatic nerve by lysolecithin	6 weeks	Improved functional recovery; Increased remyelinating axons	[76]

neurospecific marker expression and functional voltage-gated sodium and potassium channels [81].

DPSCs have been postulated to be feasible candidates for therapeutic intervention after SCI. In a study performed by de Almeida *et al.*, hDPSCs were injected in the center of compressed mouse spinal cord [82]. Following an 8 week recovery period, an increased release of trophic factors, better white matter preservation and significantly improved locomotor recovery were observed in these animals. When using the most severe animal model for spinal cord injury, namely complete transection of the spinal cord, locomotor function was substantially better in rats that received transplantation of hDPSCs compared to bone marrow MSCs or skin-derived fibroblast [62]. The therapeutic benefits of hDPSCs were not only attributed to paracrine-mediated activities, since they prevented neuron and glial cell apoptosis at the site of injury and supported axonal regeneration by inhibiting axon growth inhibitors, but also to cell-autonomous effects given their spontaneous differentiation into mature oligodendrocytes to replace lost cells.

Similar results were obtained in a rodent model of focal cerebral ischemia, where improvement in forelimb sensorimotor function was observed after intracerebral transplantation of hDPSCs [83]. Although the transplanted hDPSCs replaced lost tissue, their preferential differentiation toward astrocytes instead of neurons implied an essential role for paracrine effects in improving functional recovery. Other studies have also observed increased locomotor recovery when DPSC subpopulations were transplanted following temporary middle cerebral artery occlusion, although the underlying mechanisms of action are not conclusive. While Yang *et al.* attributed the recovery from neurologic dysfunction to differentiation of transplanted DPSCs into dopaminergic neurons [84], Sugiyama *et al.* found the release of trophic factors rather than direct cell replacement to have beneficial effects on neurogenesis and vasculogenesis [85].

A recent study performed by Mead *et al.* showed the potential of rat DPSCs for treatment of optic nerve crush injury, since they promoted survival and axon regeneration of retinal ganglion cells via the secretion of multiple neurotrophins [65]. Taken together, these studies point out the potential of DPSCs in cell-based therapies for injuries to the CNS [89].

1.3.2 DPSCs for PNS repair

In addition to studies investigating the regenerative capacity of DPSCs in CNS disorders, researchers have also proposed DPSCs as a therapy for PNI. In two different studies, Sasaki and coworkers transplanted a collagen gel containing dental pulp cells in a 7 mm rat facial nerve gap [86, 87]. Irrespective of the material used for the nerve guidance conduit, either silicone tubes [86] or biodegradable poly-DL-lactide-co-glycolide (PGLA) tubes [87], nerve repair was significantly faster in animals that received nerve guidance conduits with DPSCs compared to acellular conduits. The use of PGLA tubes was preferred since this material was resorbed over time, thereby making a secondary removal operation redundant [87]. Very recently, enhanced revascularization and regeneration of myelinated fibers was observed in a 5 mm rat sciatic nerve defect grafted with a subpopulation of hDPSCs. The expression of several neurotrophic factors such as BDNF, GDNF, NFG and VEGF in the vicinity of the transplanted cells exerted trophic effects on resident Schwann cell proliferation, migration and survival [88]. In another study, transplantation of DPSC-derived oligodendrocyte precursor cells into damaged mice sciatic nerves led to better recovery of behavioral reflexes compared to transplantation of undifferentiated DPSCs [76]. So in order to achieve therapeutic applications of DPSCs in neural tissue engineering, transplantation of neural differentiated cells that secrete a range of neurotrophic factors seem to hold great potential.

1.4 Scaffolds for neural tissue engineering

The use of materials for physical guidance of regenerating axons dates back to over a hundred years ago [90-92]. By providing a three-dimensional (3D) scaffold for infiltrating or incorporated cells, biomaterials can set the stage for *de novo* tissue generation. In attempts to meet with the performance of nerve autografts, a wide range of natural and synthetic biomaterials have been subject of past and current neuroregenerative research. The design of artificial nerve conduits is very challenging since they must comply with a set of conditions to serve as appropriate scaffolds including, but not limited to, biocompatibility, biodegradability, porosity, permeability and mechanical properties [93]. Furthermore, a number of repair strategies are available to improve the existing hollow nerve guidance conduits, such as surface functionalization, micro-grooved lumina and intraluminal guidance channels [21, 93-95]. Fabrication of such conduits can be achieved by electrospinning, porogen leaching and freeze-drying amongst others [95].

1.4.1 Hydrogels

In search of a scaffold with optimal characteristics, hydrogels have gained significant interest in the field of neural tissue engineering. Their high water content and polymeric 3D networks allow the diffusion of oxygen, nutrients and waste products, making them highly suitable for the encapsulation of cells [96, 97]. For cells to be able to interact with their ECM (see section 1.4.2), the presence of biochemical cues is essential. This can be realized either by using natural ECM molecules such as collagen, laminin or fibronectin, or by chemically modifying the surface of synthetic polymers. Another interesting property of hydrogels is that their stiffness bears resemblance to that of soft nerve tissue, ranging from 0.1-500 kPa [98, 99]. Fine-tuning the mechanical properties of hydrogels has been shown to enable maximal neurite extension on and within these scaffolds [100, 101]. In addition to exploring the biochemical and mechanical versatility of hydrogels to achieve optimal tissue regeneration, many efforts have been made to control fibrillar organization. It is well known that topographical features can influence cellular morphology, behavior, differentiation and migration [102]. The intrinsic isotropic structure of hydrogels, however, does not comply with highly oriented structures often found in the body such as tendons and nerves. As these

tissues are mainly composed of collagen, the field of tissue engineering has focused on developing approaches to create aligned collagen hydrogels.

Collagen

Comprising about 25% of the total dry weight of mammals, collagen is the most abundant protein in mammals, with about 29 types being described up to now [103]. They are all built from three α -chains that contain a glycine at every third amino acid position to allow the formation of tropocollagen. This is a tightly packed right-handed triple helix structure with a length of 300 nm and a diameter of 1.5 nm held together by hydrogen bonds (Figure 1.3) [104]. Many of these tropocollagen molecules can self-assemble longitudinally and bilaterally into fibrils via covalent bonds (e.g. collagen type I, II, III and V). Although the length of such fibrils can be several micrometers and their diameter can range from 10 to 500 nm, they all have a characteristic band pattern that is repeated every 67 nm (Figure 1.3). Side-by-side packing of fibrils creates collagen fibers, which have an enormous tensile strength. Given its abundance, self-aggregation capacity, biodegradability and bioactive cell adhesion sites, collagen and especially collagen type I has been commonly used as biomaterial in tissue engineering applications [104, 105].

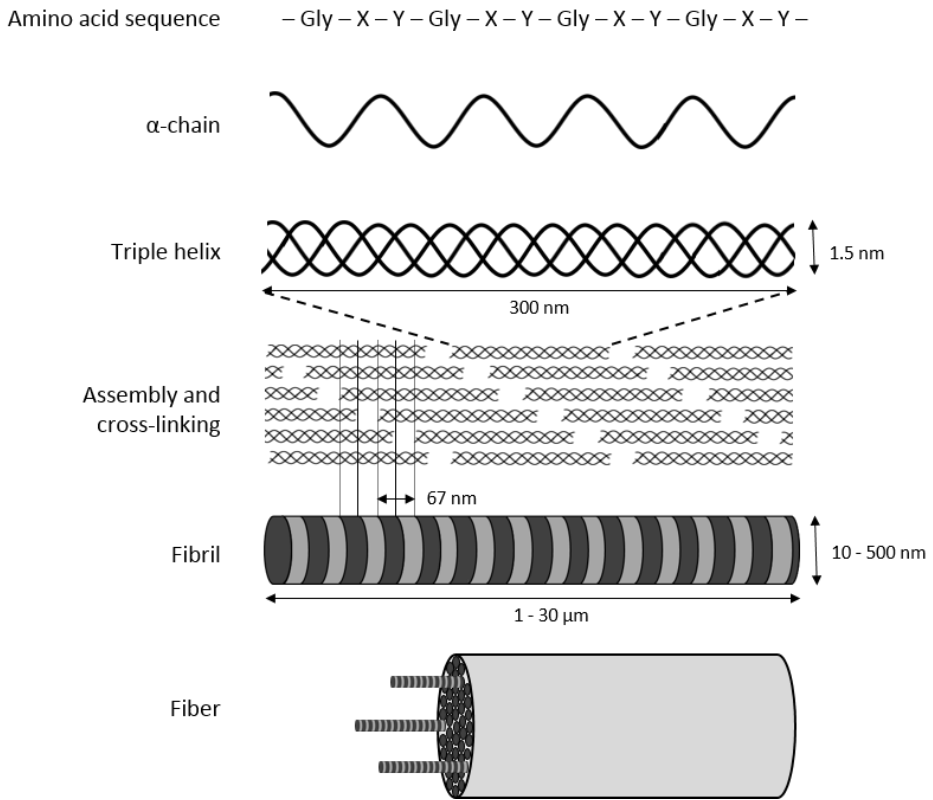


Figure 1.3: Structure of fibrillar collagen. Three α -chains, each consisting of a unique amino acid sequence, assemble into a triple helix. Cross-linking of triple helices leads to fibril formation, which can bundle to form fibers.

Aligned collagen type I hydrogels

Elsdale and Bard were the first to obtain aligned collagen fibrils in a hydrated lattice by applying gravity-driven flow to gelling hydrogels [106]. A modernization of this technique encompassed pressure-driven flow of a collagen solution through channels with a diameter of approximately 100 μm [107]. Exposing hydrogels to strong magnetic fields or electrical gradients has also shown to be effective in preparing highly anisotropic fibrillar hydrogels [108-110]. However, the technical equipment required for the production of such aligned hydrogels is rather complex and the appearance of these matrices is unnatural homogeneous as the whole

hydrogel is equally subjected to external conditions. Since the ECM is dynamically remodeled by a variety of cell types during development and normal tissue homeostasis, a more natural approach for manufacturing anisotropic substrates would involve cell-mediated alignment of 3D scaffolds. Via integrin-mediated interactions, cells can attach to their ECM and exert contractile forces, thereby applying an internal strain to their surrounding network. When cell-seeded hydrogels are tethered at opposite ends, the encapsulated cells will contract and generate a uniaxial tension in the system, which causes both cells and fibrils to become aligned over time [111, 112]. By taking advantage of cell-matrix interactions and cytoskeletal contraction, a suitable environment for nerve regeneration can be created.

1.4.2 Cell-matrix interactions

The interaction between cells and their ECM is mediated via integrins. Integrins are a large family of heterodimeric transmembrane receptors comprised of two non-covalently bound subunits, namely α and β . In mammals, 18 α and 8 β subunits have been identified that can combine to form 24 distinct conformations [113]. Each heterodimer has a large extracellular domain that contains a binding site for cell-surface, ECM or soluble protein ligands. The short cytoplasmic tail connects to the cytoskeleton via a number of anchor proteins. This linkage allows for bidirectional signaling across the plasma membrane. Signals received from other receptors can induce changes in the affinity and conformation of integrin heterodimers, a process referred to as inside-out signaling. Upon ligand binding, the receptors move laterally in the plane of the membrane and cluster to form focal adhesions, which can initiate intracellular signaling pathways to control cellular behavior such as survival, migration and differentiation [113, 114].

Ligand specificity is determined by the extracellular domains of both subunits of the heterodimer. Most integrins recognize relatively short amino acid sequences from ECM molecules. Depending on their ligand preference, integrins can be classified as primary collagen receptors (integrins $\alpha 1\beta 1$, $\alpha 2\beta 1$, $\alpha 10\beta 1$ and $\alpha 11\beta 1$), laminin receptors (integrins $\alpha 3\beta 1$, $\alpha 6\beta 1$, $\alpha 6\beta 4$ and $\alpha 7\beta 1$) and fibronectin receptors (integrins $\alpha 5\beta 1$, $\alpha 8\beta 1$, $\alpha I\text{Ib}\beta 3$ and the $\alpha v\beta(3, 5, 6 \text{ and } 8)$ integrins). The existence of leukocyte-specific integrin receptors, namely integrin $\alpha L\beta 2$, $\alpha M\beta 2$, $\alpha X\beta 2$, $\alpha D\beta 2$ and $\alpha E\beta 7$, has also been described. However, this integrin classification is not

absolute as redundancy exists with respect to certain integrin-ECM interactions: although the affinity might be different, some integrins recognize the same ligand and conversely, some ligands can bind to different integrins [113, 115].

1.5 Label-free optical imaging

Optical microscopy has been a revolutionary tool for numerous biomedical applications. Over the past decades much effort has been made in increasing the image quality. Prevalent throughout the life sciences is the technique of fluorescence using widefield or laser scanning confocal microscopy. Despite their power in visualizing molecules in biological specimens with high contrast and specificity, fluorescence microscopy relies mostly on the use of exogenous fluorophores. These labels can have significant disadvantages such as (i) phototoxicity, which can hamper long-term observations, (ii) altered properties of the target molecule, thereby possibly perturbing normal cell behavior including proliferation and differentiation and often (iii) fixation of the samples, which prevents continuous monitoring [116, 117]. In search of alternative non-invasive imaging modalities, label-free optical microscopy techniques have been explored to their potential. For example, in confocal reflectance microscopy, reflected or back-scattered light from structures such as collagen fibrils is collected. However, constraints of this technique include limited penetration depth and low contrast [118]. Another example is single photon excitation of autofluorescent molecules, which is not preferable since ultraviolet light is known to be harmful for biological samples. More elaborate approaches of label-free optical microscopy stand on the principle of nonlinear optics, which is based on the simultaneous interaction of two or more photons with a molecule. As this requires high peak power at sufficiently low average energy, picosecond or femtosecond pulsed lasers are used, thereby also offering intrinsic axial sectioning, increased penetration depth and reduced photodamage [119, 120]. The two most common endogenous nonlinear optical phenomena, namely two-photon excitation autofluorescence and second harmonic generation, are described in the following paragraphs.

1.5.1 Two-photon excitation autofluorescence

In two-photon excitation fluorescence, fluorescent molecules are brought to an excited state after the absorption of two near-infrared photons. Following internal conversion and vibrational relaxation, the excited molecules fall back to their ground state through the emission of one photon with higher energy, and therefore at shorter wavelength, as compared to the excitation photons [119]

(Figure 1.4a, left). Although a variety of fluorescent dyes or labels are available, a diverse range of intrinsically fluorescent molecules are contained in biological specimens, both intracellular (e.g. nicotinamide adenine dinucleotide, flavins and serotonin) and extracellular (e.g. collagen, elastin and keratin) [121]. Autofluorescence obtained by two-photon excitation fluorescence is further referred to as TPEA. Researchers have extensively exploited these native fluorophores to characterize cells and tissues in physiological or diseased conditions. For example, since alterations in the metabolic state of cells can lead to subtle changes in their autofluorescent fingerprint, cellular differentiation [122-124] and cancer development [125-127] could be identified.

1.5.2 Second harmonic generation

In contrast to TPEA, SHG does not involve the absorption of incident photons, but relies on induced polarization. In this second order coherent process, a wavelength-conversion effect generates frequency-doubled light from the excitation photons (Figure 1.4a, right). Only materials with a high degree of non-centrosymmetric organization such as collagen type I (Figure 1.4b), myosin and tubulin can exhibit SHG [119]. Given the high signal-to-noise ratio, the possibility to spectrally separate these signals from TPEA sources and the overall advantages of nonlinear optics, SHG microscopy has emerged as a powerful modality in a variety of biomedical imaging applications. Researchers have not only elucidated the organization of healthy sarcomeres and collagen fibrils by means of SHG imaging [128, 129], but have also explored its diagnostic potential for a range of diseases such as cancer, fibrosis and atherosclerosis [130].

In order to obtain accurate quantitative microstructural information from such label-free obtained images, robust automated analysis methods are essential. Image correlation spectroscopy (ICS) has been used to characterize collagen based hydrogels through images based on scatter, fluorescence and SHG [131-133]. In this method a spatial autocorrelation function (ACF) of the pixel content is calculated. This ACF contains information on various properties of the hydrogels, such as pore size, collagen density, fibril length, thickness and orientation of collagen hydrogel images [132-135]. Recently, Paesen *et al.* proposed an alternative ICS model for random fibril orientation which included SHG-specific polarization effects to obtain a more accurate ACF amplitude recovery as shown

by simulations and experimental data on a collagen type I hydrogel dilution series [136]. Therefore, this approach holds great potential to study the microstructural organization of SHG imaged cellular collagen type I hydrogels that are developed for regenerative medicine purposes.

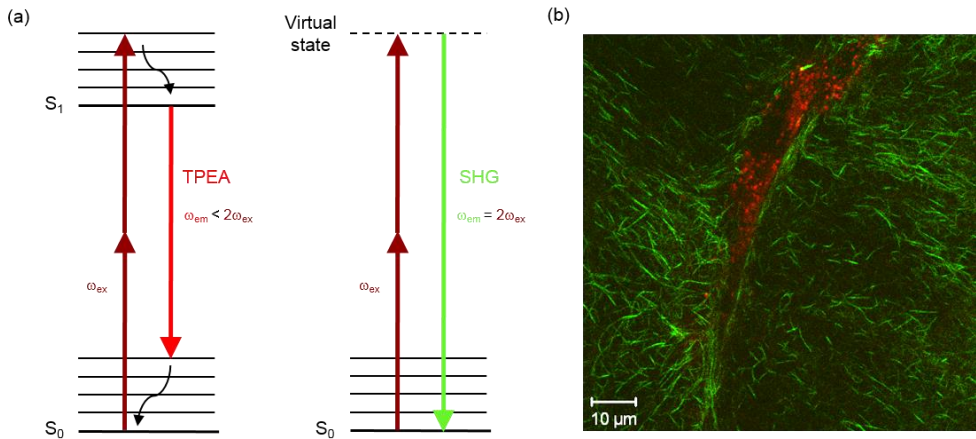


Figure 1.4: Two-photon excitation autofluorescence (TPEA) and second harmonic generation (SHG). (a) Energy level diagrams of TPEA (left) and SHG (right), with indications of ground state (S_0), excited state (S_1) and virtual state (dashed line). (b) Label-free image of a living human MRC-5 fibroblast (TPEA, red) at 37°C in a collagen type I hydrogel (SHG, green).

1.6 Aims of the study

In order to facilitate and enhance peripheral nerve regeneration, an ideal nerve conduit should meet the following criteria: (i) the presence of growth factors, either released by the scaffold or by incorporated cells, to promote neuronal survival and neurite growth, (ii) a 3D aligned cellular scaffold to direct regenerating axons to the distal nerve stump and (iii) the possibility for host or delivered Schwann cells to myelinate the regenerated nerves. As an alternative source of autologous Schwann cells, which are difficult to isolate and grow, human dental pulp stem cells (hDPSCs) represent an attractive population of stem cells for neural tissue engineering due to their neural crest origin. Indeed, hDPSCs have been shown to exhibit a broad range of neuroprotective and neuroregenerative properties *in vitro* and *in vivo* due to the secretion of neurotrophic factors and cytokines. Furthermore, extensive research has been conducted on the ability of these cells to differentiate into neuronal cell types. This is in contrast with glial differentiation of hDPSCs, which remains poorly studied. Therefore, **the first aim of this study is to explore the morphological and functional differentiation of hDPSCs toward Schwann cells *in vitro* (chapter 2)**. In this regard, hDPSCs are exposed to a sequence of growth factors to induce glial differentiation. The resulting Schwann-like cells (d-hDPSCs) are screened for glial markers, ultrastructural properties, neuroregenerative potential and myelination capacity via a range of *in vitro* assays. However, additional research is required in order to potentiate therapeutic application of these cells for peripheral nerve injury (PNI). **In chapter 3, the potential of d-hDPSCs as a cell-based therapy for peripheral nerve repair is evaluated.** Since the survival of transplanted cells in bioengineered scaffolds depends, amongst others, on adequate (neo-) vascularization of the construct, the paracrine angiogenic properties of d-hDPSCs are investigated by means of different *in vitro* tests. Next, 3D collagen type I hydrogels containing self-aligned d-hDPSCs are transplanted in an *in vivo* model of large gap PNI and the regenerated nerve tissue is evaluated for the presence of neurites, myelinated axons and blood vessels.

Within the field of tissue engineering, the similarity of the 3D construct and the native ECM often determine the success of tissue repair. So, in order to develop

biologically active scaffolds for regenerative medicine purposes, their microstructural organization must be thoroughly studied during the design process and before transplantation, preferentially by using non-invasive imaging and robust automated analysis methods. Recently, our group has introduced an alternative ICS model to accurately quantify characteristics of isotropic fibril networks in polarization second harmonic generation (SHG) images. It was suggested that this model could be extended to map the mean fibril direction and its angular spread in preferentially oriented fibrous hydrogels. Therefore, **the third aim of this study is to apply SHG microscopy and expand our ICS model to map local changes in self-aligning cellular collagen type I hydrogels (chapter 4)**. First, a collagen hydrogel contraction assay with hDPSCs and d-hDPSCs is performed to capture cell-induced hydrogel modifications at the microscopic scale and link these to changes in overall gel dimensions over time. Next, to support its potential for tissue engineering research, the spatial and temporal changes in hydrogel density and collagen fibril orientation of the 3D cellular self-aligned collagen type I hydrogels described previously are mapped and quantified using SHG microscopy and ICS analysis.

The collagen contraction assay performed in chapter 3 showed distinct contraction profiles between hDPSCs and d-hDPSCs when seeded in a collagen type I hydrogel, with d-hDPSCs being more potent. Since the collagen concentration and cell seeding density were identical, the difference in contractile capacity is most likely attributed to variation in the mechanobiology of the two cell types. The interaction between cells and their ECM is mediated by a class of transmembrane receptors called integrins. However, the profile of integrins, both type and amount, can vary from one cell type to another. **Therefore, in chapter 5, the mechanisms by which these cells contract and interact with a collagen type I hydrogel are elucidated.** The expression profiles of different collagen-binding integrin subunits are investigated via mRNA and protein analysis. Furthermore, antibody-based inhibition of specific integrin subunits is performed to reveal their contribution in collagen hydrogel contraction. With this work, we aim at better understanding the mechanisms that control the behavior of cells in their 3D environment, which is of great value for successfully creating cellular self-aligned scaffolds as a therapy for PNI.

Chapter 2

In vitro differentiation of human dental pulp stem cells into Schwann cells

Based on:

Human dental pulp stem cells can differentiate into Schwann cells and promote and guide neurite outgrowth in an aligned tissue-engineered collagen construct *in vitro*.

Martens W*; [Sanen K*](#); Georgiou M; Struys T, Bronckaers A, Ameloot M; Phillips J, Lambrechts I.

The FASEB Journal. 2014 Apr;28(4):1634-43. IF(2013)=5.480

(*) Authors contributed equally.

Declaration of own contribution: Differentiation of hDPSCs toward d-hDPSCs, conduction and analysis of immunocytochemical stainings, ELISA's, EngNT preparation and cocultures experiments. Participation in writing of the manuscript.

2.1 Abstract

In the present study, we evaluated the differentiation potential of human dental pulp stem cells (hDPSCs) toward Schwann cells, together with their functional capacity with regard to myelination and support of neurite outgrowth *in vitro*. Successful Schwann cell differentiation was confirmed at the morphological and ultrastructural level by transmission electron microscopy. Furthermore, compared to undifferentiated hDPSCs, immunocytochemistry and ELISA tests revealed increased glial marker expression and neurotrophic factor secretion of differentiated hDPSCs (d-hDPSCs), which promoted survival and neurite outgrowth in 2-dimensional dorsal root ganglia cultures. In addition, neurites were myelinated by d-hDPSCs in a 3-dimensional collagen type I hydrogel neural tissue construct. This engineered construct contained aligned columns of d-hDPSCs that supported and guided neurite outgrowth. Taken together, these findings provide the first evidence that hDPSCs are able to undergo Schwann cell differentiation and support neural outgrowth *in vitro*, proposing them to be good candidates for cell-based therapies as treatment for peripheral nerve injury.

2.2 Introduction

A variety of traumas and diseases can cause peripheral nerve injury (PNI), which often results in chronic pain and disability [137]. Endogenous repair is known to initiate after injury and is strongly dependent on the contribution of Schwann cells, as the regenerative capacity of peripheral nerves is reduced in their absence [138]. Schwann cells not only reconstitute myelin, which is essential for fast neural action potential propagation, but also provide physical guidance (bands of Büngner) and trophic support for axonal regeneration. Regeneration following nerve transection is limited by the distance between the nerve stumps, and bridging strategies are required where direct end-to-end repair is not feasible. Bridging strategies include the use of tubes and decellularized nerve tissue, and, for longer gaps (>3 mm), the nerve autograft is currently regarded as the gold standard [137]. While autografts provide Schwann cells and appropriate architecture for regeneration, there are problems with availability and donor site morbidity, and overall clinical outcomes show limited success [137, 139].

A wide range of biomaterial and tissue engineering approaches have been used to generate potential alternatives that recreate beneficial aligned cellular features of the autograft [94, 140, 141]. In particular, hydrogels made from natural proteins have gained significant interest due to their functional extracellular matrix properties, inherent biocompatibility, and suitability as carriers for different cell types [96, 97]; however, there are limitations associated with the generation and maintenance of guidance architecture in hydrogels [142]. A technique was recently developed to align and stabilize Schwann cells and collagen fibrils in a collagen type I hydrogel, thereby generating an aligned tissue-like cellular biomaterial for neural tissue engineering [143]. For this approach to be clinically useful, a suitable source of Schwann cells is required for the engineered neural tissue (EngNT) construct. The use of autologous Schwann cells for PNI is restricted because their isolation requires resection of another peripheral nerve, and they are known to expand slowly when cultured *in vitro*, thereby leading to the need for alternative cell sources [144, 145].

Adult stem cells, such as mesenchymal stem cells (MSCs), are promising candidates to treat PNI. MSCs can be isolated from a wide range of tissues and have been shown to secrete neurotrophic factors (NFs) capable of inducing axonal

outgrowth, and they can differentiate into Schwann-like cells or neurons [146, 147]. A promising alternative cell source is human dental pulp stem cells (hDPSCs) [40]. These are ectoderm-derived stem cells, originating from migrating neural crest cells and possessing MSC properties [148-151]. The resulting stem cell population can be easily isolated from discarded wisdom teeth without the need for invasive tissue harvest associated with other sources of MSCs. Furthermore, their stem cell properties are retained after cryopreservation, providing the opportunity to establish a stem cell bank [40, 152]. In addition to their ability to differentiate into cells of mesodermal lineages, hDPSCs have the potential to differentiate along the neural lineage. Even in an undifferentiated state, hDPSCs already express neural markers like S100, β -III-tubulin, and p75NTR and are able to produce and secrete a range of NFs, ciliary neurotrophic factor, vascular endothelial growth factor (VEGF), brain-derived neurotrophic factor (BDNF), glia-derived neurotrophic factor (GDNF), and nerve growth factor beta (b-NGF), thereby enhancing and guiding axonal outgrowth [63, 64, 79, 80, 153]. Although several groups have already reported *in vitro* neuronal differentiation of hDPSCs [48, 52, 59], the differentiation of hDPSCs toward Schwann cells has not been reported to date.

Here we established a protocol for glial differentiation of hDPSCs *in vitro* and assessed the functional capacity of differentiated hDPSCs (d-hDPSCs) with regard to myelination and support of neurite growth. Our findings provide the first evidence that hDPSCs are able to undergo differentiation toward Schwann-like cells that support neural outgrowth *in vitro*, revealing them to be good candidates for cell-based therapies to treat PNI.

2.3 Materials and methods

2.3.1 Materials and products

All products were purchased from Sigma-Aldrich (Bornem, Belgium) unless stated otherwise.

2.3.2 Isolation and differentiation of hDPSCs into Schwann-like cells

Human third molars were collected with written informed consent from donors (15–20 years of age) undergoing tooth extraction for orthodontic or therapeutic reasons at Ziekenhuis Oost-Limburg (Genk, Belgium). When donors were underaged, written informed consent was obtained *via* their legal guardians. This study was approved by the medical ethical committee of Hasselt University. hDPSCs were isolated from dental pulp tissue *via* the explant method previously described [154]. hDPSCs were maintained in minimal essential medium, a modification (αMEM) supplemented with 10% fetal bovine serum (FBS, Biochrom AG, Berlin, Germany), 2 mM L-glutamine, 100 U/ml penicillin, and 100 µg/ml streptomycin. When 80–90% confluency was reached, cells were routinely subcultured.

At passage 2–3, Schwann cell differentiation was induced by changing the medium to standard culture medium without FBS containing 1 mM β-mercaptoethanol (BME) for 24 h. Subsequently cells were incubated in standard culture medium supplemented with 35 ng/ml all *trans*-retinoic acid (RA). After 72 h, medium was changed to standard culture medium supplemented with 5 µM forskolin, 10 ng/ml basic fibroblast growth factor (b-FGF), 5 ng/ml platelet-derived growth factor AA (PDGF_{aa}), and 200 ng/ml heregulin-β-1 (NRG) (Immunotools, Friesoythe, Germany). The cells were cultured in this supplemented medium for 2 weeks with medium changes every 2–3 d [155]. hDPSCs differentiated toward Schwann-like cells are henceforth referred to as d-hDPSCs. Both hDPSCs and d-hDPSCs were grown at 37°C in a humidified atmosphere with 5% CO₂.

2.3.3 Collection of conditioned medium

hDPSCs were seeded at a density of 20,000 cells/cm² in standard hDPSC culture medium. After 24 h, hDPSCs were rinsed with PBS and incubated with standard culture medium supplemented with 0.1% FBS instead of 10% FBS. After 48 h of

incubation, the medium was collected and stored at -80°C . Furthermore, conditioned medium from d- hDPSCs was collected as described above and stored at -80°C .

2.3.4 Isolation of primary Schwann cells

Primary Schwann cells were isolated from postnatal d 17 Sprague-Dawley rats as described previously [156] with minor modifications. Briefly, sciatic nerves were dissected out and stripped free of epineurium. Following enzymatic treatment with 0.25% collagenase and 0.25% trypsin-EDTA, the nerve segments were mechanically dissociated. Cells from 2 nerve segments (1 animal) were seeded in a T25 flask precoated with $10\ \mu\text{g/ml}$ poly-L-lysine. Further purification of the culture was performed as previously described (31).

2.3.5 Immunocytochemistry

An immunocytochemical analysis was performed on hDPSCs, d-hDPSCs and primary Schwann cells with antibodies against glial fibrillary acidic protein (GFAP; 1:400; Leica Microsystems/ NovoCastra, Diegem, Belgium), p75NTR (1:50, Dakocytomation, Glostrup, Denmark), laminin (1:1000, Abcam, Cambridge, UK), CD104 (1:100, Abcam), and nestin (1:500, Millipore, MA, USA) to determine the immunophenotype after differentiation. Cells were fixed with 4% paraformaldehyde (PFA) at 4°C for 20 min and washed with PBS. In case of intracellular targets, cells were permeabilized with Triton-X 0.05% for 30 min at 4°C . To block non-specific binding sites, cells were incubated with 10% normal donkey serum at room temperature for 20 min. After washing with PBS, cells were incubated with primary antibody for 1 h, followed by incubation with donkey anti-rabbit Alexa488 (1:500) or donkey anti-mouse Alexa555 (1:500) secondary antibodies for 30 min at room temperature. Slides were mounted using 4',6-diamidino-2-phenylindole (DAPI) with Prolong Gold Antifade (Molecular Probes, Merelbeke, Belgium). Fluorescence was visualized with a Nikon Eclipse 80i fluorescence microscope equipped with a Nikon DS-2MBWc digital camera (Nikon, Tokyo, Japan). Samples in which primary antibodies were omitted were used as a negative control.

2.3.6 Ultrastructural analysis: transmission electron microscopy (TEM)

Following fixation with 2% glutaraldehyde (Laborimpex, Brussels, Belgium) in 0.05M cacodylate buffer (pH 7.3; Aurion, Wageningen, the Netherlands) at 4°C, the fixative was gently aspirated with a glass pipette, and the cells were postfixed in 2% osmium tetroxide (Aurion) for 1 h. Subsequently, the cell-seeded coverslips were put through a dehydrating series of graded concentrations of acetone and embedded in araldite according to the popoff method [157]. Ultrathin sections (0.06 µm) were mounted on 0.7% formvarcoated copper grids (Aurion), contrasted with 0.5% uranyl acetate and a stabilized solution of lead citrate (both from Laurylab, Saint-Fons Cedex, France), and examined in a Philips EM 208 transmission electron microscope (Philips, Eindhoven, The Eindhoven) operated at 80 kV. The microscope was provided with a Morada Soft Imaging System (SIS; Olympus, Tokyo, Japan) camera to acquire high-resolution images of the evaluated samples. The images were processed digitally with iTEM-FEI software (Olympus SIS).

2.3.7 Enzyme-linked immunosorbent assay (ELISA)

ELISAs were performed on conditioned medium derived from hDPSCs and d-hDPSCs in order to determine the concentration of BDNF, GDNF, neurotrophin 3 (NT-3) and b-NGF (RayBiotech, Boechout, Belgium). Experiments were performed in triplicate and absorbance was measured at 450 nm by means of the FLUOstar Optima multifunctional microplate reader (BMG Labtech, Ortenberg, Germany). Conditioned medium from 9 different donors was used, and ELISA tests were performed according to the manufacturer's protocol.

2.3.8 Neonatal dorsal root ganglion (DRG) neuron cell cultures: 2-dimensional (2D) experiments

Experimental procedures involving neonatal animals were approved by the Hasselt University animal ethics advisory group. DRGs were harvested from 5-d-old Sprague-Dawley rat pups. Briefly, isolated DRG explants were dissociated with 0.025% collagenase at 37°C for 1 h. Dissociated cells were seeded onto coverslips at a density of 25,000 cells/cm². Coverslips were precoated with poly-L-lysine (10 µg/ml) for 1 h. At 1–2 h after cell plating, medium was changed to remove non-adhering cells. Neurons were cultured for 24 h in DMEM/F12 medium

supplemented with Glutamax, 10% FBS, 100 U/ml penicillin, and 100 µg/ml streptomycin.

2.3.9 Survival assay

Isolated neonatal DRG cultures were seeded in a 96-well plate at a density of 10,000 cells/well. The next day, cells were washed twice with PBS, and the medium was replaced with conditioned medium from hDPSCs or d-hDPSCs. αMEM with 10 or 0.1% FBS (henceforth DRG 0.1%) was used as positive or negative control, respectively. After 48 h, the medium was removed, and 500 µg/ml MTT was added to the wells. The MTT solution was removed after an incubation time of 4 h at 37°C. A mixture of 0.01 M glycine and DMSO was added to each well. The absorbance was measured at a wavelength of 540 nm with a Benchmark microplate reader (Bio-Rad Laboratories, Nazareth Eke, Belgium). Conditioned medium from cultures from ≥7 different donors was used.

2.3.10 Neurite regeneration assay

Neonatal DRG cultures were incubated with conditioned medium from hDPSCs or d-hDPSCs to analyze the effect on neurite outgrowth. αMEM with 10% FBS or DRG 0.1% was used as positive or negative control, respectively. After 48 h, cells were fixed in 4% PFA and immunostained using anti-β-III-tubulin. Four independent experiments were carried out, and neurite outgrowth was assessed by measuring the length of the longest neurite of individual cells.

2.3.11 Adult DRG cell cultures: 3-dimensional (3D) experiments

Experimental procedures involving adult animals were conducted in accordance with the UK Animals (Scientific Procedures) Act (1986) and approved by the Open University animal ethics advisory group. Dissociated DRG cultures were prepared from adult (200–300 g) Sprague-Dawley rats that were culled using CO₂ asphyxiation. Briefly, spines were removed, and DRG explants were collected in DMEM with 10% FBS and 100 U/ml penicillin and 100 µg/ml streptomycin. After removal of the connective tissue and nerve roots, DRGs were placed into a collagenase solution (0.125%) at 37°C. After 90 min of incubation, collagenase was removed, and explants were triturated in DMEM with 10% FBS until a homogenous cell suspension was obtained. Next, cells were transferred to culture

flasks containing DMEM with 10% FBS, 100 U/ml penicillin, 100 µg/ml streptomycin, and 10 µM cytosine arabinoside (Ara-C) for 24 h to deplete the non-neuronal cells.

2.3.12 Myelination in hydrogel

d-hDPSC-seeded collagen gels were tethered within rectangular stainless steel molds according to methods described previously [158-160]. Gels were prepared using 10% cell suspension (a mixture of 250,000 d-hDPSCs and 5 dissociated DRG explants per milliliter of gel) mixed with 10% MEM and 80% type I rat tail collagen (5 mg/ml in 0.6% acetic acid; First Link, Wolverhampton, UK) following neutralization using sodium hydroxide. This mixture (1 ml) was added to each mold at 4°C and integrated with tethering mesh at opposite ends before setting at 37°C for 10 min. Tethered gels were immersed in medium, and after 2 weeks, the contracted hydrogels were fixed overnight with 4% PFA at 4°C. The higher collagen concentration (compared to tethered gels used in EngNT assembly) delayed the process of hydrogel contraction and cell alignment, thereby allowing long-term incubation of the uncompressed cellular hydrogel in the mold.

2.3.13 TEM of cellular hydrogels

Cellular hydrogels were fixed with 4% PFA and processed for TEM as described above, with the ultrathin sections sliced perpendicular to the longitudinal axis of the hydrogel in this case. The total numbers of d-hDPSCs and neurites were manually counted in each ultrathin section (3 sections/gel, $n=5$ gels). A distance of <40 nm between a neurite and a d-hDPSC was considered to be a contact between cell types. Data were normalized to number per square millimeter of hydrogel section.

2.3.14 Generation of EngNT using d-hDPSCs

A cell-seeded collagen gel was prepared as described above, with some modifications. d-hDPSCs were suspended in a collagen type I solution of 2 mg/ml (First Link) to give a final density of 10^6 cells/ml gel mixture. Tethered gels were immersed in medium for 4–6 h to allow alignment to develop. Aligned cellular gels were stabilized by plastic compression, i.e. removal of interstitial fluid from hyperhydrated scaffolds by unconfined compression to increase the matrix and

cell density and improve their suitability for use in regenerative medicine. To this end, aligned tethered gels were separated from the tethering mesh using a scalpel, then immediately compressed by loading the gel with 120 g for 1 min, while fluid was removed into a porous paper pad underneath. The resulting sheets of EngNT were transferred to 24-well plates for *in vitro* neurite growth experiments.

2.3.15 Seeding of dissociated DRG neurons on top of EngNT

Adult DRG neurons (20 dissociated DRG explants) were seeded onto the surface of each EngNT sheet and allowed to settle for 30 min, and then constructs were immersed in medium at 37°C in a humidified incubator with 5% CO₂. After 3 d, the EngNT-neuron cocultures were washed briefly in PBS and fixed in 4% PFA at 4°C for 24 h, followed by immunofluorescence staining as described previously for collagen gels [161, 162], to detect β -III-tubulin positive neurons and S100-positive Schwann cells.

2.3.16 Analysis of angle of deviation

Confocal microscopy (Leica SP5) was used in the assessment of d-hDPSC alignment in EngNT, and d-hDPSC and neurite alignment and growth in the EngNT-neuron cocultures. Four equivalent fields were analyzed per gel using a predetermined sampling protocol. The total area sampled per gel was 0.49 mm². Images were captured using a 40 oil immersion lens, and z-stacks were 20 μ m, with a step size of 1 μ m. Image analysis was conducted using Volocity software (PerkinElmer, Waltham, MA, USA) running automated 3D image analysis protocols to measure the angle of Schwann cell alignment and neurite alignment in each field. To evaluate the directional growth of neurites on EngNT containing d-hDPSCs, angles of neurites deviating from the mean d-hDPSC angle in each field were measured.

2.3.17 Statistical analysis

Statistical analysis was performed using GraphPad Prism 5 software (GraphPad, San Diego, CA, USA). Data from the survival assay and neurite outgrowth were first controlled for normality by means of a D'Agostino-Pearson omnibus normality test, followed by comparison of control and experimental groups by means of a

Kruskal-Wallis test while applying a Dunn's multiple comparison *post hoc* test. Data from ELISA tests were submitted to a D'Agostino-Pearson omnibus normality test, followed by an unpaired *t* test. Data from the proliferation assays were compared by means of a 2-way ANOVA followed by Bonferroni's multiple comparison test. Values of $P \leq 0.05$ were considered statistically significant. All data are expressed as means \pm SEM.

2.4 Results

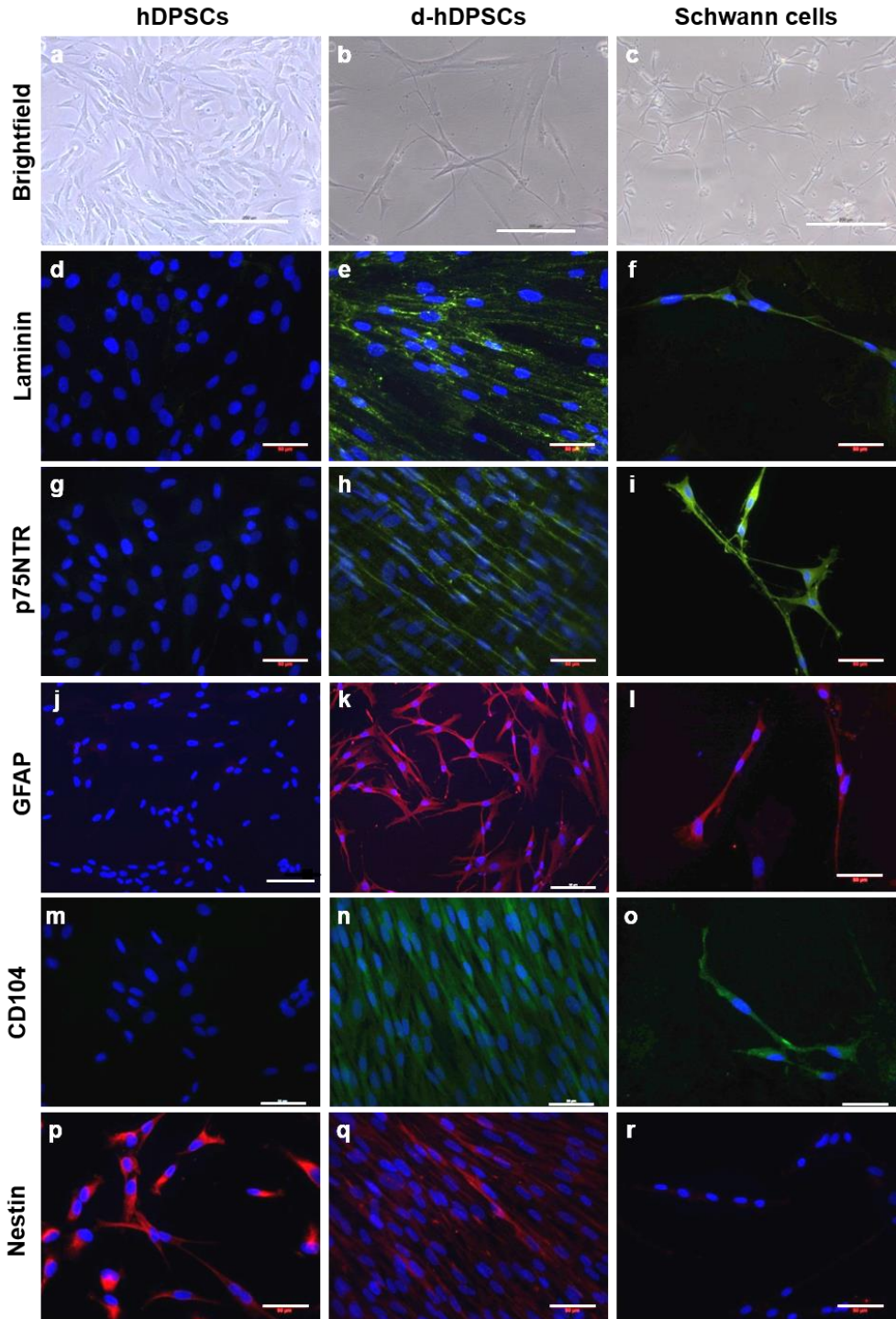
2.4.1 Morphology and immunophenotype of d-hDPSCs *in vitro*

Schwann cell differentiation was induced in hDPSCs at passage 2–3. *In vitro*, undifferentiated hDPSCs displayed a flattened fibroblast-like morphology (Figure 2.1a). After 24 h in differentiation medium containing 1 mM BME, cells adopted an elongated shape. Following the induction protocol, cells acquired a bipolar cell morphology resembling primary rat Schwann cells in culture (Figure 2.1b, c).

To evaluate the expression of glial markers, immunocytochemical staining was performed with antibodies against laminin, p75NTR, GFAP, CD104, and nestin in hDPSCs, d-hDPSCs, and Schwann cells. Both Schwann cells and d-hDPSCs showed a positive immune reaction for laminin, p75NTR, GFAP, and CD104 (Figure 2.1d–o). Furthermore, expression of the early neural marker nestin decreased in differentiated cell cultures compared to hDPSCs and was not detected in Schwann cells (Figure 2.1p–r).

Figure 2.1 (next page): Phenotyping hDPSCs after Schwann cell differentiation.

Brightfield imaging (a–c) and immunocytochemistry (d–r) were performed on hDPSCs (a, d, g, j, m, p) and d-hDPSCs (b, e, h, k, n, q) for the typical Schwann cell markers laminin (d–f), p75NTR (g–i), GFAP (j–l), CD104 (m–o), and nestin (p–r). Nuclei were counterstained with DAPI (blue). Primary rat Schwann cells (c, f, i, l, o, r) were used as positive controls for differentiation. Scale bars = 200 μm (a–c); 50 μm (d–i, l–r); 100 μm (j, k).



At the ultrastructural level, hDPSCs and d-hDPSCs displayed large euchromatic nuclei with prominent nucleoli. Within the cytoplasm of hDPSCs, a perinuclear zone was observed containing organelles such as mitochondria, rough endoplasmatic reticulum cisternae, and some Golgi apparatus (Figure 2.2a-c). In cultures of d-hDPSCs, however, organelles were spread throughout the cytoplasm, and cell-cell contacts were often visible between neighboring cells (Figure 2.2d, e; oval).

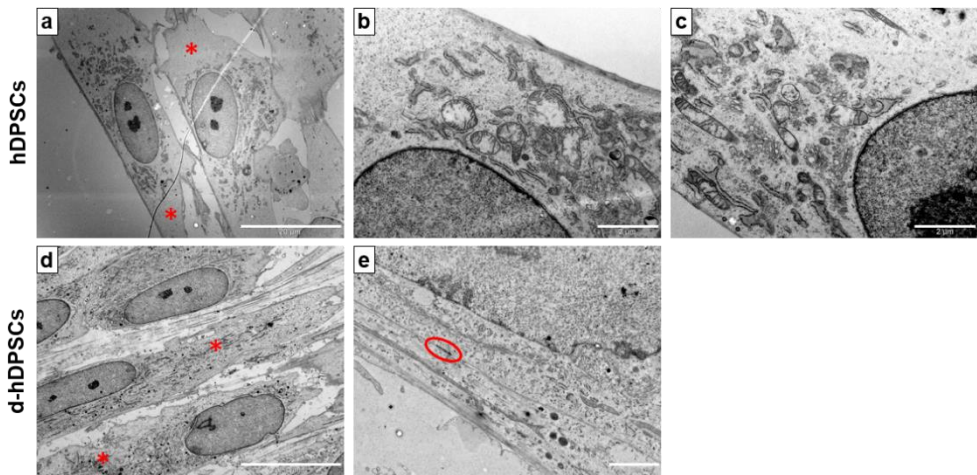


Figure 2.2: Ultrastructural characteristics of hDPSCs and d-hDPSCs. Transmission electron micrographs of hDPSCs (a-c) and d-hDPSCs (d, e) show different distribution of organelles in the cytoplasm (asterisk) and the presence of cell-cell contacts between neighboring d-hDPSCs (e, oval). Scale bars = 20 μm (a, b, d); 2 μm (c, e).

2.4.2 Secretion of neurotrophic factors by hDPSCs and d-hDPSCs

The concentration of GDNF, BDNF, NT-3, and b-NGF, secreted in the conditioned medium of hDPSCs and d-hDPSCs, was determined by means of ELISA (Fig. 2.3a). The levels of BDNF, b-NGF, NT-3, and GDNF were significantly increased after differentiation by 1.60-, 3.68-, 2.02-, and 8.27-fold, respectively.

DRG cultures were incubated with conditioned medium of hDPSCs or d-hDPSCs for 48 h. MTT assays showed a significant increase in the survival of DRG cells

after the addition of conditioned medium from hDPSCs and d-hDPSCs (Fig. 2.3b). Furthermore, compared with hDPSCs, a higher percentage of survival was observed in DRG cultures after the addition of conditioned medium from d-hDPSCs. To detect the outgrowth of neurites in DRG cultures following 48 h of incubation with conditioned medium of hDPSCs and d-hDPSCs, immunocytochemical staining for β -III-tubulin was performed. A significant increase in the length of the longest neurite was observed after adding conditioned medium of hDPSCs and d-hDPSCs (Fig. 2.3c). In addition, conditioned medium of d-hDPSCs induced a distinct positive influence on neurite outgrowth compared to conditioned medium of undifferentiated hDPSCs.

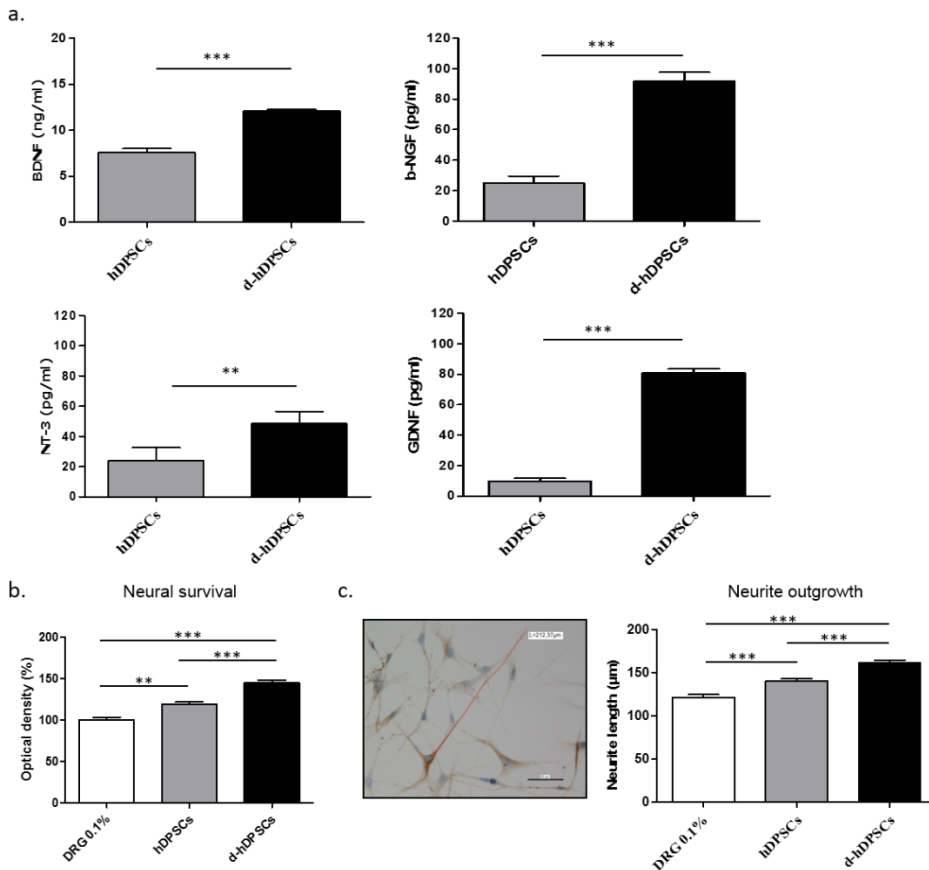


Figure 2.3: Neurotrophic factor secretion by hDPSCs and d-hDPSCs. (a) ELISAs indicated a significant increase in BDNF, b-NGF, NT-3, and GDNF levels after differentiation

(n=9). Neural survival (b; n=7) was assessed by an MTT assay and the length of the longest neurite of individual cells was measured to assess neurite outgrowth (c; n=4). Both were significantly improved with conditioned medium from hDPSCs and d-hDPSCs, with the latter being more potent. Scale bar = 50 μm . Data represent means \pm SEM. **P < 0.01, ***P < 0.001.

2.4.3 d-hDPSCs are aligned in EngNT and guide neurite outgrowth *in vitro*

The capacity of d-hDPSCs to contribute toward a beneficial neuroregenerative environment was assessed *in vitro*. After d-hDPSCs aligned within tethered collagen gels within 4–6 h, constructs were stabilized by removal of interstitial fluid from the hydrogel. This process did not affect d-hDPSC survival (data not shown). Columns of aligned d-hDPSCs within the EngNT were visualized by means of immunofluorescence and confocal microscopy (Figure 2.4a). When dissociated DRG neurons were cultured on top of this aligned cellular material for 3 d, neurite extension along aligned d-hDPSCs was observed (Figure 2.4b–c). The relative frequency distribution of neurite deviation from the mean d-hDPSCs orientation revealed that the majority of neurites (84.11%) deviated with an angle of only 0–30° from the underlying d-hDPSC columns (Figure 2.4d). Neurites growing near perpendicular (80–90°) to the overall direction of aligned d-hDPSCs were not observed.

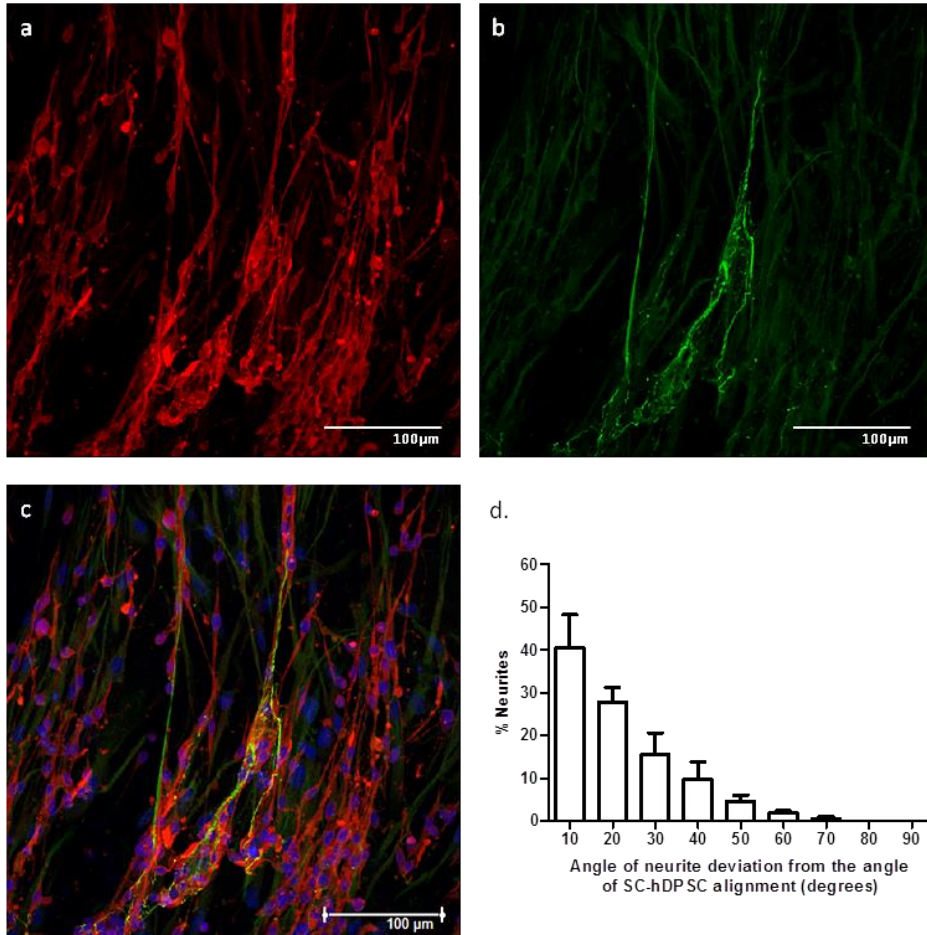


Figure 2.4: d-hDPSC alignment in EngNT guides neurite outgrowth in coculture. (a-c) Confocal images represent d-hDPSCs (S100, red) and neurites (β -III-tubulin, green). Nuclei were counterstained with DAPI (blue). Scale bars = 100 μ m. (d) Frequency distribution of neurite angles compared to mean angle of d-hDPSC alignment in each field (field volume: $9.8 \times 10^6 \mu\text{m}^3$). Data represent means \pm SEM (in 10° bins; $n=4$).

2.4.4 Ultrastructural evaluation of myelination capacity of d-hDPSCs

Three-dimensional cocultures of d-hDPSCs and DRG-derived primary neurons in EngNT were established to assess the myelination capacity of d-hDPSCs. Cytoplasm of both cell types could be easily distinguished based on differential amounts of cell organelles. Neurites were characterized by numerous

mitochondria, whereas dhDPSC cytoplasm was mainly occupied by rough endoplasmic reticulum and free ribosomes. Proximity of d-hDPSCs and neurons resulted in an extensive number of cell-cell contacts (Figure 2.5a). Neurites were engulfed by d-hDPSCs following enfoldment using pseudopodial processes. d-hDPSCs produced myelin sheaths ranging in thickness from 0.1 to 1 μm (Figure 2.5b). Once established, myelin sheaths contained multiple neurites and exhibited typical periodic and intraperiodic lines (Figure 2.5c). Manual counting of the total number of d-hDPSCs and neurites showed that, on average, 20 d-hDPSCs and 172 neurites/ mm^2 hydrogel were present. The total number of neurites consisted of 4 subgroups: neurites that were in contact with d-hDPSCs (14.26%), myelinated neurites (6.42%), neurites that were ensheathed by the cytoplasm of d-hDPSCs (16.40%), and the remaining fraction showing none of the previous characteristics (62.93%) (Figure 2.5d).

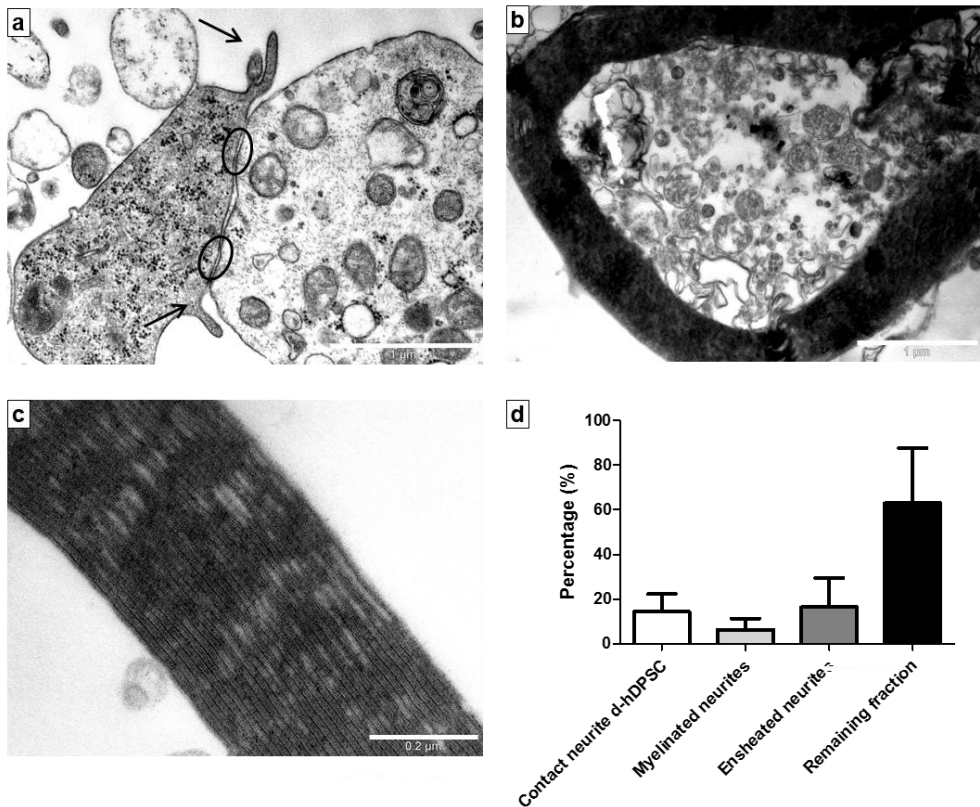


Figure 2.5: Ultrastructural analysis of myelination capacity of d-hDPSCs. (a) Multiple cell-cell contacts (encircled) and enfoldment of neurites by pseudopodial processes of d-hDPSCs (arrows) were frequently observed. Myelin sheaths were present in the culture (b), showing typical periodic and intraperiodic lines (c). (d) Total number of d-hDPSCs and neurites per square millimeter of hydrogel. Scale bars = 1 μm (a, b); 0.2 μm (c).

2.5 Discussion

In the present study, we established a protocol for the differentiation of hDPSCs into cells with a Schwann cell phenotype and functionality *in vitro*. Although several researchers described the possible differentiation of bone marrow-derived MSCs or adipose-derived MSCs toward Schwann cells [144, 163, 164], this is the first time, to our knowledge, that successful differentiation of hDPSCs toward a Schwann cell phenotype has been established and well characterized. Following the differentiation protocol, hDPSCs expressed typical Schwann cell markers and promoted neuronal survival and neurite outgrowth. Moreover, in a 3D coculture model with neurons, d-hDPSCs guided neurite outgrowth and were able to myelinate neurites extended by DRG neurons. Since DPSCs originate from migrating neural crest cells, they are thought to be predisposed toward differentiating into peripheral glial cells under the correct environmental conditions [148-151]. In addition to this neural crest lineage, the high proliferation capacity, multipotency, plasticity, and immunomodulatory properties of DPSCs make them excellent candidates for regenerative medicine purposes, especially in the field of neural tissue engineering [45, 48, 153, 165].

Differentiation of hDPSCs toward Schwann-like cells was induced *in vitro* by the addition of various factors: BME, RA, and growth media supplemented with a cocktail of growth factors containing PDGF $\alpha\alpha$, b-FGF, forskolin, and NRG. BME is known to promote the formation of neurite-like outgrowth [28, 166] as is seen in cell cultures after 24 h administration of BME. RA was used to further induce morphological cell changes, as several reports state that RA together with BME can work as a triggering factor that alters cell morphology. Furthermore, RA induces differentiation of embryonic stem cells into neural cells and regulates the expression of transcription factors that play a role in neural cell determination [155, 167]. An increase in cAMP, and thus an elevated expression of mitogenic genes, can be achieved when cells are treated with forskolin. Taken together, BME and RA have altered cell morphology, and further use of forskolin, b-FGF, PDGF $\alpha\alpha$, and NRG synergistically promote the differentiation of hDPSC into cells with Schwann cell characteristics.

The ultrastructural characteristics of undifferentiated hDPSCs have previously been described [154]. As seen in our cultures, undifferentiated hDPSCs are

fibroblast-like cells containing a perinuclear organelle-rich zone and a peripheral zone lacking any cell organelles. Furthermore no cell-cell contacts and extracellular matrix components were observed [154]. After differentiation, we observed that d-hDPSCs adopted a spindle-shaped bipolar morphology with numerous organelles spread throughout the cell cytoplasm.

To confirm the Schwann cell-like phenotype of differentiated hDPSCs, the expression of multiple markers was evaluated. In order for MSCs to develop toward a neural cell lineage, nestin expression is essential [168]. On differentiation, nestin expression is known to decrease, which is in accordance with the lower levels of nestin seen in d-hDPSCs compared to undifferentiated hDPSCs. Whereas laminin, p75NTR, GFAP, and CD104 expression was hardly detectable in undifferentiated hDPSCs, d-hDPSCs stained strongly positive for these glial markers, similar to Schwann cells. CD104, also known as integrin $\beta 4$, associates with integrin $\beta 6$ to form an adhesion receptor for laminins and is widely expressed by Schwann cells. These results demonstrate the successful morphological differentiation of hDPSCs toward Schwann-like cells.

Previous studies have demonstrated that DPSCs secrete an array of NFs both *in vitro* and *in vivo* and that different neuronal populations exhibit enhanced neuronal survival and neurite outgrowth in the presence of these DPSCs-derived NFs [62-64, 80]. In line with these findings, we observed the secretion of GDNF, BDNF, NT-3, and b-NFG by undifferentiated hDPSCs and their beneficial effects on neuronal survival and neurite length of cultured dissociated DRG neurons. As denervated Schwann cells are known to secrete NFs, and axonal regeneration is reduced in the absence of Schwann cells [169], we predicted that d-hDPSCs would have better neuroprotective and neurotrophic effects than hDPSC. Indeed, not only did significantly more DRG neurons survive with the use of conditioned medium derived from d-hDPSC cultures compared to undifferentiated hDPSCs cultures; an increase in neurite length was also observed.

In the field of neural regeneration, different conduits (natural, synthetic, resorbable, and non-resorbable hydrogels or polymers), in all cases being hollow tubes, have been evaluated to provide guidance for regrowing axons [137]. Although promising results are obtained, these conduits lack the microarchitecture typical of nerve tissue [170]. For optimal nerve regeneration across a long gap, it is important to use a scaffold that mimics key features of the native environment:

Schwann-like cells secreting neurotrophic factors (like denervated Schwann cells in an autograft), Schwann-like cells organized into aligned columns (like bands of Büngner), and Schwann-like cells surrounded by an aligned nanofibrillar collagen extracellular matrix (like the endoneurium).

Since our results showed that hDPSCs were able to differentiate into Schwann-like cells and were capable of secreting NFs that play a role in neural regeneration, we evaluated whether d-hDPSCs were able to self-align in 3D collagen to form EngNT, and whether they could provide guidance for regrowing axons.

After seeding d-hDPSCs in a collagen type I hydrogel, alignment of d-hDPSCs was obtained, and this was stabilized using plastic compression to form EngNT, as previously shown using Schwann cells [97]. This organization of aligned d-hDPSCs in a collagen matrix resembled the bands of Büngner, which are important for accurate guiding of axonal regeneration. Indeed, it has previously been shown that in the process of nerve regeneration, the organization of Schwann cells into columns (bands of Büngner) is of critical importance to guide and support axonal regeneration from the proximal to the distal end of the injury [170]. Cells in a collagen gel will form stable integrin bonds with the collagen fibrils, and then cytoskeletal activity generates forces that contract the gel. EngNT formation as used here exploits this phenomenon; anchoring the ends of a rectangular cellular collagen gel results in development of a longitudinal axis of tension, causing cell elongation and alignment of cells and collagen fibers [97, 142, 143].

The majority of DRG neurites seeded on top of EngNT acquired the direction of aligned d-hDPSCs. In this manner, d-hDPSCs provided a strong guidance cue for neurite growth, which is necessary to promote neural regeneration *in vivo*. Our results were similar to previous studies where aligned glial cell environments supported and guided neurite growth *in vitro* [8, 143, 171, 172]. The aligned cells rather than the collagen matrix are likely to be the main contributor to the promotion of neurite growth, since a previous study showed that little outgrowth was detected in decellularized and acellular constructs compared to EngNT containing live Schwann cells [143].

Tethered hydrogels were used to establish 3D cocultures of DRG neurons and d-hDPSCs to investigate the myelination capacity of the latter. Although the majority of neurites were not myelinated, a close apposition between cellular extensions of d-hDPSCs and neurons was frequently observed. Often these areas were

characterized by the presence of multiple cell junctions, which, in turn, might represent the initiating step of the myelination process [173]. The *in vitro* model used here showed that when neurons and d-hDPSCs were cultured together within a 3D hydrogel environment, the d-hDPSCs spontaneously ensheathed neurites and, in some cases, generated myelin structures, both characteristics that would be associated with neuron - Schwann cell interactions *in vivo*.

In the present study, hDPSCs were successfully differentiated toward Schwann-like cells both on the morphological and functional level. d-hDPSCs expressed characteristic Schwann cell markers, promoted neurite outgrowth in 2D and 3D culture environments, and exhibited typical Schwann cell interactions with neurons, such as ensheathment and myelination of neurites. These features, coupled with their potential clinical availability and utility as a component of tissue engineered constructs, make hDPSCs promising candidates for investigation as cell-based therapies in peripheral nerve injury.

Chapter 3

The potential of Schwann cell differentiated human dental pulp stem cells as a treatment for peripheral nerve injury

Based on:

Regenerating peripheral nerves: the potential of Schwann cell differentiated human dental pulp stem cells

Sanen K, Martens W, Georgiou M, Ameloot M, Lambrichts I, James Phillips

In preparation

3.1 Abstract

Despite the spontaneous regenerative capacity of the peripheral nervous system (PNS), large gap peripheral nerve injuries (PNI) require bridging strategies. The limitations and suboptimal results obtained with autografts or hollow nerve conduits in the clinic urge the need for alternative treatments. Recently, we have described promising neuroregenerative capacities of Schwann cell differentiated human dental pulp stem cells (d-hDPSCs) *in vitro*. Here, we extended the *in vitro* assays to show the pro-angiogenic effects of d-hDPSCs such as enhanced endothelial cell proliferation, migration and differentiation. In addition, for the first time we evaluated the performance of d-hDPSCs in an *in vivo* rat model of PNI. 8 weeks after transplantation of engineered neural tissue containing d-hDPSCs in 15 mm rat sciatic nerve defects, immunohistochemistry and ultrastructural analysis revealed ingrowing neurites, myelinated nerve fibers and blood vessels along the construct. Although further research is required to optimize the delivery of this engineered neural tissue and the timing of complete nerve regeneration, our findings suggest that d-hDPSCs are able to exert a positive effect in the regeneration of nerve tissue *in vivo*.

3.2 Introduction

Peripheral nerve injury (PNI) represents a major clinical concern worldwide and has significant socio-economic impact, causing pain and restriction in daily activities of affected individuals. Although endogenous peripheral nerve regeneration is possible, it is a slow and therefore often incomplete process [15, 16]. Many attempts have been made to accelerate neural regeneration and improve functional outcomes. The preferred therapy for PNI is primary end-to-end suturing. However, for large nerve gaps, when tension-free joining of the proximal and distal nerve stumps is excluded, autologous nerve grafting is regarded as the gold standard [18, 19]. Nerve autografts provide aligned autologous denervated Schwann cells in an aligned extracellular matrix, the predominant structural component of which is collagen type I. Nevertheless, since morphometric mismatch between graft and native nerve is a frequent occurrence, optimal recovery is often restrained [174]. Furthermore, autografting raises additional problems such as donor site morbidity, limited availability of donor tissue and extra time and cost of the second surgical procedure [175]. In search for alternative strategies to treat PNI, a wide range of natural and synthetic biomaterials have been developed, with collagen type I being the most commonly used natural polymer, and combined with Schwann cells or stem cells in order to mimic the key features of the autograft [94, 141, 176].

In the development of artificial nerve tissue, the use of a cellular scaffold that mimics the native tissue environment in the autograft is common. Numerous techniques have been applied to recreate the highly oriented cellular and extracellular matrix architecture of peripheral nerves. Gravity or pressure-driven flow, magnetic fields and electrical gradients can establish alignment of collagen type I fibrils in hydrogels [106-108, 110]. Instead of relying on external forces to orient the extracellular matrix, a recent technique described the self-alignment of collagen fibrils and Schwann cells by using a uniaxially tethered cellular hydrogel system [143]. Following plastic compression (i.e. removal of interstitial fluid from hyperhydrated scaffolds by unconfined compression) to stabilize the construct, the resulting engineered neural tissue (EngNT) has been shown to support and guide neuronal growth both *in vitro* and *in vivo* when seeded with rat Schwann cells [143]. To facilitate clinical translation of this potential therapy for PNI, the

use of an autologous cell source is preferred. Despite the apparent ideal profile of autologous Schwann cells, their isolation is rather invasive and their expansion is difficult. Furthermore, to obtain alignment of cells in constrained hydrogels, cells need to be able to exert a certain level of contractility, a characteristic that is limited in primary glial cell cultures [171, 177]. In search of alternative cell sources, mesenchymal stem cells have shown to be promising candidates for regenerative medicine purposes.

Dental pulp stem cells (DPSCs) represent an easily accessible source of adult stem cells as they can be isolated from extracted wisdom teeth [40]. The proliferative and immunomodulatory properties of DPSCs are more pronounced compared to bone marrow-derived mesenchymal stem cells [45], which enforces their therapeutic potential. Furthermore, their neural crest origin has triggered extensive research on the neurogenic differentiation potential of DPSCs [52, 59, 67, 76]. Recently, we described the *in vitro* differentiation of human DPSCs (hDPSCs) toward Schwann-like cells (d-hDPSCs) [178]. In addition to successful morphological differentiation, the *in vitro* functionality of d-hDPSCs was confirmed as they not only promoted neuronal survival, but also directed neurite outgrowth and myelinated axons in self-aligned 3D co-cultures. These promising data are a first indication that d-hDPSCs could be used as an alternative Schwann cell source for the construction of artificial neural tissue for the treatment of PNI. However, additional research is required in order to potentiate therapeutic application of d-hDPSCs.

The survival of transplanted cells in bioengineered scaffolds depends, amongst others, on adequate (neo-) vascularization of the construct. Vascular endothelial growth factor (VEGF) is best known for its angiogenic properties such as inducing endothelial cell proliferation and migration and stimulating blood vessel formation [179]. However, VEGF has also been reported to exert direct effects on neurons and glial cells by offering neuroprotection and enhancing Schwann cell invasion and axonal outgrowth [180]. Therefore, a VEGF-secreting cell population could have therapeutic benefits in peripheral nerve repair. Although studies have described the expression of VEGF by hDPSCs [181-184], the positive impact of hDPSCs on endothelial cell proliferation and tube formation was described only recently [185]. In addition, both the capillary density of skeletal muscles and

intra-epidermal nerve fiber density of diabetic rats was significantly ameliorated upon transplantation of DPSCs into skeletal muscles [186].

This initial study investigated the use of d-hDPSCs as a cell-based therapy for peripheral nerve repair. First, the paracrine angiogenic properties of d-hDPSCs were investigated at the level of endothelial proliferation, migration and tube formation. Next, EngNT constructs containing d-hDPSCs (d-hDPSC-EngNT) were transplanted in an *in vivo* model of large gap PNI and the regenerated nerve tissue was evaluated for the presence of neurites, myelinated axons and blood vessels.

3.3 Materials and methods

3.3.1 Materials and products

All products were purchased from Sigma-Aldrich (Bornem, Belgium) unless stated otherwise.

3.3.2 Cell culture in 2D and 3D

Human third molars were collected from donors (15-20 years of age) undergoing extraction for orthodontic or therapeutic reasons at Ziekenhuis Oost-Limburg, Genk, Belgium. The medical ethical committee of Ziekenhuis Oost-Limburg approved this study and written informed consent from all donors, or from legal guardians in case of under-aged donors, was obtained. hDPSCs were isolated and differentiated toward Schwann-like cells (d-hDPSCs) in 2D conditions as described previously [178]. hDPSCs were maintained in minimal essential medium, a modification (αMEM) supplemented with 10% fetal bovine serum (FBS, Biochrom AG, Berlin, Germany), 2 mM L-glutamine, 100 U/ml penicillin, and 100 µg/ml streptomycin, further referred to as standard cultured medium. After the induction of differentiation, d-hDPSCs were cultured in complete differentiation medium, which is standard culture medium supplemented with 5 µM forskolin, 10 ng/ml basic fibroblast growth factor (b-FGF), 5 ng/ml platelet-derived growth factor AA (PDGF_{aa}), and 200 ng/ml heregulin-β-1 (NRG) (Immunotools, Friesoythe, Germany).

A human microvascular endothelial cell line (HMEC-1) was purchased from the Center of Disease Control and Prevention (Atlanta, GA). The cells were cultured in MCDB 131 medium (Invitrogen, Carlsbad, CA) supplemented with 100 U/ml Penicillin and 100 µg/ml Streptomycin, 10 mM L-glutamine, 10% FBS, 10 ng/ml human epidermal growth factor (hEGF, Immunotools, Germany) and 1 µg/ml hydrocortisone (Immunotools).

3.3.3 Collection of conditioned medium and ELISA

Donor-matched hDPSCs or d-hDPSCs were seeded at a density of 20,000 cells/cm² in standard or complete differentiation culture medium respectively. After 24 h, cells were washed 3 times in PBS and fed fresh standard culture medium

containing 0.1% FBS. Another 48 h later, the medium was collected and stored at -80°C.

An enzyme-linked immunosorbent assay (ELISA) was performed on conditioned medium in order to determine the concentration of VEGF-A produced by hDPSCs and d-hDPSCs (RayBiotech, Inc., Boechout, Belgium). Experiments were performed in triplicate and absorbance was measured at 450 nm by means of the FLUOstar Optima multifunctional microplate reader (BMG Labtech, Germany). Conditioned medium from 4 different donors was used and ELISA was performed according to the manufacturer's protocol.

3.3.4 Alamar Blue cell proliferation assay

HMEC-1 were seeded in a 96-well plate at a density of 10,000 cells per well in standard MBEC culture medium. After attachment to the culture plate, cells were rinsed with PBS and incubated with conditioned medium for 24, 48 or 72 h. α MEM with 0.1% FBS was used as negative control. Alamar Blue solution ® Cell Viability Reagent (Invitrogen, Carlsbad, CA) was added 4 h prior to readout according to the manufacturer's instructions (AlamarBlue® Cell Viability Reagent, Invitrogen, Carlsbad, CA). 100 μ l of the solution was transferred to a black, clear-bottom 96 well plate and fluorescence (excitation 570 nm, emission 590 nm) was measured using a FLUOstar OPTIMA microplate reader.

3.3.5 Transwell migration assay

HMEC-1 were seeded in tissue culture inserts (ThinCert™, 8 μ m pore size, Greiner Bio-One, Frickenhausen, Germany) at 100,000 cells/cm² in standard hDPSC culture medium containing 0.1% FBS and placed into a 24-well plate. Underneath the tissue culture inserts, conditioned medium from hDPSCs or d-hDPSCs was added. Standard hDPSC culture medium containing 10% FBS or 0.1% FBS was used as a positive and negative control respectively. Following 24h of incubation, transmigrated HMEC-1 were fixed with 4% PFA in PBS and stained with 0.1% crystal violet in 70% ethanol. Cells on the surface of the upper chamber were gently removed with a cotton swab. Per insert, two representative pictures were taken with an inverted phase-contrast microscope (Nikon Eclipse TS100, Nikon co., Japan) equipped with a ProgRes® C3 digital microscope camera (Jenoptik AG, Jena, Germany). The amount of migration (segmentation) based on stained cells

expressed as mean area percent) was quantified using AxioVision software 4.6.3 (Carl Zeiss Vision, Aalen, Germany).

3.3.6 Tube formation assay

In order to evaluate the effect of hDPSCs and d-hDPSCs on tubulogenesis, a tube formation assay (in vitro angiogenesis assay kit, Millipore) was performed. When cultured on ECMatrix™, a solid gel of basement proteins prepared from the Engelbreth Holm–Swarm mouse tumor, endothelial cells rapidly align and form hollow tube-like structures. ECMatrix™ was prepared in 96-well plates as described by the manufacturer, and 15,000 HMEC-1 were plated onto the surface in the presence of conditioned medium from hDPSCs or d-hDPSCs. Standard hDPSCs culture medium containing 10% FBS and 0.1% FBS was used as a positive and negative control, respectively. HMEC-1 were allowed to attach for 4 h before tube formation was evaluated by an inverted phase-contrast microscope (Nikon Eclipse TS100) equipped with a ProgRes® C3 digital microscope camera (Jenoptik AG). Three random fields from each well were captured and analyzed using Angiogenesis Analyzer (ImageJ) for the number of branching points, total network length (continuously joined end-end cells) and the number of closed polygon-shaped structures (mesh size).

3.3.7 Preparation of EngNT containing d-hDPSCs

Gels were prepared as described previously (section 3.3.2) with some modifications. One ml of the collagen solution containing 1 million d-hDPSCs was cast within an ice-cold rectangular stainless steel mould and tethered at each end through the use of a porous mesh. The gels were allowed to set for 15 min at 37 °C after which they were immersed with standard culture medium. Tethered gels were kept at 37 °C in a humidified atmosphere containing 5% CO₂ for 24 h to allow alignment of d-hDPSCs, after which they were stabilised by plastic compression [159]. The resulting 40 µm thick sheets of EngNT were rolled up to form rods (approximately 200 µm diameter × 15 mm length) and kept in standard culture medium until transplantation into animals suffering from sciatic nerve injury (section 3.9).

3.3.8 Surgical repair of rat sciatic nerve

All experimental procedures involving animals were conducted in accordance with the UK Animals (Scientific Procedures) Act (1986)/the European Communities Council Directives (86/609/EEC) and approved by the Open University Animal Ethics Advisory Group. Sprague Dawley (250–500 g) rats were deeply anaesthetised by inhalation of isoflurane, the left sciatic nerve of each animal was exposed at mid-thigh level, transected and then either a repair conduit or a nerve graft was positioned between the stumps to produce an inter-stump distance of 15 mm. Conduits or grafts were retained in place using three 10/0 epineurial sutures at each stump, then wounds were closed in layers and animals were allowed to recover for 8 weeks. Neuronal regeneration was assessed across a 15 mm inter-stump distance and included three groups (7 rats in each): (A) empty NeuraWrap™ conduit (18 mm long with 1.5 mm at each end to accommodate proximal and distal stump), (B) two d-hDPSC-EngNT rods (15 mm long) in a NeuraWrap™ sheath (18 mm long) or (C) a 15 mm nerve graft taken from a littermate culled using CO₂ asphyxiation. Animals receiving d-hDPSCs were immunosuppressed by sub-cutaneous injection of Cyclosporine A (15 mg/kg) 24 h prior to the surgery and then daily throughout the recovery period. After 8 weeks, animals were culled using CO₂ asphyxiation and repaired nerves were excised under a dissecting microscope and immersion fixed in 4% PFA at 4°C. The central 3 mm of the repair device was removed and prepared for transmission electron microscopy (TEM) and transverse cryostat sections (10 µm thick) were prepared from the proximal and distal parts of the device and the nerve stumps for immunostaining (Figure 3.5a).

3.3.9 Transmission electron microscopy

Following fixation with 4% PFA, the fixative was gently aspirated with a glass pipette, and tissues were postfixed in 2% osmium tetroxide (Aurion) for 1 h. Subsequently, tissues were dehydrated through a series of graded concentrations of acetone and embedded in araldite according to the popoff method [157]. Semi-thin sections (0.5 µm) were stained with toluidine blue after which they were scanned with a Mirax digital slide scanner (Carl Zeiss Vision, Aalen, Germany). Ultrathin sections (0.06 µm) were mounted on 0.7% formvar coated copper grids

(Aurion), contrasted with 0.5% uranyl acetate and a stabilized solution of lead citrate (both from Laurylab, Saint-Fons Cedex, France), and examined in a Philips EM 208 transmission electron microscope (Philips, Eindhoven, The Netherlands) operated at 80 kV. The microscope was provided with a Morada Soft Imaging System (SIS; Olympus, Tokyo, Japan) camera to acquire high-resolution images of the evaluated samples. The images were processed digitally with iTEM-FEI software (Olympus SIS). The number of blood vessels and myelinated neurites in the whole of each cross-section were quantified manually.

3.3.10 Immunostaining

Prior to the staining, cryosections were washed with PBS and post-fixed in 4% PFA for 10 min at room temperature (RT). Sections were permeabilized with 0.05% Triton-X for 30 min at 4°C and blocked using 5% normal donkey serum in PBS for 30 min at RT. A mouse monoclonal anti-neurofilament antibody (1:100, DakoCytomation, Glostrup, Denmark) was diluted in 0.2% Triton-X and incubated overnight at 4°C. As secondary antibody, donkey anti-mouse labeled with A555 (1:500, Invitrogen/Molecular probes, Merelbeke, Belgium) was applied for 45 min at RT in the dark. Following nuclear counterstaining using DAPI, slides were mounted with fluorescent mounting medium (Dako, Glostrup, Denmark). Images were taken with a Nikon Eclipse 80i fluorescence microscope equipped with a Nikon digital sight camera DS-2MBWc (Nikon, Tokyo, Japan). Primary antibody was omitted in the negative control condition. To assess axonal growth throughout the EngNT, the total number of neurites was quantified. Pictures were taken covering the whole section and NF-positive neurites were counted manually using Image J software.

3.3.11 Confocal microscopy

To quantify the density of NF growth within the EngNT group, high quality overview images were obtained from cryosections of the mid-proximal part. Imaging was performed using a Zeiss LSM510 META (Carl Zeiss, Jena, Germany) mounted on an Axiovert 200M and a 40x /1.1 water immersion objective (LD C-Apochromat 40 /1.1W Korr UV-VIS-IR, Carl Zeiss), yielding a pixel size of 0.439 µm. The Alexa 555 fluorophore was excited with the 543 nm emission line of a He-Ne laser and internally detected after passing a 560 nm long pass filter. DAPI

excitation was achieved by two-photon excitation at 720 nm performed by a MaiTai laser (Spectra- Physics, CA, USA) and when transmitted through a 37.5 nm wide band pass filter with a central wavelength of 427.5 nm, emitted light was captured by an analogue photomultiplier tube (Zeiss). Four z-stacks spanning 9 μm of the slice were acquired (z-resolution of 0.89 μm) and tiled together to produce a mosaic of image z-stacks that spanned the entire cryosection. 3D images were compressed to a single image using Image J. Next, sections were subdivided into three zones (d-hDPSC-EngNT material; 25 μm border around each d-hDPSC-EngNT rod; remaining area within conduit) to assess the location of neurites in relation to the d-hDPSC-EngNT. The density of neurites in each zone was measured using Image J software analysis and expressed as mean grey value.

3.3.12 Statistical analysis

Statistical analysis was performed using GraphPad Prism 5 software (GraphPad, San Diego, CA, USA). Data from the VEGF-A ELISA were submitted to a D'Agostino-Pearson omnibus normality test, followed by an unpaired t test. Data from the proliferation assay, neurofilament stainings were compared by means of a 2-way ANOVA followed by Bonferroni's multiple comparison test. Data from the migration and tube formation assay and the blood vessel and myelin counting were first controlled for normality by means of a D'Agostino-Pearson omnibus normality test, followed by comparison of control and experimental groups by means of a Kruskal-Wallis test while applying a Dunn's multiple comparison *post hoc* test. Values of $P \leq 0.05$ were considered statistically significant. All data are expressed as means \pm SEM.

3.4 Results

3.4.1 Expression of VEGF-A by hDPSCs and d-hDPSCs *in vitro*

In our previous study [178], we identified a range of neurotrophic factors to be differentially expressed by d-hDPSCs compared to hDPSCs. Here, we evaluated the expression level of the angiogenic factor VEGF-A between both cell populations. ELISA revealed that d-hDPSCs secreted a significantly higher concentration of VEGF-A compared to hDPSCs (Figure 3.1).

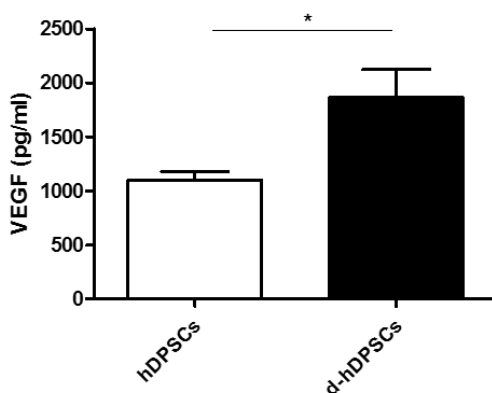


Figure 3.1: Expression of the angiogenic factor VEGF-A by hDPSCs and d-hDPSCs *in vitro*. ELISA indicated a significant increase in VEGF-A release over 48 h *in vitro* after differentiation of hDPSCs toward Schwann cells. Data represent means \pm SEM (n = 4 donors). *P < 0.05.

3.4.2 Angiogenic properties of d-hDPSCs *in vitro*

Angiogenesis is a well-coordinated process involving endothelial cell proliferation, migration and differentiation. Therefore, the potential effects of factors secreted by d-hDPSCs on each of these endothelial cell behaviors were evaluated using a series of *in vitro* assays. First, the proliferation-promoting capacity of d-hDPSCs was evaluated using an Alamar Blue assay. The results in Figure 3.2 show that after 72 h, the endothelial cell line HMEC-1 had proliferated significantly more in the presence of conditioned medium from hDPSCs and d-hDPSCs compared to those in control medium.

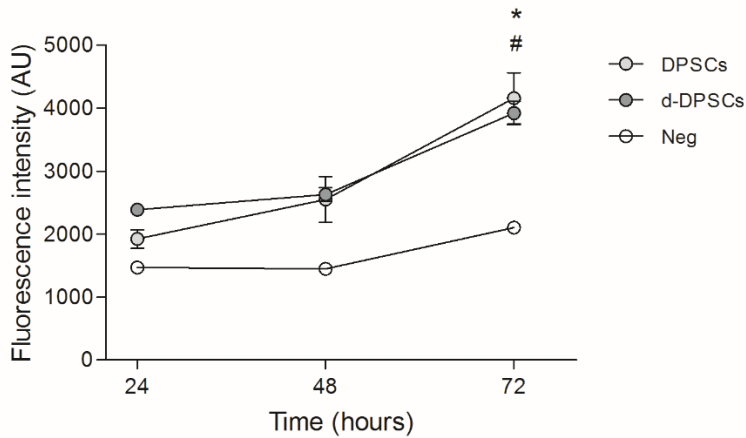


Figure 3.2: Effect of hDPSCs and d-hDPSCs on endothelial cell proliferation.

Endothelial cells were incubated for 24, 48 or 72 h with conditioned medium for hDPSCs or d-hDPSCs. Negative control (neg) is culture medium containing 0.1% FCS. Endothelial cell proliferation was measured using an Alamar Blue fluorescence assay. Data represent means \pm SEM (n = 4 donors). $P < 0.05$ for hDPSCs (*) or d-hDPSCs (#) compared to the negative control at that time point. The error bars may be smaller than the symbol.

Since endothelial cells migrate to the site that is in need of new vascular supply in response to chemical stimuli, the chemotactic potential of d-hDPSCs was examined. In the transwell migration assay, HMEC-1 showed significantly increased transmigration in the presence of conditioned medium from hDPSCs and d-hDPSCs compared to those in control medium (Figure 3.3a-b).

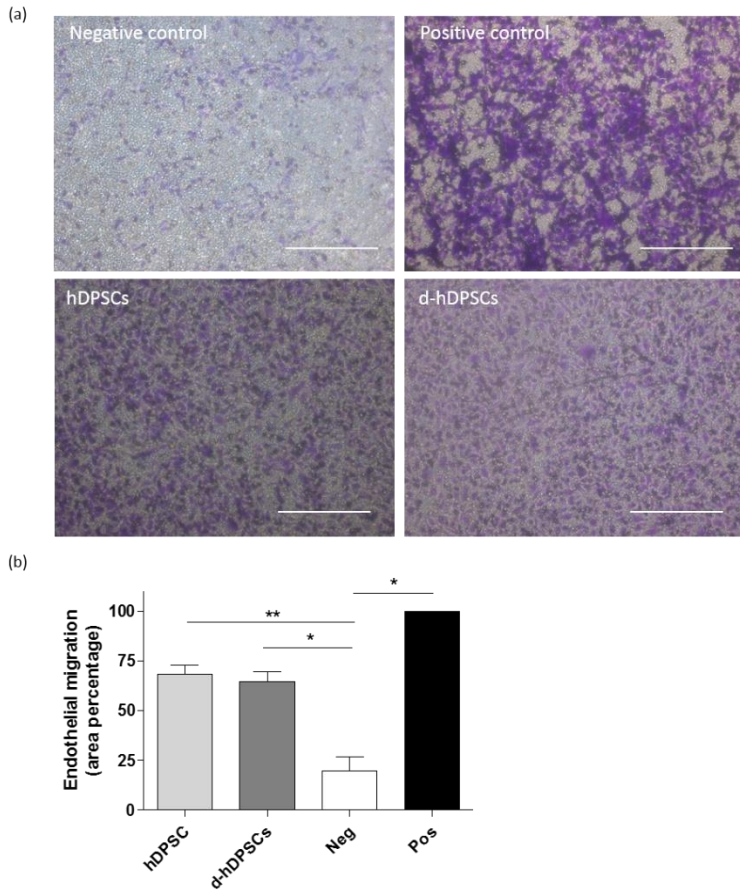
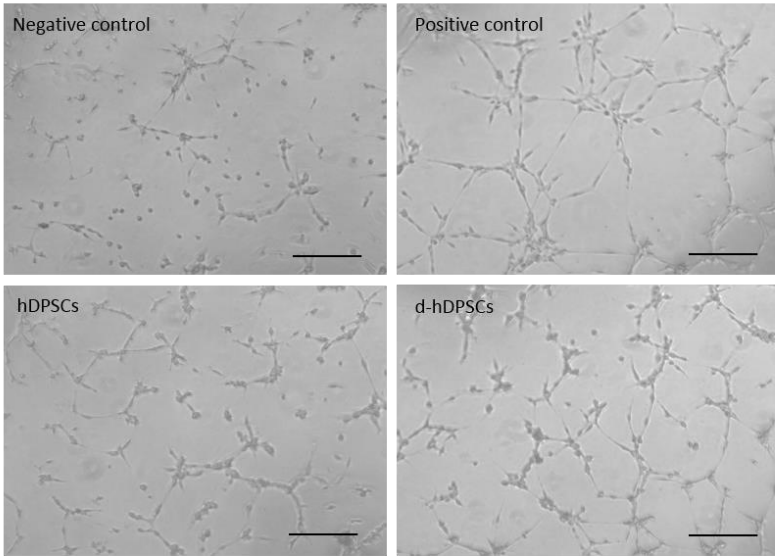


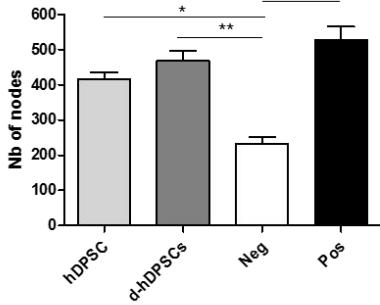
Figure 3.3: Effect of hDPSCs and d-hDPSCs on endothelial cell migration. (a) Representative micrographs show endothelial cell transmigration following 24 h of incubation with conditioned medium from hDPSCs or d-hDPSCs. Culture medium containing 10% FBS or 0.1% FBS was included as positive and negative control respectively. Scale bars = 200 μ m. **(b)** Endothelial cell transmigration expressed as the mean area percentage per condition. Data represent means \pm SEM ($n = 4$ donors). * $P < 0.05$, ** $P < 0.01$.

Finally, an ECMatrix™ assay was performed to assess the effect of d-hDPSCs on endothelial tube formation. Following 24 h incubation of HMEC-1 seeded in ECMatrix™, the conditioned medium of hDPSCs and d-hDPSCs significantly increased the number of nodes, segments and meshes (Figure 3.4a-d). Furthermore, the total branching length of endothelial tubes was significantly longer in these conditions compared to the negative control (Figure 3.4e).

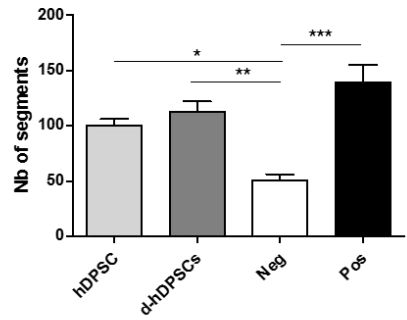
(a)



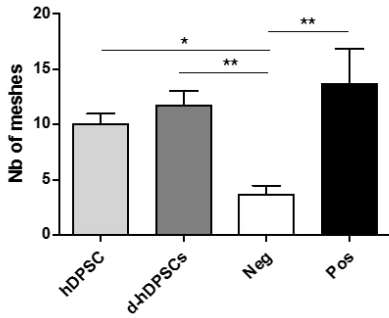
(b)



(c)



(d)



(e)

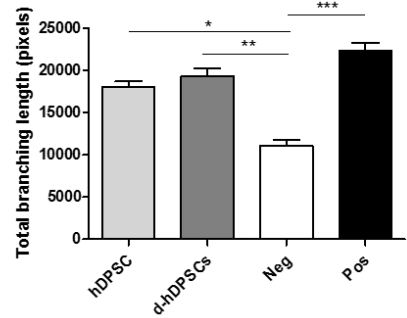


Figure 3.4: Effect of hDPSCs and d-hDPSCs on endothelial tubulogenesis. (a) Representative micrographs show endothelial cell tube formation following 24 h of incubation with conditioned medium from hDPSCs or d-hDPSCs. Culture medium containing 10% FBS or 0.1% FBS was included as positive and negative control respectively. Scale bars = 300 μm . The average number of nodes (b), segments (c) and meshes (d) and the total branching length (e) was measured for each condition. Data represent means \pm SEM (n = 4 donors). *P < 0.05, **P < 0.01, ***P < 0.001.

3.4.3 Nerve repair

d-hDPSCs were seeded in uniaxial tethered collagen type I hydrogels. Following self-alignment, the gels were stabilized by plastic compression and rolled into rods, of which two were placed within NeuraWrap™ conduits. Adult rats with a 15 mm sciatic nerve gap received either d-hDPSC-EngNT, empty conduit or allograft transplants. Following an 8 week recovery period, specific parts of the excised transplants were processed for transverse cryosectioning and subsequent immunofluorescence staining to detect neurofilament (Figure 3.5a). For each group, the number of neurites in the mid-proximal and mid-distal part of the construct were normalized to the number of neurites in the proximal nerve stump, which was set at 100% (Figure 3.5b). In the empty conduit group, only about half of the neurites reached the mid-proximal part of the construct (54.2%), which was significantly fewer compared to the allograft group (85.4%). The number of neurites in the d-hDPSC-EngNT group at this level was 78.3% of the neurites in the proximal stump. In the mid-distal part of the transplants, the level of neurite regeneration in the allograft group was approximately 2.5-fold higher than the EngNT and empty conduit groups. In order to capture the transverse distribution of regeneration within the d-hDPSC-EngNT constructs (mid-proximal and mid-distal part), the density of neurites in three different zones was determined: zone 1 comprised the d-hDPSC-EngNT rods, a border of 25 μm adjacent to the rod defined zone 2 and the remainder of the construct lumen (NeuraWrap™ excluded) was zone 3 (Figure 3.5c). No significant differences between the three zones were observed, although zone 2 showed a trend for higher mean grey values (relative to the density of neurofilament immunoreactivity) compared to the other zones (Figure 3.5d).

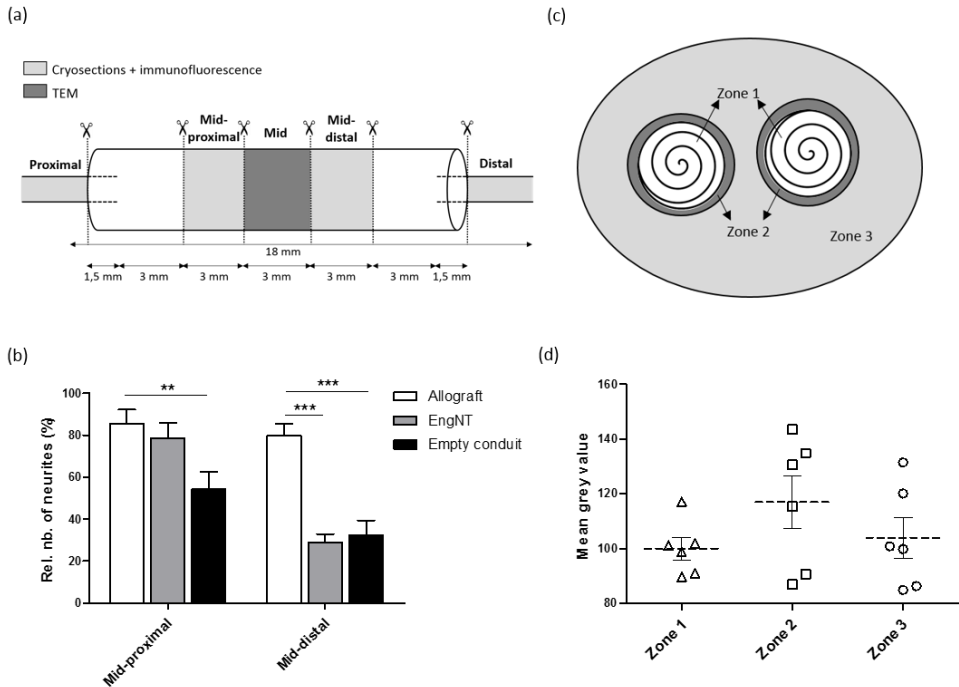


Figure 3.5: Quantification of nerve regeneration by repair devices and allografts.

(a) Schematic representation of 15 mm transplanted construct (allograft: $n = 7$; empty conduit: $n = 7$; or d-hDPSC-EngNT: $n = 5$) with indications on transverse sectioning for post-processing. **(b)** Nerve regeneration throughout the constructs was assessed by means of neurofilament fluorescence staining on transverse cryosections. The number of neurofilament positive axons in the mid-proximal and mid-distal part of the constructs were counted and compared to the number of axons detected in the proximal part of the conduit (expressed as percentage of proximal part). **(c)** Schematic representation of transverse section of two d-hDPSC-EngNT rods in a NeuroWrap™ sheath with indications of different zones in which the number of axons per unit area were quantified: zone 1= whole d-hDPSC-EngNT rods; zone 2= 25 μm adjacent to d-hDPSC-EngNT rods; zone 3 = rest of the cross-sectional area within the NeuroWrap™ sheath. **(d)** The axon density is represented by the mean grey value of neurofilament fluorescent staining for each zone. Data represent means \pm SEM. ** $P < 0.01$, *** $P < 0.001$.

3.4.4 Blood vessels and myelin

The mid part of the excised transplants (Figure 3.5a, dark grey) were processed for TEM. The analysis of semi-thin sections stained with toluidine blue revealed regenerated nerve tissue throughout the cross-section of the allograft group, the presence of 2 rods and regenerated tissue in the d-hDPSC-EngNT samples and only limited tissue regeneration in the empty conduit group (Figure 3.6a, upper part). At the ultrastructural level (Figure 3.6a, lower part), blood vessels and myelinated nerves in the d-hDPSC-EngNT group were observed within and near an abundant fibrillar extracellular matrix. Although blood vessels and myelinated nerve fibers were also present in the empty conduit samples, collagen type I fibrils were hardly detectable. The numbers of blood vessels and of myelinated fibers were assessed for the whole area of each tissue section (Figure 3.6b-c). The allograft and d-hDPSC-EngNT groups contained significantly more blood vessels compared to the empty conduit group. The number of myelinated neurites was significantly higher in the allograft group, but there was no difference in this measure between the d-hDPSC-EngNT and empty conduit group. Although no correlation was observed between the number of blood vessels and the number of myelinated neurites for any of the groups, the three experimental groups seemed to exhibit different characteristic patterns with regard to numbers of blood vessels and myelinated neurites (Figure 3.6d). Overall, the empty conduit group had low blood vessel and low myelin counts, the d-hDPSC-EngNT group had high blood vessel and low myelin counts and the allograft showed both high blood vessel and high myelin counts.

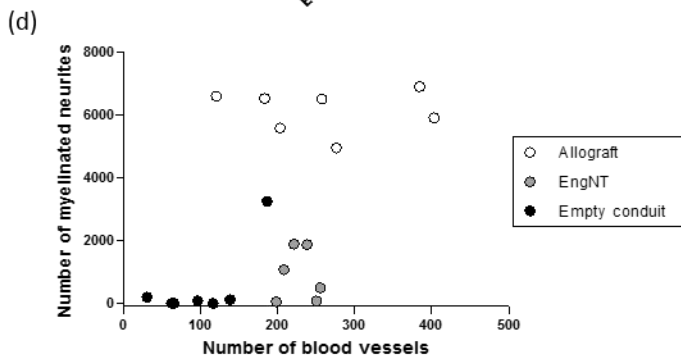
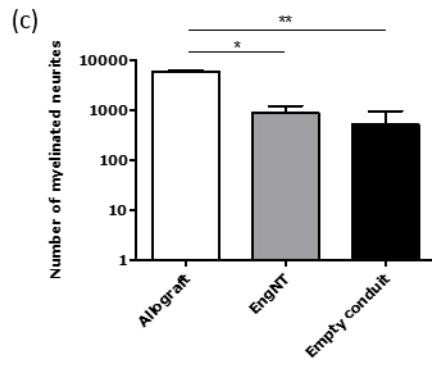
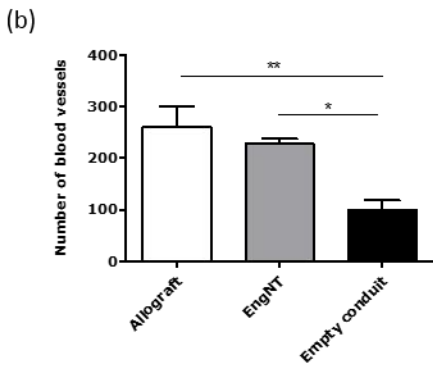
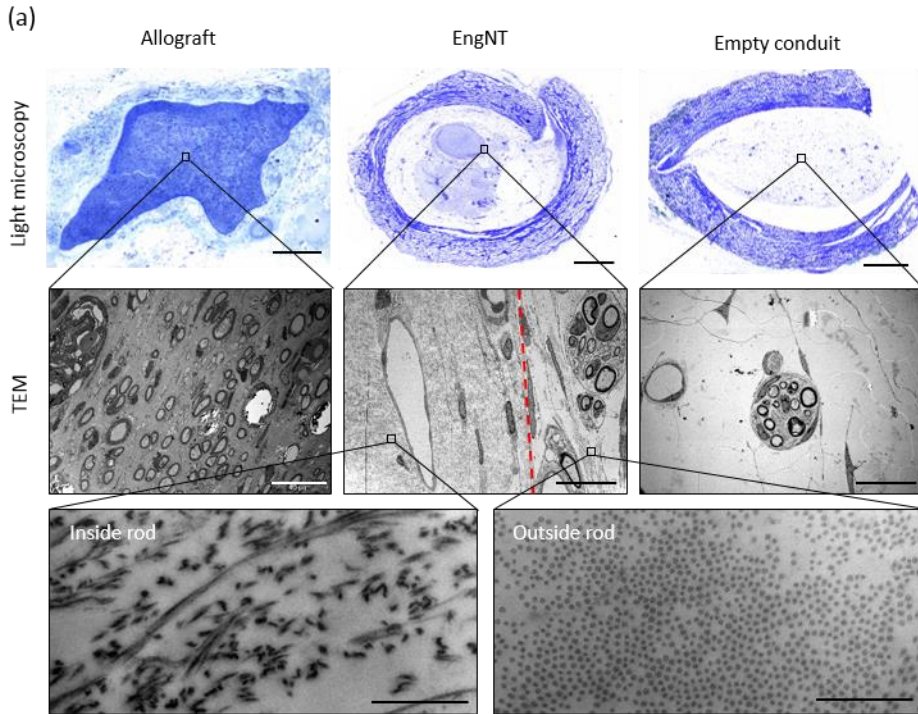


Figure 6: Comparison number of blood vessels and myelinated fibers. The mid parts of the 15 mm conduits were processed for TEM examination. **(a)** Representative semi-thin toluidine blue stained sections (upper row; scale bar = 200 μm for allograft and 500 μm for d-hDPSC-EngNT and empty conduit) and TEM images (scale bars for middle row = 10 μm and for lower row = 1 μm). Red dotted line marks the edge of a cellular hydrogel rod, and representative higher magnification images of collagen fibrils inside and outside a rod are also shown. The number of blood vessels **(b)** and myelinated neurites **(c)** in the whole of each cross-section were quantified manually. A scatter plot **(d)** depicts the mean number of blood vessels and myelinated neurites for every animal that received allograft, d-hDPSC-EngNT or empty conduit transplantation. Data represent means \pm SEM. * $P < 0.05$, ** $P < 0.01$.

3.5 Discussion

A major challenge in the field of neuroscience is the repair of peripheral nerve gaps. In the clinic, different strategies such as autografts, allografts and nerve conduits are employed to join nerve ends and enhance PNS regeneration [95]. Unfortunately, repair outcomes of these bridging approaches are suboptimal [20]. Over the past decades, tissue engineering strategies have been proposed as promising alternatives to reconstruct peripheral nerve defects. A variety of cells and biomaterials have been combined in attempts to provide an adequate environment for nerve regeneration [187]. As already described previously, d-hDPSCs display neuroprotective and neurotrophic properties, can self-align within collagen type I hydrogels and myelinate neurites *in vitro* [178]. In the present study, we assessed the angiogenic properties of d-hDPSCs using *in vitro* assays, then a rat sciatic nerve model of PNI was performed for the first time to further understand the potential for using EngNT containing d-hDPSCs as a regenerative strategy for peripheral nerve lesions.

In the first part of this study, the presence of the pro-angiogenic factor VEGF-A in the conditioned medium of hDPSCs and d-hDPSCs was determined via an ELISA. The results showed that d-hDPSCs secreted approximately 2-fold more VEGF-A compared to hDPSCs. VEGF-A is known to stimulate different steps in the process of blood vessel formation. Recently, research performed by Hilkens *et al.* showed that hDPSCs had a predominant pro-angiogenic impact on endothelial cell migration and tube formation [185], which is confirmed in our study. In addition, we demonstrate that d-hDPSCs have comparable capacities in stimulating the migratory and tubulogenic actions of endothelial cells, indicating that hDPSCs retain their pronounced angiogenic properties following differentiation into Schwann-like cells. Whereas the former publication showed no effect of hDPSCs on endothelial cell proliferation using an MTT (3-(4,5-dimethylthiazol-2-yl)-2,5-diphenyltetrazolium bromide) assay [185], we observed a significant increase in HMEC-1 when incubated with conditioned medium from hDPSCs or d-hDPSCs for 72 h via an Alamar Blue assay. A possible explanation for this discrepancy could lie in the sensitivity of the conducted proliferation assays, since the fluorescence-based readout of the Alamar Blue assay has been reported to provide higher sensitivity compared to the absorbance measurements obtained by MTT assays

[188, 189]. Since several studies have indicated beneficial effects of MSCs on the proliferative capacity of endothelial cells [190-193] and the results obtained for hDPSCs so far are contradictory, it would be of interest to re-evaluate their effect on endothelial cell proliferation. To circumvent interpretation bias of the aforementioned assays due to metabolic changes in HMEC-1 behavior [194], it might be better to conduct future proliferation experiments by means of a Bromodeoxyuridine ELISA [195].

The capacity of d-hDPSC-EngNT to support neuronal growth from the proximal stump *in vivo* was assessed in a rat sciatic nerve injury model. A nerve gap of 15 mm was reconstructed with either nerve allograft, empty conduit or d-hDPSC-EngNT. Eight weeks after transplantation, immunohistochemical analysis of the mid-proximal part of the allograft and d-hDPSC-EngNT constructs revealed comparable neuronal regeneration, whereas less neuronal tissue was observed in the empty conduit treated animals. Regeneration was maintained in distal parts of the allograft, whereas in the d-hDPSC-EngNT transplants the number of neurites in mid-distal regions were lower than in allografts and similar to that of empty conduit transplants. Interestingly, this trend is in contrast to previous research performed with Schwann cells and with differentiated rat adipose-derived stem cells in EngNT, where regeneration was maintained between proximal and distal parts of the implanted constructs [196]. This difference might be attributed to immunosuppressant treatment, administered daily to all the animals in our study and not used in the previous studies where rat cells were used in EngNT. Although hDPSCs have been described to exhibit potent immunomodulatory and anti-inflammatory capacities [45, 46], graft-versus-host responses in rats receiving d-hDPSC-EngNT transplants could not be excluded, so all animals were treated with Cyclosporine A in this study. Both innate and adaptive immune cells have been shown to play a role in clearing myelin and axonal debris and promoting neurite outgrowth [197], and Namavari *et al.* showed that immunomodulation with Cyclosporine A delays axonal sprouting and growth of transected nerves [198].

With regard to the distribution of the regenerating neurites in the EngNT transplants, there was a trend for higher axon densities in the zone directly adjacent to the EngNT rods compared to the surrounding area, which was also a region of high neurite density in the previous study using rat Schwann cells in

EngNT [143]. Since neuronal growth within the rods was lower in this study, one could speculate that the longitudinal permeability of the d-hDPSC-EngNT rods was not optimal for neurite ingrowth. In order to fully exploit the potential of d-hDPSC-EngNT, other ways of incorporating EngNT sheets within the constructs will be examined in the future. For example, a low density hydrogel could be used as a core material to wrap the d-hDPSC-EngNT sheets around, or as an additional spacing layer within the rods. By increasing the total available d-hDPSC-EngNT sheet surface for regenerating axons and facilitating diffusion of neurotrophic factors produced by d-hDPSCs, the growth of neurites into and throughout such constructs might be enhanced.

In the mid part of the construct, the number of blood vessels observed in the d-hDPSC-EngNT and allograft transplants were comparable. Revascularization of nerve grafts, and especially vascular ingrowth from the surrounding tissue bed, is important since ischemia-induced necrosis and fibrosis hamper axonal regeneration [199-201]. Furthermore, transplantation of adipose-derived stem cells has been shown to boost vascularization of the nerve defect [202], which can promote the longevity of the construct. Upon transplantation of d-hDPSC-EngNT, a lack of intrinsic vascular supply creates a hypoxic environment for the encapsulated cells, thereby triggering the upregulation of pro-angiogenic pathways [203]. Because the resulting enhanced vasculature will increase survival chances of the transplanted cells, this is an important component in the provision of subsequent neurotrophic support. The difference in number of regenerated axons between the mid-proximal and the mid-distal part of the d-hDPSC-EngNT constructs indicates that priority may have been given to revascularization and, as a consequence, reinnervation was delayed when compared to allograft controls. Previous studies have demonstrated that longitudinal inosculation is the primary method of revascularisation in allografts, whereby anastomosis occurs between the vessels in the graft and the repaired nerve, accelerating restoration of blood flow without the requirement for angiogenesis [204, 205]. Future improvements to d-hDPSC-EngNT devices could therefore focus on provision of structures that accelerate vascularisation and promote the survival and neurotrophic behaviour of the implanted cells.

In this first study to report the transplantation of human cells in EngNT constructs for peripheral nerve repair, the proximal part of the d-hDPSC-EngNT showed a

comparable amount of neurite regeneration compared to allograft treatment but a lower number of neurites had traversed into the distal part after 8 weeks. This pattern of nerve regeneration was associated with increased vascularisation compared to empty conduits, which was consistent with the pro-angiogenic effects of d-hDPSCs observed *in vitro*. In conclusion, d-hDPSC-EngNT is a promising new approach that showed an ability to enhance vascularisation and to promote initial neurite ingrowth in a long-gap nerve repair scenario. Future work will focus on tuning the cell and material environment to improve regeneration in the distal part of the constructs.

Chapter 4

Label-free mapping of microstructural organization in cellular hydrogels using ICS

Based on:

Label-free mapping of microstructural organization in self-aligning cellular collagen hydrogels using image correlation spectroscopy.

Sanen K, Paesen R, Luyck S, Phillips J, Lambrichts I, Martens W, Ameloot M

Acta Biomaterialia (2015). doi: <http://dx.doi.org/10.1016/j.actbio.2015.10.047>.

IF(2014)=6.025

4.1 Abstract

Hydrogels have emerged as promising biomaterials for regenerative medicine. Despite major advances, tissue engineers have faced challenges in studying the complex dynamics of cell-mediated hydrogel remodelling. Second harmonic generation (SHG) microscopy has been a pivotal tool for non-invasive visualization of collagen type I hydrogels. By taking into account the typical polarization SHG effect, we recently proposed an alternative image correlation spectroscopy (ICS) model to quantify characteristics of randomly oriented collagen fibrils. However, fibril alignment is an important feature in many tissues that needs to be monitored for effective assembly of anisotropic tissue constructs. Here we extended our previous approach to include the orientation distribution of fibrils in cellular hydrogels and show the power of this model in two biologically relevant applications. Using a collagen hydrogel contraction assay, we were able to capture cell-induced hydrogel modifications at the microscopic scale and link these to changes in overall gel dimensions over time. After 24 h, the collagen density was about 3 times higher than the initial density, which was of the same order as the decrease in hydrogel area. We also showed that the orientation parameters recovered from our automated ICS model match values obtained from manual measurements. Furthermore, regions axial to cellular processes aligned at least 1.5 times faster compared with adjacent zones. Being able to capture minor temporal and spatial changes in hydrogel density and collagen fibril orientation, we demonstrated the sensitivity of this extended ICS model to deconstruct a complex environment and support its potential for tissue engineering research.

4.2 Introduction

Hydrogels are three-dimensional (3D) networks formed by natural or synthetic cross-linked polymers. Their high water-absorbing capacity and modifiable biomechanical and biochemical properties make them highly suitable carriers for different cell types [96, 97]. Therefore, many efforts have been made to use hydrogels in tissue engineering applications. By combining multidisciplinary strategies based on material, life and engineering sciences, research in this field aims to restore, preserve or enhance tissue structure and function following injury or disease [206]. Because their stiffness can range from 0.1-500 kPa [99], hydrogels are especially appealing for regenerating soft tissues such as skin, tendons, muscles and nerves [98].

In the past decade, natural hydrogels have gained significant interest due to their native-like extracellular matrix (ECM) properties and inherent biocompatibility [96, 97]. Of all natural polymers, collagen type I has received great attention in tissue engineering as it is the most abundant ECM protein in the human body. Although many tissues such as corneas, vessel walls, tendons and nerves contain collagen type I, their mechanical strength and function are related to specific alignment patterns of these fibrils [207]. In the body, collagen type I is capable of self-aggregation and crosslinking to form a tissue-specific anisotropic ECM. *In vitro* assembly, however, consistently creates a randomly oriented fibrillar hydrogel network [208].

Different methods have been probed to generate aligned collagen hydrogels including drainage [106], microfluidic channels [107] and the use of electrical gradients [108] or magnetic fields [110]. Whereas these scaffolds are organised by being subjected to external mechanical forces, a more natural approach involves uniaxial constrained cell-seeded collagen hydrogels where cell-generated tension causes self-alignment of both cells and collagen fibrils [111, 112]. The use of these highly organised cellular collagen constructs for nerve repair is well studied [143, 178, 196], but little is known about the progression of these cell-induced changes in hydrogel architecture. Live imaging of the formation of aligned tissue-engineered cellular constructs will advance our understanding of the process and provide valuable new information to inform the construction of better 3D hydrogel microenvironments that mimic native ECM. Although many optical

microscopy techniques can visualize individual cells in their ECM, most of them require exogenous dyes which could have phototoxic effects and perturb native cellular behaviour [117]. In order to truly understand ECM remodelling by embedded cells, it is essential to continuously monitor cell-matrix interactions within the 3D construct in a label-free manner.

Collagen type I fibrils are capable of generating two types of intrinsic optical signals: autofluorescence and second harmonic generation (SHG) [209, 210]. Both processes can be induced by femto-second pulsed laser light but the resulting signals differ in wavelength and intensity. The frequency-doubled SHG signal has a much higher signal-to-noise ratio compared to the Stokes-shifted autofluorescence signals [211]. Yielding high contrast and submicron resolution images on a non-invasive basis, SHG microscopy holds great promise in the field of biomedical imaging [212] and tissue engineering [213, 214].

When studying collagen fibril organisation, extraction of quantitative information from these SHG images is not trivial. Often, time consuming manual data extraction is used which might suffer from subjective interpretation. To overcome this possible bias, image correlation spectroscopy (ICS) has been used to predict bulk mechanical properties of collagen hydrogels in an automated and objective manner. By calculating the autocorrelation function (ACF) of a fibrous SHG image, quantitative parameters such as pore size, collagen density, fibril length, thickness and orientation can be extracted [132-135]. Recently, we proposed an alternative ICS model for random fibril orientation which included SHG-specific polarization effects to obtain a more accurate ACF amplitude recovery as shown by simulations and experimental data on a collagen type I hydrogel dilution series [136].

In the current work, we expand our previous approach and describe the extension toward the characterization of cellular self-aligning collagen hydrogels designed for tissue engineering. The power of the extension is demonstrated in two relevant applications. First, we perform a collagen hydrogel contraction assay to evaluate cell-mediated hydrogel changes over time at the macroscopic and microscopic level. We explore the sensitivity of the extended ICS model by using two different but related cell types that can exhibit minor differences in contractile capacity, namely human dental pulp stem cells (hDPSCs) and their glial differentiated derivatives (d-hDPSCs) [178]. Secondly, we examine whether this model can be used to estimate fibril orientation in cellular hydrogels. To test the accuracy of the

Label-free mapping of microstructural organization in cellular hydrogels using ICS

estimated orientation parameters, we implement a validation experiment in which manually obtained and automated (ICS) outcomes are compared. Finally, we apply the ICS model to quantify and map collagen fibril organisation in a self-aligning d-hDPSCs containing hydrogel for neural tissue engineering.

4.3 Materials and methods

4.3.1 Materials and products

All products were purchased from Sigma-Aldrich (Bornem, Belgium) unless stated otherwise.

4.3.2 Cell culture

Human third molars were collected from donors (15-20 years of age) undergoing extraction for orthodontic or therapeutic reasons at Ziekenhuis Oost-Limburg, Genk, Belgium. The medical ethical committee of Ziekenhuis Oost-Limburg approved this study on February 3rd 2014 and written informed consent from all donors, or from legal guardians in case of under-aged donors, was obtained. hDPSCs were isolated, cultured and differentiated toward Schwann-like cells (d-hDPSCs) as described in section 2.3.2.

4.3.3 Aligned cellular hydrogels

A tethered cell-seeded collagen gel was prepared according to methods described previously [158-160, 178] with some modifications. Briefly, gels were prepared on ice by mixing 1 volume of 10x MEM with 8 volumes of type I rat tail collagen (2 mg/ml in 0.6% acetic acid; First Link, Wolverhampton, UK). The pH of the mixture was neutralized dropwise using 1 M sodium hydroxide, after which 1 volume of d-hDPSCs suspension was added to give a final seeding density of 10^6 cells/ml. The resulting mixture was cast within an ice-cold rectangular stainless steel mould (37 mm x 27 mm x 4.5 mm) and tethered at each end through the use of a porous mesh. The gels were allowed to set for 15 min at 37 °C, transferred to a #1.5 glass bottom petri dish and subsequently immersed with standard culture medium. From this moment on ($t = 0$ h after casting), tethered gels with initial dimensions of 16 mm x 6.5 mm x 4.5 mm were kept at 37 °C in a humidified atmosphere containing 5% CO₂ in a cell culture incubator or in the microscope stage incubator for imaging at 0, 4, 8 and 32 h after casting. The orientation of the 3D construct is referred to as x for the long axis of gel, y for the shorter axis and z for the height. The mould was always positioned such that the x-axis of the hydrogel was parallel to the polarization of the incident light, which is always along the x-axis of the image in this paper. Since alignment occurs in the direction of

tension generated by the cellular gel contraction being resisted by the tethering bars, elongated cells and aligned collagen fibrils along the x-axis are expected in the acquired images. Per hydrogel, 6 cells were randomly selected in the central part of the tethered system and around each cell, 3 defined regions near the cellular processes (axial, diagonal and parallel with respect to cellular processes) (Fig. 3a) were imaged. Differentiated hDPSCs from 4 different donors were used to carry out 4 independent experiments ($n = 4$).

4.3.4 Hydrogel contraction assay

Gels were prepared as described above with some modifications. Donor-matched hDPSCs or d-hDPSCs were added to the hydrogel mixture in a final seeding density of 10^6 cells/ml. Cell-seeded collagen hydrogels were cast in duplicate in a 96-well plate (Greiner F-bottom; 75 μ l/well) for six different time points (0, 2, 4, 6, 8 and 24 hours). After 10 min of setting at 37 °C, gels were immersed in 200 μ l standard culture medium and detached from the wells using a fine spatula. Four independent experiments, i.e. cells from four different donors ($n = 4$), were carried out and for each experiment, free-floating hydrogel contraction was assessed both macro- and microscopically at the indicated time points. For macroscopic analysis, the medium was removed and digital images were taken. ImageJ software was used to determine the area of the upper surface of the gels. Collagen gel size was defined as a percentage of the initial hydrogel area. For microscopic analysis, duplicate gels were transferred to μ -Slide 8 Well ibiTreat (Proxylab, Beloeil, Belgium) and 3 random regions without cells in the field of view were imaged in the centre of each hydrogel. For one donor ($n = 1$), also 3 random regions at the edge of each hydrogel were imaged.

4.3.5 Microscopy

Label-free imaging of cell-seeded gels was performed using a Zeiss LSM510 META (Carl Zeiss, Jena, Germany) mounted on an Axiovert 200M. The horizontally polarized excitation was provided by a femtosecond pulsed laser (MaiTai DeepSee, Spectra- Physics, CA, USA) tuned to a central wavelength of 810 nm. The beam was reflected by a short-pass 650 nm dichroic beam splitter and focused onto the sample with a 40x/1.1 water immersion objective (LD C-Apochromat 40x/1.1W Korr UV-VIS-IR, Carl Zeiss). The average excitation power at the sample is

approximately 4 mW. Two-photon excitation (TPE) autofluorescence of the embedded cells and SHG signals from the collagen fibrils were epi-collected, discriminated with a 442 nm dichroic beam splitter and transmitted through a 100 nm or 5 nm wide band pass filter with a central wavelength of 550 nm or 405 nm respectively. An analogue photomultiplier tube (Zeiss) was used for detection in non-descanned mode. Based on our previous work [136], a pixel size of 85 nm was chosen for 1024 x 1024 pixels per image, yielding a field of view of 87 μm x 87 μm which proved to be sufficient to correctly estimate all ACF parameters and provides sufficiently detailed spatial insight in the studied structures. If we would reduce the field of view (FOV), while keeping the pixel size constant, less fibrils are included in the image. Because ICS is a statistical method, lowering the number of fibrils would result in less accurate ACFs, and therefore less representative parameter values would be recovered from the ACF. Conversely, increasing the FOV with fixed pixel size would yield better defined ACFs, but also averages more local spatial variations. The images were taken 20 μm above the cover glass and microscopy was performed at 37 °C.

4.3.6 ACF analysis

The analysis of the ACF is based on the previously described ICS model [136] developed to study hydrogels imaged by SHG. In the extended model used in the current work, the ACF $g(\eta, \xi)$ is modeled by

$$g(\eta, \xi) = g_{00} \left| \sum_{i=1}^N g_{\theta_i}^1(\eta, \xi, L) m(\theta_i) \right| \quad (1)$$

with $g_{\theta_i}^1(\eta, \xi, L)$ the ACF of a single fibril of length L oriented at an angle θ_i relative to the orientation of the polarization direction of the incident light. The angles θ_i are set to be equally spaced at 10 ° intervals between 0 ° and 180 °. The notation $|\dots|$ takes care of the normalization of the sum to unity such that the ACF amplitude is solely defined by g_{00} . The amplitude g_{00} is inversely proportional to the fibril density [136].

The modulation function $m(\theta)$ in eq. (1) accounts for the polarization effect related to SHG imaging and the orientation distribution of the fibrils,

$$m(\theta) = p^2(\theta)\Phi(\theta) \quad (2)$$

with

$$p(\theta) \propto \sin 2\theta + \left(\frac{d_{31}}{d_{15}} \sin^2 \theta + \frac{d_{33}}{d_{15}} \cos^2 \theta \right)^2 \quad (3)$$

where d_{ij} are non-zero second order macroscopic susceptibility tensor elements of the collagen fibrils and where $\Phi(\theta)$ describes the orientation distribution of the fibrils within the image. We assume that the fibril orientations have a Gaussian distribution around the preferential angle μ . To implement the Gaussian distribution as a wrapped distribution function, a circular variant analogue to the so called Von Mises distribution was used. Since the fibrils have no sense, a periodicity of π appears in the ACF. Therefore, the standard Von Mises distribution with a periodicity of 2π must be adjusted to one with half the periodicity. Our implementation of the adjusted Von Mises distribution reads

$$\Phi(\theta) \propto \frac{e^{-\kappa \cos 2(\theta-\mu)}}{I_0(\kappa)} \quad (4)$$

with $I_0(\kappa)$ the zeroth order Bessel function of the first kind, and κ a dimensionless parameter representing the spread of the distribution, being analogue to the inverse of four times the variance of the approximated wrapped Gaussian distribution. This means that for $\kappa = 0$, a uniform distribution is obtained, while for increasing values of κ a Gaussian distribution with a standard deviation of $0.5\kappa^{-0.5}$ is approximated. Note that for both $p(\theta)$ and $\Phi(\theta)$ only the proportionalities are used, since additional factors vanish by the ACF normalization.

In the actual analysis of the experimental ACF, the tensor element ratios are fixed to the values we determined previously.: $d_{31} = 1.5d_{15}$ and $d_{33} = 1.8d_{15}$ [136]. The e^{-2} width of the point spread function was fixed at $0.33 \mu m$. The freely adjustable parameters in the fitting procedure are the ACF amplitude g_{00} , the average fibril length L , the preferential orientation μ and the orientation spread κ . Consistently with our previous work [136], the length always results in values above the detection limit. Therefore, we cannot draw conclusions on the fibril lengths. To account for possible background effects, an additional offset is included in the fitting procedure as well. The fitting is done on the central 64×64 pixels of the ACF. The analysis was done with in house developed Matlab (The MathWorks) routines. The analysis of one ACF takes approximately 10 seconds on a standard pc with a quad-core processor (Intel i5) running at 3.30 GHz.

4.3.7 Validation of ICS analysis for orientation parameters κ and μ

Three random images were collected from the central part of a tethered gel containing d-hDPSCs at each of the indicated time points (see section 4.3.3). To minimize heterogeneity within a SHG image, pictures were captured without cells or their processes in the field of view. For validation purposes, collagen fibrils were traced manually in ImageJ software. For each image, the distribution of fibril orientations was analyzed using the Von Mises distribution given by eq. (4), yielding the mean direction μ and the concentration parameter κ . These parameters were then compared to their corresponding parameters returned by the automated ICS analysis described in section 4.3.6.

4.3.8 Statistical analysis

Statistical analysis was performed using Graphpad Prism 5 software (Graphpad, California, USA). Data from the hydrogel contraction assay and the aligned hydrogel constructs were compared by means of a two-way ANOVA followed by Bonferroni's multiple comparison test. P-values ≤ 0.05 were considered statistically significant (* $p \leq 0.05$; ** $p \leq 0.01$; *** $p \leq 0.001$). All data were expressed as mean \pm Standard Error of the Mean (SEM).

4.4 Results

4.4.1 Differential hydrogel contraction on macro and micro scale

A hydrogel contraction assay was performed to determine the sensitivity of the ICS model in a biologically relevant setting. Since the macroscopic change in overall gel dimensions is a result of cell-level activity [215], it should be possible to link macroscopic observations to microscopic data. Therefore, contraction of collagen type I hydrogels was captured macro- and microscopically for both hDPSCs and d-hDPSCs at six different time points. For macroscopic evaluation, hydrogel contraction was measured from digital pictures (Figure 4.1a; upper row) as a percentage of the initial hydrogel area (Figure 4.1b). While contraction after 2 h was similar for both cell types (~80% of initial area), hydrogels seeded with d-hDPSCs were significantly smaller compared to hydrogels seeded with hDPSCs at 4 h (64% versus 76% of initial area) and 6 h after casting (and 52% vs 65% of initial area). After 24 h, a reduction to ~40% of the original hydrogel size was observed for both cell types.

To evaluate whether this differential macroscopic hydrogel contraction by hDPSCs and d-hDPSCs corresponds to distinct changes in matrix density, SHG imaging of these gels (Figure 4.1a; lower row) with subsequent ICS analysis was performed. Figure 4.1c shows the ACF amplitude g_{00} as function of time. Starting off with the same collagen density directly after casting ($t = 0$ h), a remarkable difference was observed after 2 h where hydrogels seeded with d-hDPSCs showed a significantly lower amplitude compared to gels seeded with hDPSCs. 4 h after hydrogel casting the amplitude was comparable for both conditions but another 2 h later, d-hDPSCs-containing gels had a significantly higher collagen density compared to gels with hDPSCs as indicated by a lower amplitude ($g_{00} = 0.31$ and 0.65 respectively) (Figure 4.1c). In the end, both cellular hydrogels reached a g_{00} value of ~0.30. It must be noted that at the edge of the hydrogel, this minimal ACF amplitude is already reached 2 h after hydrogel casting with hDPSCs and d-hDPSCs (Supplementary Figure 4.4). Although both cell types showed similar patterns for hydrogel contraction (Figure 4.1c, full line), hDPSCs showed a time lag in initiation of central collagen fibril condensation (Figure 4.1c, dotted line). Taken together, the differential decrease in area between hydrogels seeded with

hDPSCs or d-hDPSCs is coupled with proportional increases in collagen density as indicated by the trend of distinctively decreasing g_{00} values.

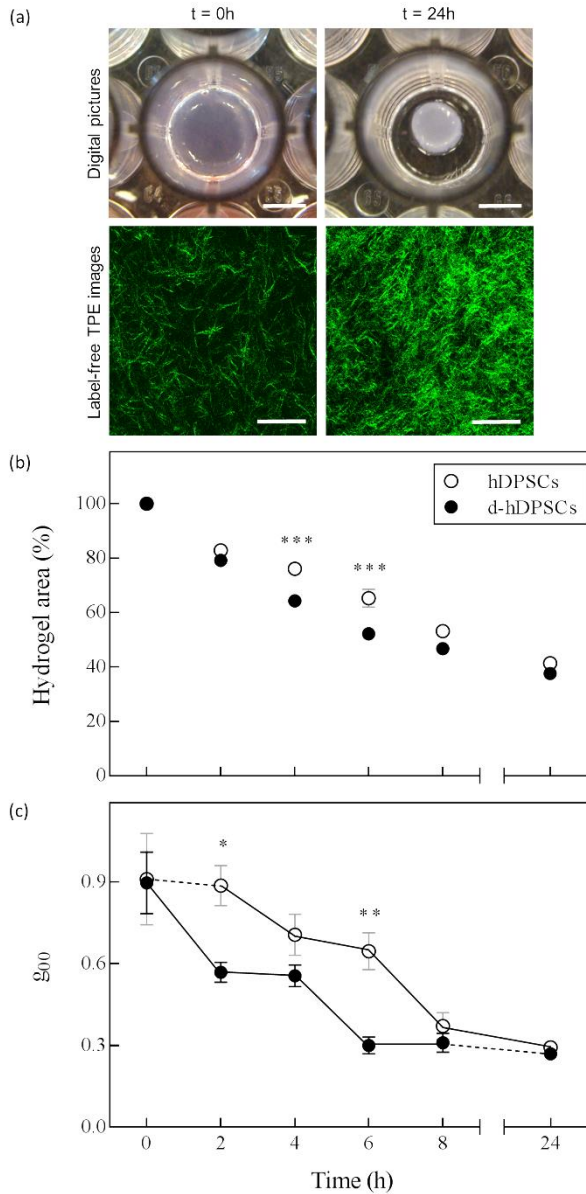


Figure 4.1: Hydrogel contraction assay with hDPSCs or d-hDPSCs. Each free-floating collagen type I hydrogel seeded with (d-)hDPSCs was monitored from directly after hydrogel casting ($t = 0$ h) to the fully contracted stage ($t = 24$ h). **(a)** Digital pictures (scale bars = 3 mm) show the macroscopic changes in hydrogel area while TPE images (scale bars = 20 μm) visualize collagen type I fibrils (green) by SHG signals. **(b)** Macroscopic evaluation was done by measuring the area of the hydrogel from digital images, depicted as percentage of the initial hydrogel area as a function of time. **(c)** Microscopically obtained SHG images with a pixel size of 85 nm and 1024 x 1024 pixels per image (yielding a field of view of 87 μm x 87 μm) were analyzed by the ICS model described in section 4.3.6, of which the ACF amplitude g_{00} is plotted as a function of time. hDPSCs and d-hDPSCs showed similar changes in g_{00} values (full lines) with a small time lag (dotted lines) between both cell types. Data represent means \pm SEM ($n = 4$). * $p < 0.05$, ** $p < 0.01$, *** $p < 0.001$ compared with hDPSCs at each time point. The error bars are often smaller than the symbol.

4.4.2 Validation of orientation parameters

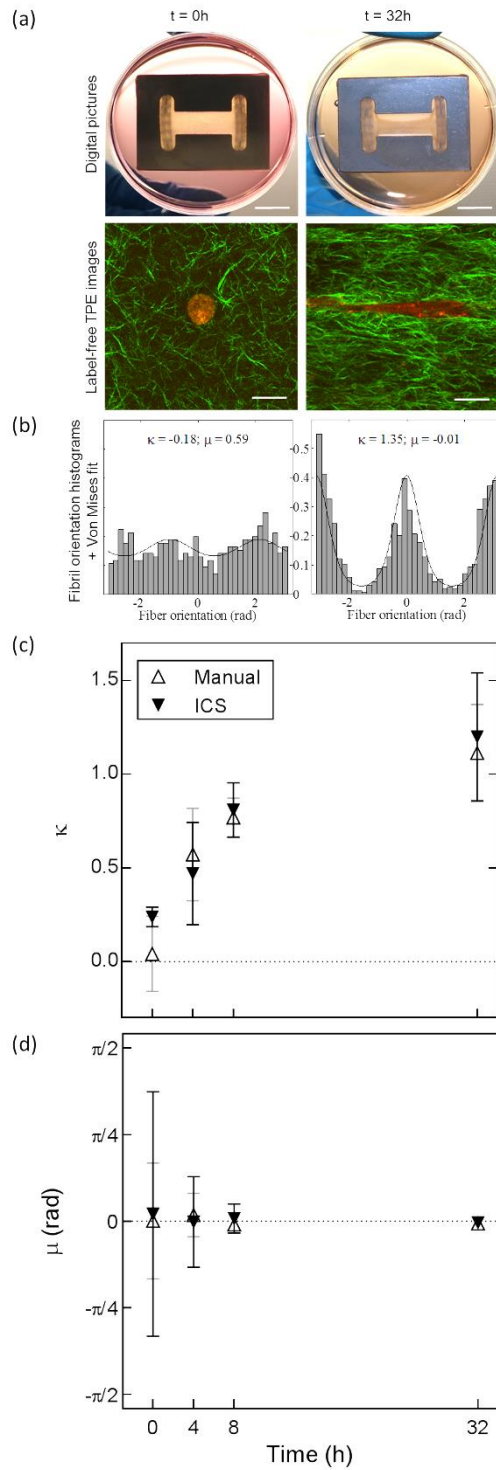
For the characterization of fibrillar hydrogels, not only collagen density but also fibril orientation are of interest, especially when developing aligned tissue engineered constructs. We recently showed that d-hDPSCs were able to self-align in a tethered collagen type I hydrogel [178], but the effect on local hydrogel architecture remained to be elucidated. Here, these constructs were monitored over time by TPE autofluorescence of the embedded cells and SHG microscopy of the collagen fibrils. Directly after casting ($t = 0$ h), cells appeared round and collagen fibrils seemed to be randomly oriented (Figure 4.2a; left). However, when the hydrogel is completely contracted ($t = 32$ h), alignment of both cells and collagen fibrils was observed parallel to the longitudinal axis of the 3D construct (Figure 4.2a; right).

As this is the first time that the Von Mises distribution has been included in an ICS based approach, we first determined the validity of the method to quantify the degree of fibril alignment. Using a set of SHG images from an aligning hydrogel, orientation parameters obtained by automated analysis and manual tracing were compared. Representative manually determined fibril orientation histograms with fitted Von Mises function at 0 h and 32 h after hydrogel casting are shown in Figure 4.2b. Both analysis methods yielded essentially equal values in terms of

the preferential angle μ and the spread of angle distribution κ (Figure 4.2 c-d). Being inversely proportional to four times the variance of the approximated wrapped Gaussian distribution, a κ value near zero is indicative of a large spread of angle distribution for the collagen type I fibrils while increasing κ values point to a narrow distribution around a preferential direction of fibril orientation. The increasing value of κ over time (Figure 4.2c) indicates that the organization of collagen type I fibrils in the tethered hydrogel changes from random directly after gel formation to highly aligned after contraction. As at $t = 0$ h the fibrils are expected to be in random orientation [136], the average value of μ is about zero with a substantial spread over the separate determinations (Figure 4.2d). The time evolution of κ and μ indicate that the collagen fibrils orient along the x-axis of the mould with a distribution with decreasing width under the action of the embedded cells.

Figure 4.2 (next page): Validation of ICS analysis of SHG images to quantify fibril orientation. **(a)** Each tethered collagen type I hydrogel seeded with d-hDPSCs was monitored from directly after hydrogel casting ($t = 0$ h) to the fully contracted stage ($t = 32$ h). Digital pictures (scale bars = 10 mm) show the macroscopic changes in hydrogel area while label-free TPE images (scale bars = 20 μm) visualize the cells (red) and collagen type I fibrils (green) by TPE autofluorescence and SHG signals respectively. **(b)** Representative manually determined fibril orientation histograms with fitted Von Mises function at 0 h and 32 h after hydrogel casting. At 4 different time points, **(c)** the spread of fibril orientation κ and **(d)** the preferential angle μ were calculated by manual and ICS analysis of SHG images with a pixel size of 85 nm and 1024 x 1024 pixels per image (yielding a field of view of 87 μm x 87 μm). Data represent means \pm SEM ($n = 3$). The error bars are sometimes smaller than the symbol.

Label-free mapping of microstructural organization in cellular hydrogels using ICS

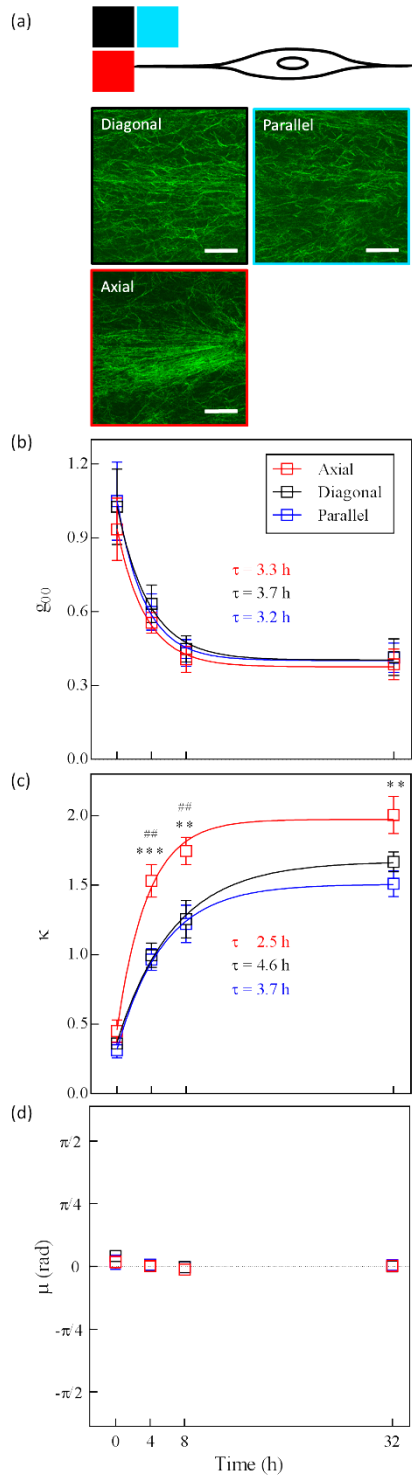


4.4.3 Local changes in hydrogel architecture during cell-mediated alignment

As described above, an overall time-dependent increase in fibril organization was observed for tethered hydrogels (Figure 4.2). However, since this collagen remodeling is cell-mediated, local differences in hydrogel architecture can be expected. To explore this hypothesis, three different zones near cells were imaged: axial, diagonal and parallel with respect to the leading edge (Figure 4.3a; red, black and blue square respectively). Figure 4.3b shows an exponential fit with a characteristic relaxation time τ for the ACF amplitude g_{00} as a function of time. For each of the above mentioned zones, the ACF amplitude decreases over time, indicating an increase in collagen density. A characteristic time of ~ 3.4 h is obtained for all zones, reaching the maximum collagen density 8 h after hydrogel casting (Figure 4.3b).

The spread of the fibril orientation decreases over time as indicated by an increasing κ (Figure 4.3c). Directly after casting ($t = 0$ h), the low κ values of ~ 0.4 for the three zones reflect an isotropic environment, thereby making the mean fibril direction μ at this time point meaningless (Figure 4.3c-d). As time progresses, zones axial to the leading edge have significantly higher κ values compared to diagonal ($t = 4-8$ h) and parallel ($t = 4-8-32$ h) zones. In addition, the characteristic times of κ reveal that axial hydrogel zones tend to align ~ 1.5 times and ~ 1.8 times faster compared to diagonal and parallel zones respectively. In this situation, Figure 3d demonstrates that the preferential direction of fibril orientation is along the x-axis of the construct (0 rad) for all zones considered.

Figure 4.3: Detection of local changes in cell-mediated hydrogel alignment by ICS analysis. (a) Schematic representation of the different zones near cellular processes in a tethered hydrogel, further referred to as axial (red), diagonal (black) and parallel (blue) zones. Per zone, a representative SHG image at 4 h after hydrogel casting is depicted. Panels (b-d) respectively show the ACF amplitude g_{00} , spread on fibril orientation κ and preferential angle μ over time for each of the zones obtained by ICS analysis of SHG images with a pixel size of 85 nm and 1024 x 1024 pixels per image (yielding a field of view of 87 μm x 87 μm). Data represent means \pm SEM ($n = 4$). ** and # # $p < 0.01$, *** and # # # $p < 0.001$ for the axial zone compared to the diagonal (#) or parallel (*) zone at that time point. The error bars for panel (d) are smaller than the symbol.



4.5 Discussion

The success of tissue engineering is often dependent on the similarity of the 3D construct and the native ECM. So, in order to develop biologically active scaffolds for regenerative medicine purposes, their microstructural organisation must be thoroughly studied during the design process and before implantation, preferentially by using non-invasive imaging and robust automated analysis methods. In this study, we extended our previously developed ICS-based model [136] to get the orientation distribution of fibrils within images obtained by SHG microscopy. The power of this model is shown in two relevant applications where we quantify the spatial and structural characteristics of collagen type I fibrils within different cellular hydrogel systems over time.

Cell-mediated contraction of free-floating collagen type I hydrogels has been well described in literature. Being dependent on the collagen concentration, the number of cells and the cell type, *in vitro* collagen contraction assays are amongst others extensively performed in tissue engineering research to optimize the composition of newly developed 3D constructs [216, 217]. Although hydrogel size and opacity are currently the most conventional readout parameters of this assay, relevant microstructural information cannot be captured in this way. The current work shows that ICS analysis of SHG images can overcome this limitation with high accuracy and without interfering in the contraction process as the method is optical and label-free. As expected, hydrogel contraction by hDPSCs or d-hDPSCs resulted in a decrease in hydrogel area. This surface reduction was accompanied by a measurable increase in collagen density as shown by declining g_{00} values. It must be noted, however, that during the first 2 hours of hydrogel contraction by hDPSCs, the central collagen density remained unchanged despite a reduction in hydrogel area. Since hydrogel compaction has been described to propagate from the edges of the hydrogel into the bulk [218], we investigated whether contraction of our free-floating hydrogels also occurred in a non-uniform manner. Indeed, when measuring the ACF amplitude in the centre and the edge of hydrogels at different time points, collagen condensation at the edge of the hydrogel started immediately after casting and reached its maximal density after 2 hours. This boundary effect explains why the initial area of hDPSC-seeded hydrogels decreases without a reduction in the central collagen density. Another observation

was that both cell types showed stepwise changes in collagen density and a gradual reduction in hydrogel area. At certain time points, however, significant smaller hydrogel areas and g_{00} values were detected for hydrogels seeded with d-hDPSCs compared to hDPSCs. So despite the similar patterns for hydrogel contraction, d-hDPSCs were more efficient in contracting collagen type I hydrogels. It must be noted that the collagen density was significantly higher for d-hDPSCs already after 2 hours, while a significant difference in hydrogel area was only observed after 4 hours, pointing to a time lag between locally initiated hydrogel remodeling and the macroscopic effect. In the course of time, both cell types reach a final collagen density that is about three times higher than the initial density, which is of the same order as the decrease in hydrogel area observed macroscopically.

In addition to change in fibril density, cell and matrix alignment is an important feature that needs to be monitored and understood for effective construction of anisotropic tissue constructs. The two-dimensional discrete Fourier transform has been shown to be effective in quantifying the degree of collagen fibril organisation in different biological tissues [219-221]. In this work, we present an alternative by extending our previously described ICS model [136], that provided a measure for the collagen fibril density, with the Von Mises distribution yielding the non-phenomenological parameter κ which represents the spread of fibril orientation. By comparison with manually obtained data, we showed the validity of this adapted ICS model for the determination of the orientation parameters μ and κ . Both the Fourier based approach and the ICS approach hold the same constraints regarding the size of the analyzed FOV, which was already discussed before for the ICS case. Yet, the preferred FOV size also depends on whether local or more global information is desired. Similarly to the Fourier based approach [221], the ICS technique can also be used to map local fibril orientation by subdividing the full FOV into smaller regions of interest (ROIs). For this type of application, the main orientation μ returned by the ICS approach is more valuable than the orientation spread κ for each ROI. When interested in the non-random fibril orientation distribution, also both the Fourier and the ICS approach can be applied. In the Fourier approach, increasing anisotropy yields more elongated frequency spectra. The degree of anisotropy can then be quantified by measuring this elongation, for instance through fitting with an ellipse and comparing the major

and minor axis lengths [221]. For the discussed ICS based approach, it was shown that the orientation spread is well quantified by κ which is related to the standard deviation of a Gaussian distribution of possible fibril orientations. The Fourier and ICS method can thus be used to both map fibril orientation and quantify the corresponding orientation distribution function.

Compared to the Fourier approach in which the spectrum is analyzed by fitting it with an ellipse [221], the ICS approach is typically slower since it is more computationally intensive in the ACF analysis step. Yet, the ICS model was specifically designed to analyze images containing fibrils, and the resulting fit parameters are directly related to physical quantities of those fibrils. Also, it was previously shown that all fibrils are taken into account when considering the ACF [136], rendering the ICS method an appropriate statistical tool to quantify the global fibril organisation, which was the goal of this work. Additionally, the model includes the SHG related polarization effect which is typically present when imaging with linearly polarized light. This phenomenon might induce artifacts in the frequency spectrum which are not accounted for in Fourier based approaches. Finally, it must be noted that the proposed ICS model is not limited to label-free SHG images only. A similar approach can also be applied to fluorescent images in case of fluorescence sensitivity to polarization, or when omitting the polarization effect in the ICS model also regular fluorescence images can be analyzed.

Throughout the central part of the tethered hydrogels, an overall time-dependent increase in fibril organisation along their longitudinal axis was observed. However, cell-induced ECM remodeling and compaction have been shown to give rise to local heterogeneities [218, 222, 223]. To capture such non-uniformities within the collagenous matrix, we specified three arbitrary zones near cellular processes that could be differentially affected in terms of hydrogel remodeling. As these predefined zones are in the direct vicinity of the cell membrane, the first anchoring events could already induce changes in hydrogel architecture, thereby explaining the slightly higher offset values of κ in these zones as compared to those of random locations in the validation experiment. According to our expectations, we observed that the rate at which the spread of fibril orientation decreased was higher in the axial zones compared to diagonal and parallel zones. In other words; the fibrils that are positioned directly in front of the leading edge of the cell exhibited faster alignment than those in adjacent areas. Also note that for the

diagonal and parallel zones, the characteristic times of κ were larger than those of g_{00} , indicating that hydrogel remodeling for these regions was still ongoing while the maximum density had already been reached. Quantitative maps of collagen density, fibril orientation and the degree of alignment around individual cells are required to capture compositional heterogeneities of collagen architecture. Since not only single cells but also intercellular forces play a role in matrix remodeling [222], such contour maps can provide insight into the formation of aligned cellular collagen type I hydrogels and can be used to optimize cellular density of tissue engineered constructs.

In the present study, we have characterized 3D cell-laden hydrogel scaffolds using an ICS model based on SHG images. Being able to capture minor temporal and spatial changes in hydrogel density and collagen fibril orientation in biologically relevant systems, we showed the sensitivity of this technique to deconstruct a complex environment. Looking beyond bulk hydrogel composition is key in understanding the mechanisms that influence the mechanical and biological properties of artificial tissues. Therefore, we believe that this ICS method has high-throughput potential in screening arrays of hydrogel scaffolds, making it an interesting tool for future tissue engineering research.

4.6 Supplementary figure

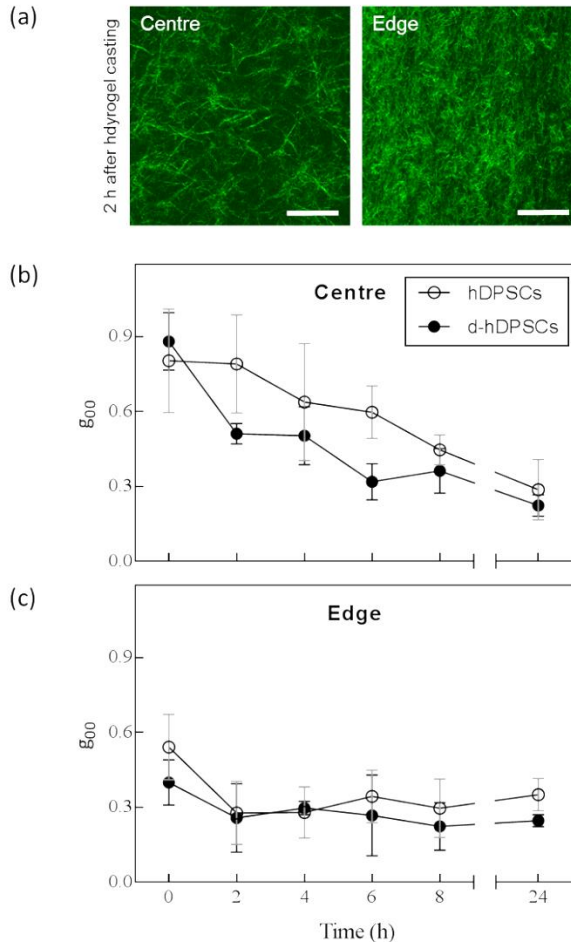


Figure 4.4: Centre versus edge microstructural changes during hydrogel contraction. Each free-floating collagen type I hydrogel seeded with (d-)hDPSCs was monitored from directly after hydrogel casting ($t = 0$ h) to the fully contracted stage ($t = 24$ h) at the centre and the edge of the hydrogel. **(a)** Representative SHG images of the centre and the edge of contracting hydrogels 2 h after casting. ICS analysis of images with a pixel size of 85 nm and 1024 x 1024 pixels per image (yielding a field of view of 87 μm x 87 μm). For both hDPSCs and d-hDPSCs, the ACF amplitude g_{00} is plotted as a function of time at the centre **(b)** and edge **(c)** of the hydrogel. Data represent means \pm standard deviation ($n = 1$, i.e. only one donor used for cellular hydrogels, but duplicate hydrogels with 3 images per hydrogel analyzed).

Chapter 5
Molecular mechanisms of collagen type I
hydrogel contraction by hDPSCs and d-hDPSCs

5.1 Abstract

Alignment of cells and the embedding matrix is a feature commonly observed within tissues such as Schwann cells and collagen type I in peripheral nerves. In order to mimic this environment, a technique was developed to non-invasively align cells and collagen fibrils in a uniaxial tethered collagen type I hydrogel. Cells within the gel attach to the matrix and self-align in parallel to the longitudinal axis in response to cell-generated tension. In order for this construct to be effective, a suitable source of Schwann cells is required. While the use of autologous Schwann cells is unfavorable due to, for example, invasive harvesting and slow expansion *in vitro*, human dental pulp stem cells (hDPSCs) provide an easily accessible and expandable cell source. In chapter 2, we described the differentiation potential of hDPSCs toward Schwann cell-like cells (d-hDPSCs) which can self-align within a collagen type I hydrogel. Furthermore, we observed distinct contraction profiles between hDPSCs and d-hDPSCs seeded in a collagen type I hydrogel, with d-hDPSCs being more potent (chapter 4). Since the collagen concentration and cell seeding density were identical, the difference in contractile capacity is most likely attributed to differential expression of collagen-binding integrin receptors in these cells. Therefore, the aim of this study was to elucidate the mechanisms by which these cells contract and interact with a collagen type I hydrogel. Protein analysis by immunocytochemistry and western blot revealed significantly higher expression of the collagen-binding receptor subunit integrin $\beta 1$ in d-hDPSCs, whereas no significant differences in the expression of integrin α subunits was observed. Furthermore, contraction was markedly impeded after antibody-based inhibition of the $\beta 1$ subunit, while no effect was observed after blocking integrin $\alpha 1$. These results indicate an important role for integrin $\beta 1$ in the contraction of a collagen type I hydrogel by both hDPSCs and d-hDPSCs. However, given the heterodimeric nature of integrin receptors, the contribution of specific integrin alpha subunits (e.g. $\alpha 11$) should be explored to reveal the differential contraction potential between both cell types. Results from our study provide initial insights in the mechanisms behind cellular self-alignment in collagen type I hydrogels. Extending this understanding of cell-matrix interactions will be of value in the development of self-aligned cellular hydrogels for neuroregenerative therapy.

5.2 Introduction

An anisotropic cellular and extracellular matrix (ECM) organization is required for proper functioning of many tissues [207]. For example, due to the specific alignment patterns of collagen type I fibrils and cells, tendons can resist loads efficiently, corneas are transparent and peripheral nerves are able to regenerate in a directed manner following injury. In this regard, the field of tissue engineering and regenerative medicine aims at developing anisotropic scaffolds that mimic the native environment. Phillips *et al.* described a technique that resulted in the self-alignment of Schwann cells seeded within a tethered collagen type I hydrogel [172]. Fabrication of this engineered neural tissue (EngNT) exploits the natural ability of contractile cells to form aligned 3D structures in response to cell-generated tension.

The intimate coupling of cells and their ECM is mediated by integrins. Integrins are transmembrane glycoproteins that consist of one α and one β subunit forming a heterodimer. At least 24 different heterodimers have been identified in mammals, each of which can bind to a specific set of ligands [113]. The primary collagen receptors are represented by integrin $\alpha1\beta1$, $\alpha2\beta1$, $\alpha10\beta1$ and $\alpha11\beta1$ [224, 225]. Although Schwann cells have been shown to express the $\alpha1\beta1$ and $\alpha2\beta1$ receptors, other ECM proteins such as laminin and fibronectin are far more efficient in promoting adhesion and migration of Schwann cells compared to collagen substrates [226]. Therefore, we speculate that Schwann cells seeded in a collagen type I hydrogel might not properly or efficiently remodel their ECM to create EngNT. In order to obtain nicely self-aligned cellular hydrogels, the interaction of the seeded cells and their ECM must be optimal. Since pure laminin and fibrinectin hydrogels are not commercially available up until now, and collagen type I is the main ECM protein in het peripheral nervous system [1], the use of collagen type I hydrogels to generate EngNT is set. Hence, an alternative cell source of Schwann cells is required.

Recently, we have shown that human dental pulp stem cells (hDPSCs) can differentiate toward Schwann-like cells (d-hDPSCs) [178]. In addition to secreting a range of neurotrophic factors and promoting neuronal survival, these d-hDPSCs were able to self-align within collagen type I hydrogels, thereby directing neurite outgrowth *in vitro*. As already described in chapter 4, we also observed that d-

hDPSCs were more efficient in contracting collagen type I hydrogels compared to d-hDPSCs. A number of factors can influence hydrogel contraction that can possibly explain the observed difference between hDPSCs and d-hDPSCs. These include cell count (more cells yield faster contraction), collagen type I concentration (higher density hydrogels are more difficult to contract), and cell type [227]. While cell count and collagen density were the same for every condition in our experiment, two related yet different cell types were used. It is well known that every cell type possesses a specific integrin signature, which can even reflect differentiation states of cells [114, 228]. Although a number of studies already described the expression of integrin subunits on hMSCs [229-231] as well as their interaction with a collagen type I hydrogel [232], the integrin signatures of hDPSCs and d-hDPSCs have yet to be reported. We hypothesize that the differential contractile capacity of hDPSCs and d-hDPSCs in collagen type I hydrogels can be attributed to distinct collagen-binding integrin signatures of these cells.

5.3 Materials and methods

5.3.1 Materials and products

All products were purchased from Sigma-Aldrich (Bornem, Belgium) unless mentioned otherwise.

5.3.2 Isolation, culture and differentiation of hDPSCs

Dental tissues were obtained with informed consent from donors (15-20 years of age) undergoing third molar extraction for orthodontic or therapeutic reasons at Ziekenhuis Oost-Limburg, Genk, Belgium. Written informed consent of patients younger than 18 years was obtained via their legal guardians. This study was approved by the medical ethical committee of Ziekenhuis Oost-Limburg. hDPSCs were isolated, cultured and differentiated toward Schwann-like cells (d-hDPSCs) as described in chapter 2 (section 2.3.2).

5.3.3 Collagen contraction assay

The contractile capacity of hDPSCs and d-hDPSCs within a collagen type I hydrogel was determined as described in chapter 4 (section 4.3.4). Contraction at each time point was measured as the percentage reduction of the initial hydrogel area.

5.3.4 Isolation of primary Schwann cells

Experimental procedures involving neonatal animals were approved by the medical ethical committee of Hasselt University. The isolation of primary rat Schwann cells from neonatal (P5) Sprague-Dawley rats was performed as described in chapter 2 (section 2.3.4).

5.3.5 RNA extraction and RT-PCR

To extract (d-)hDPSCs from hydrogels, replicate gels were transferred to a 6-well plate, washed with PBS and subsequently incubated with 0.2% collagenase (diluted in medium without FBS) for 1 h at 37 °C. When the gel was completely digested, the supernatant was collected and adherent cells in the 6-well plate were trypsinized, after which they were also collected. The cell suspension was then pelleted at 400 *g* for 10 min. To reduce collagen debris of the hydrogel, the resulting pellet was washed with PBS and centrifuged again and this procedure

was repeated 2 more times. Total RNA from these pellets was extracted as described by the PARIS™ Kit (Ambion, LifeTechnologies) and RNA concentrations and purity were determined with a NanoDrop 2000 Spectrophotometer (Thermo Scientific, Pittsburgh, USA). 500 ng RNA was used for reverse transcription in reaction volumes of 20 μ l using qScript™ cDNA SuperMix (Quanta Biosciences, VWR International, Leuven). cDNA was amplified through RT-PCR according to the protocol described in Table 5.1. New primer sets were developed by means of Primer-BLAST (Table 5.2). The RT-PCR products were analysed by 1.5% (w/v) agarose containing 1 μ g/ml ethidium bromide gel electrophoresis.

5.3.6 Immunocytochemistry

For immunocytochemical analysis, hDPSCs and d-hDPSCs were seeded on 12 mm glass coverslips (PLL coated for d-hDPSCs) at a concentration of 2×10^4 cells in standard culture medium or differentiation medium respectively. When cells reached 70-80% confluency, they were fixed in 4% PFA for 20 min at RT. For intracellular targets (e.g. integrin α 1), cells were permeabilized with 0.05% Triton X-100 in PBS for 30 min at 4 °C. Aspecific binding sites were blocked by incubating cells with 10% normal donkey serum (Millipore, MA, USA) in 1x PBS for 30 min at RT. After washing with 1x PBS, cells were incubated with the primary antibodies for either 1 h at RT or overnight at 4 °C. Samples in which the primary antibody was omitted were used as a blanco. Prior to adding the secondary antibody, cells were washed four times with 1x PBS. Secondary antibodies were incubated for 1 h at RT in the dark, followed by the DAPI nuclear counterstain for 10 min at RT in the dark. Primary and secondary antibodies used are listed in Table 5.3. Coverslips were mounted with Dako fluorescent mounting medium (Dako, Heverlee, Belgium) on glass slides. Samples were evaluated using a Nikon Eclipse 80i fluorescence microscope equipped with a Nikon DS-2MBWc digital camera (Nikon, Tokyo, Japan). For each staining, fluorescent images of hDPSCs were used to establish the reference settings in ImageJ (upper and lower threshold). Quantification of the fluorescent images of both hDPSCs and d-hDPSCs was performed using ImageJ. By measuring the total fluorescence intensity of each image and divide it by the number of cells in that image, the resulting mean fluorescence intensity (MFI) per cell allowed to calculate the relative difference in protein expression of d-hDPSCs compared to hDPSCs.

Table 5.1: RT-PCR protocol

Product	PCR mix		cDNA amplification		
	$\mu\text{l}/\text{sample}$		Temperature ($^{\circ}\text{C}$)	Time (min)	Cycles
MilliQ	17		50	30	1
10x PCR buffer	2.5		95	15	1
dNTPs (10 mM)	0.5		95	0.5	
Forward primer (10 μM)	1		T_m	0.5	34
Reverse primer (10 μM)	1		72	1	
Taq polymerase	1		72	2	4
cDNA	2		4	∞	1

Table 5.2: Overview of primers used for RT-PCR.

Target gene	Accession number	Primer	Sequence (5' -3')	T_m ($^{\circ}\text{C}$)	Product size (bp)
Integrin $\alpha 1$	NM_181501.1	Forward	CTCCTCACTGTTGTTCTACGCT	60	442
		Reverse	ACGACTTGAATGTGGGGCT		
Integrin $\alpha 2$	NM_002203.3	Forward	TTGGCATAGCAGTTCTTGGGT	60	302
		Reverse	GGTCCCACTCCAGCCTAAAG		
Integrin $\alpha 11$	NM_001004439.1	Forward	TCAGTGGCAATAAGTGGCTGG	60	168
		Reverse	CGAGGGCGCATGTTGTCTTC		
Integrin $\beta 1$	NM_002211.3	Forward	TGTGAATGCCAAAGCGGAAGG	60	334
		Reverse	TGCAAACACCATTTCTCCAC		
18S	NM_022551.2	Forward	TCAACTTTCGATGGTAGTCGC	60	324
		Reverse	CCTCCAATGGATCCTCGTTAA		

Table 5.3: Overview of primary and secondary antibodies used for immunocytochemistry.

Primary antibody	Species	Dilution	Manufacturer	Secondary antibody	Dilution
Integrin $\alpha 1$	Rabbit polyclonal	1/200	Abcam (ab78479)	Donkey-anti-rabbit (A488)	1/1000
Integrin $\alpha 2$	Mouse monoclonal	1/100	Abcam (ab55340)	Donkey-anti-mouse (A555)	1/1000
Integrin $\beta 1$	Mouse monoclonal	1/100	Abcam (P5D2)	Donkey-anti-mouse (A555)	1/1000

5.3.7 Western blot

In order to quantify integrin expression levels of hDPSCs and d-hDPSCs western blot analysis was performed. After washing the cells with PBS, ice-cold lysis buffer was added (1 ml per 10^7 cells). Subsequently, adherent cells were scraped of the culture flask using a plastic cell scraper and the resulting cell suspension was transferred into a pre-cooled microfuge tube. Following constant agitation for 30 min at 4 °C, the cell suspension was centrifuged for 20 min at 13,800 *g*. The supernatant was aspirated and placed in a fresh eppendorf and afterwards stored at -80 °C.

SDS-PAGE was performed according to a standard protocol. Briefly, 5 μ g of protein samples were loaded on 7.5% polyacrylamide gels, under denaturing condition (without BME). Samples were heated for 10 min at 70°C prior to loading. Electrophoresis initially was run at 100V until the samples reached the separating gel, after which the voltage was increased to 150V to complete the run. Subsequently proteins were transferred onto a PVDF membrane for 90 min at 350 mA. The membrane was incubated with blocking solution consisting of 5% bovine serum albumin (BSA) in PBS for 1 h at room temperature with gentle shaking. Afterwards the membrane was incubated with the primary antibody diluted in 2% BSA, overnight at 4° C. After washing with 0.05% PBS-Tween20, the membrane was incubated with a horseradish peroxidase (HRP) labeled secondary antibody for 1 h at room temperature. Primary and secondary antibodies used are listed in Table 5.4. The membrane was washed 3x5 min in 0.05% PBS-Tween and 30 min in MilliQ to reduce background signals. Finally, the membrane was incubated with

Pierce ECL plus western blotting substrate for 5 min at room temperature in the dark, followed by chemiluminescent detection using an Image Quant LAS 4000 mini. In general, beta-actin (mouse monoclonal; 1:5000; Santa Cruz, Heidelberg, Germany) was used for normalization in processing of the results.

Table 5.4: Overview of primary and secondary antibodies used for western blot.

Primary antibody	Species	Dilution	Manufacturer	Secondary antibody	Dilution
Integrin α 1	Rabbit polyclonal	1/1250	Abcam (ab78479)	Goat-anti-rabbit	1/5000
Integrin α 11	Rat monoclonal	1/1000	R&D Systems	Rabbit-anti-rat	1/5000
Integrin β 1	Mouse monoclonal	1/100	Abcam (P5D2)	Rabbit-anti-mouse	1/5000

5.3.8 Inhibition hydrogel contraction

In order to determine the contribution of certain collagen type I-binding integrin subunits in the contraction process of both hDPSCs and d-hDPSCs, an inhibition experiments was set up. Cell-seeded collagen hydrogels were prepared as described in chapter 4 (section 4.3.4). In this case however, cell suspensions of hDPSCs and d-hDPSCs were prepared for a number of different conditions. After removal of the supernatant, cell pellets were resuspended in medium (standard culture medium or differentiation medium) containing different concentrations of blocking antibodies (10⁻¹ – 0.1 – 0.01 μ g/ml), or their matched isotype controls at 10 μ g/ml (Table 5.5). A blanco, in which blocking antibody or isotype control was omitted, was also incorporated. Cell pellets were allowed to incubate in blocking or 'control' medium for 20 min on ice, after which the right amount of neutralized collagen suspension was added, attaining a final concentration of 10⁶ cells/ml. For each condition, 75 μ l of this cellular collagen solution was pipetted in a 96-well plate (Greiner, F-bottom) in duplo. After polymerization, 150 μ l standard or differentiation medium containing the appropriate concentration of antibody was added to the corresponding wells. The hydrogels were detached from the wells using a needle and allowed to incubate for 8 h at 37 °C. After 8 h, digital

images were taken from the hydrogels. Images were imported into ImageJ and contraction was measured as described in chapter 4 (section 4.3.3).

Table 5.5: Overview of blocking antibodies and isotype controls used for inhibition of hydrogel contraction.

Blocking antibody	Species	Manufacturer	Isotype control
Integrin α 1	Mouse monoclonal	Abcan (ab33410)	Mouse IgG2a
Integrin β 1	Mouse monoclonal	Abcam (ab24693)	Mouse IgG1

5.3.9 Statistical analysis

Statistical analysis was performed using GraphPad Prism 5 software (GraphPad, San Diego, CA, USA). Data from the hydrogel contraction profile were compared by means of a 2-way ANOVA followed by Bonferroni's multiple comparison test. Data from immunocytochemistry and western blot analysis were compared by means of a Mann-Whitney test. Data were represented as mean \pm standard error of the mean (SEM). P-values ≤ 0.05 were considered statistically significant.

5.4 Results

5.4.1 Differential contraction of collagen type I hydrogels by hDPSCs and d-hDPSCs

The collagen contraction assay data for hDPSCs and d-hDPSCs described in chapter 4 (section 4.1.1) are represented here differently in order to facilitate the interpretation of involved molecular mechanisms. Briefly, the ability of hDPSCs and d-hDPSCs to contract a collagen type I hydrogel was measured as a percentage of the reduction in hydrogel area (Figure 5.1). Although both cell types showed similar contraction after 2 h (~20% area decrease), d-hDPSCs attained significantly higher contraction levels at 4 h and 6 h after hydrogel casting compared to hDPSCs. After 24 h, the hydrogel area was reduced by approximately 60% by both hDPSCs and d-hDPSCs.

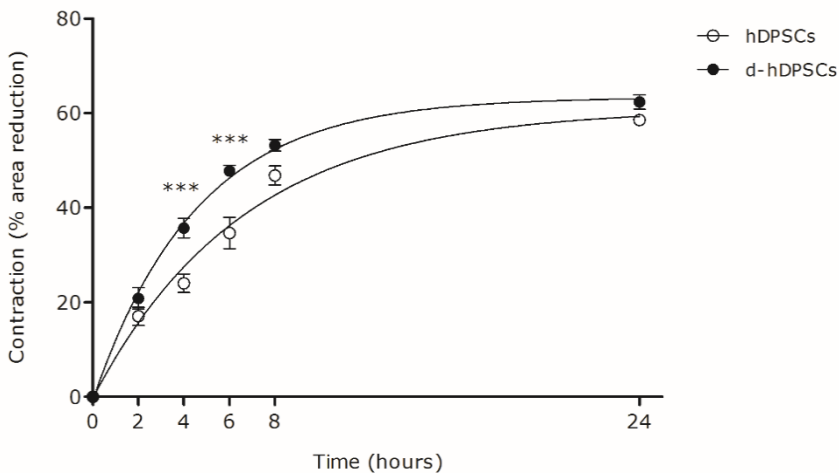


Figure 5.1. Hydrogel contraction profile for hDPSCs and d-hDPSCs. The contractile capacity of hDPSCs and d-hDPSCs in collagen type I hydrogels was assessed over time, with 0 h being immediately after hydrogel casting. Contraction at each time point was measured as the percentage reduction of the initial hydrogel area. Data represent means \pm SEM ($n = 4$). *** $P < 0.001$ compared with hDPSCs at that time point. Adapted from Figure 4.1b.

5.4.2 Expression of integrins by hDPSCs and d-hDPSCs at mRNA level

The observed distinction in contractile ability between hDPSCs and d-hDPSCs could be due to a differential expression of certain collagen type I binding integrins. Based on previous research conducted in human MSCs regarding the expression of collagen type I binding integrins [225, 230, 232, 233], the following integrin receptors were selected as the focus of our research: $\alpha 1\beta 1$, $\alpha 2\beta 1$ and $\alpha 11\beta 1$. Consequently, hDPSCs and d-hDPSCs were screened in the first place for the mRNA expression levels of the integrin subunits $\alpha 1$, $\alpha 2$, $\alpha 11$ and $\beta 1$ by means of RT-PCR (Figure 5.2). Analyses indicated overall comparable expression levels of the aforementioned subunits between hDPSCs and between different donors, although integrin $\alpha 11$ and $\beta 1$ mRNA from donor 2 d-hDPSCs were detected at different molecular weights compared to the other samples.

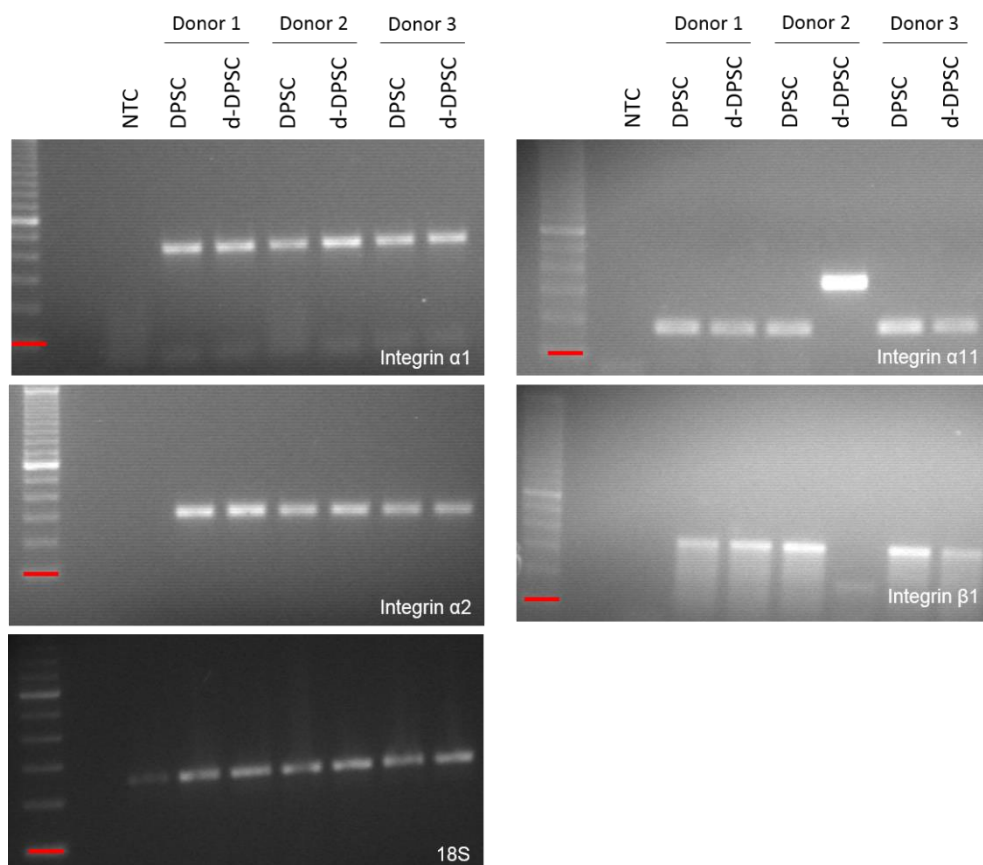


Figure 5.2: Expression of integrins by hDPSCs and d-hDPSCs at mRNA level. RT-PCR was conducted to measure the expression levels of the integrin subunits $\alpha 1$, $\alpha 2$, $\alpha 11$ and $\beta 1$ by hDPSCs and d-hDPSCs. The 18S ribosomal RNA was used as a reference gene. Red lines indicate the 100bp DNA fragments from the ladder.

5.4.3 Expression of integrins by hDPSCs and d-hDPSCs at protein level

The protein expression of integrin subunits $\alpha 1$, $\alpha 2$ and $\beta 1$ by hDPSCs and d-hDPSCs was assessed via immunocytochemistry. Whereas integrin $\alpha 1$ and $\beta 1$ were found to be abundantly expressed by both cell types (Figure 5.3a, b, e, f), the integrin $\alpha 2$ subunit was undetectable in hDPSCs and d-hDPSCs (Figure 5.3c, d). Furthermore, the staining for the $\alpha 1$ and $\beta 1$ subunits revealed the presence of focal adhesions, which are clustered integrin receptors at the cell membrane, in both hDPSCs and d-hDPSCs (Figure 5. 3a, b, e, f; arrows). In order to determine potential differences in protein expression levels of integrin $\alpha 1$ and $\beta 1$, quantitative analysis of the fluorescent images of hDPSCs and d-hDPSCs was performed (Figure 5.3g, h). While the expression of integrin $\alpha 1$ was not significantly altered in d-hDPSCs, the integrin $\beta 1$ subunit was expressed about 2.4-fold higher in d-hDPSCs compared to hDPSCs.

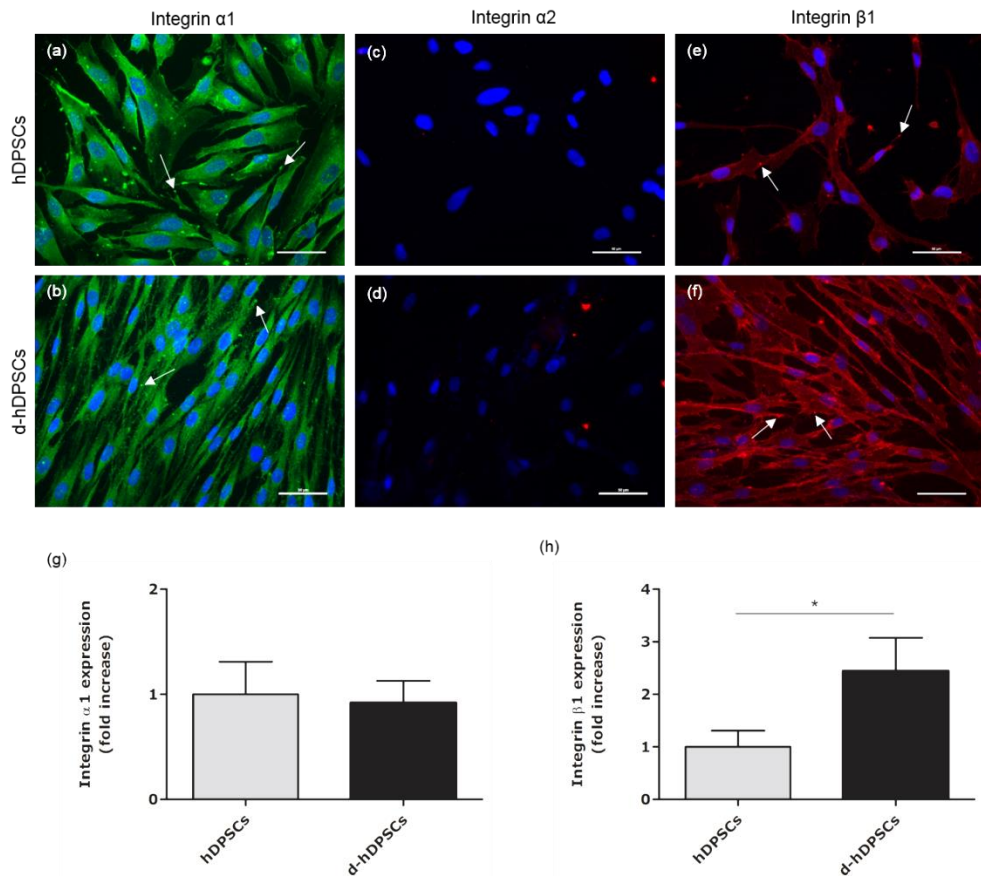


Figure 5.3: Expression of collagen type I binding integrins $\alpha 1$, $\alpha 2$ and $\beta 1$ in hDPSCs and d-hDPSCs. Immunocytochemistry was performed on hDPSCs (a, c, e) and d-hDPSCs (b, d, f) for the collagen type I binding integrin subunits $\alpha 1$, $\alpha 2$ and $\beta 1$. Nuclei were counterstained with DAPI (blue). Arrows indicate focal adhesion points. Protein expression levels were quantified for integrin $\alpha 1$ (g; $n = 4$) and $\beta 1$ (h; $n = 5$) and are represented as relative fold increase compared to the expression level in hDPSCs. Scale bars = 50 μm . Data represent means \pm SEM. * $P < 0.05$.

The expression of collagen type I binding integrin subunits in hDPSCs and d-hDPSCs was further investigated through western blot (Figure 5.4). Similar to the results obtained by immunocytochemistry, a strong integrin $\beta 1$ expression could be detected in both cell types. Integrin $\alpha 1$ however produced a less pronounced signal. Furthermore, the integrin $\alpha 11$ subunit displayed an apparent band in

undifferentiated and Schwann cell differentiated hDPSCs (Figure 5.4a). In order to quantify protein levels of the integrin subunits in hDPSCs and d-hDPSCs, their expression levels were normalized to those of β -actin (Figure 5.4b-d). In line with the results obtained from immunocytochemical stainings, expression of the integrin β 1 subunit was significantly increased in d-hDPSCs (approximately 5-fold) compared to hDPSCs. The expression of integrin α 1 and α 11 was slightly increased in d-hDPSCs (\sim 1.3-fold and \sim 1.9-fold respectively), although not significant.

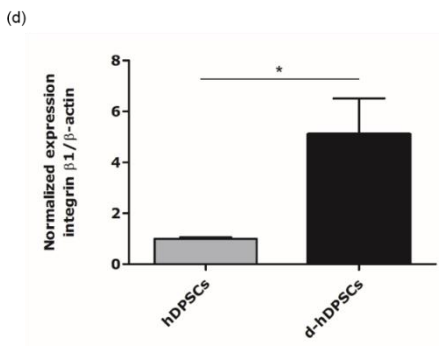
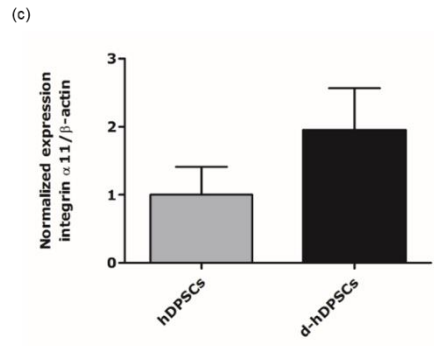
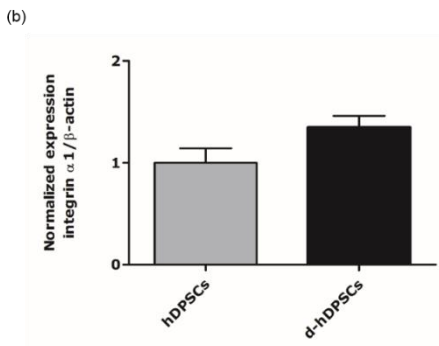
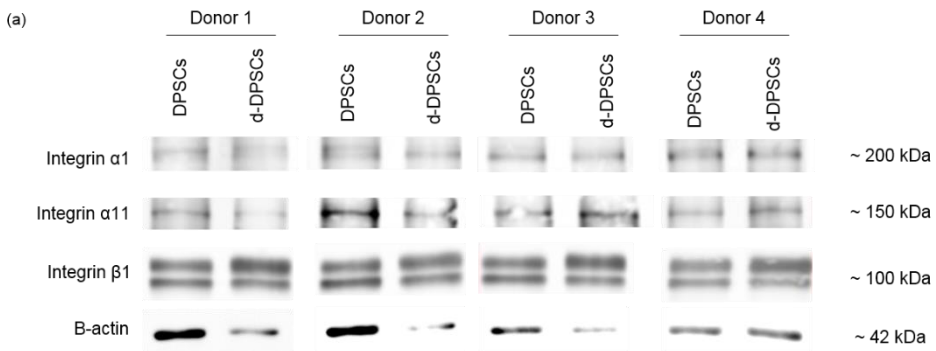


Figure 5.4: Differential expression of the collagen type I binding integrin subunits $\alpha 1$, $\alpha 11$ and $\beta 1$ after differentiation. (a) Western blot analysis was performed to investigate protein expression levels between hDPSCs and d-hDPSCs for four different donors ($n = 4$). Consequent quantification was carried out to determine the protein expression levels of integrin $\alpha 1$, $\alpha 11$ and $\beta 1$ in d-hDPSCs, compared to hDPSCs (b-d). Values were normalized against beta-actin and are represented as relative fold changes. Data represent means \pm SEM. * $P < 0.05$.

5.4.4 Integrin $\beta 1$ plays a major role in the contraction process of hDPSCs and d-hDPSCs in a collagen type I hydrogel

Previous experiments have shown that d-hDPSCs possess a larger contractile ability within a collagen type I hydrogel compared to hDPSCs. Furthermore, immunocytochemical and western blot analysis revealed a considerably increased expression of the collagen type I binding integrin $\beta 1$ subunit (and to a lesser extent of integrin $\alpha 1$ and $\alpha 11$) in d-hDPSCs. To investigate the contribution of specific integrin subunits in the contraction of collagen type I hydrogels by hDPSCs and d-hDPSCs, an inhibition experiment using blocking antibodies was performed. For each experiment, cells were pre-incubated with four different concentrations (10 – 1 – 0.1 – 0.01 $\mu\text{g/ml}$) of the respective blocking antibody or an isotype antibody (negative control). At 8 h after hydrogel casting, contraction was captured and measured as the percentage reduction of the initial hydrogel area. Integrin $\alpha 1$ inhibition had no effect at any concentration on the contraction capacity of hDPSCs and d-hDPSCs in a collagen type I hydrogel (Figure 5.5a). In contrast, blocking of the integrin $\beta 1$ subunit at the two highest concentrations markedly reduced hydrogel contraction by both hDPSCs and d-hDPSCs. At lower concentrations ($<0.1 \mu\text{g/ml}$), contraction reached percentages comparable to those of the blanco (normal situation; no blocking antibody or isotype control) and the negative control (Figure 5.5b).

Collagen type I hydrogel contraction by hDPSCs and d-hDPSCs

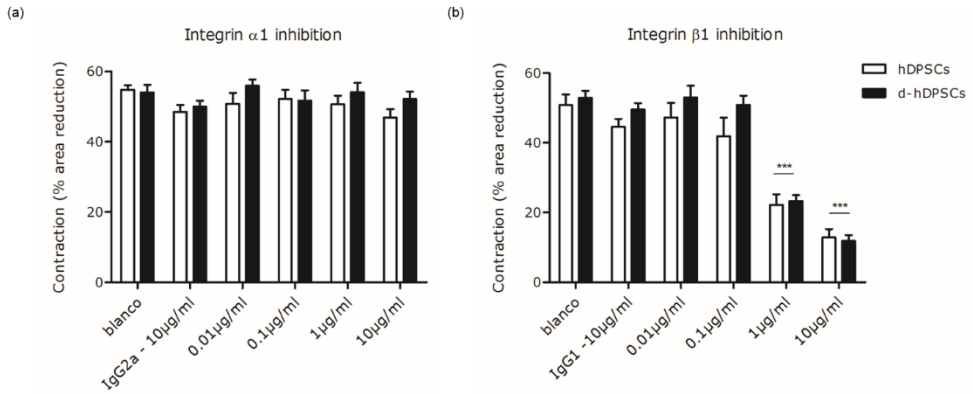


Figure 5.5: Effect of integrin $\alpha 1$ or $\beta 1$ inhibition on hydrogel contraction by hDPSCs and d-hDPSCs. hDPSCs and d-hDPSCs were pre-incubated with blocking antibodies against integrin $\alpha 1$ (a) or $\beta 1$ (b) at 4 different concentrations (0.01 – 0.1 – 1 – 10 μ g/ml) or their respective isotype controls at 10 μ g/ml before seeding in a collagen type I hydrogel. Samples without antibodies were used as blanco. After 8 h, hydrogel contraction was measured as the percentage reduction of the initial hydrogel area. Data represent means \pm SEM ($n = 4$). *** $p < 0.001$ compared with the IgG1 isotype control condition for the according cell type.

5.5 Discussion

In the present study, we investigated the mechanisms by which hDPSCs and d-hDPSCs contract and interact with a collagen type I hydrogel. A number of studies already described the expression of integrin subunits on human MSCs [229-231] as well as their interaction with a collagen type I hydrogel [232]. However, our study is the first in which the expression of collagen type I-binding integrin receptor subunits in hDPSCs and d-hDPSCs and their role in contraction of collagen type I hydrogels have been explored.

First, we determined the collagen hydrogel contraction profile of hDPSCs and d-hDPSCs. Although both cell types were able to reduce the initial hydrogel volume by approximately 60%, the time course of the contraction process was different for hDPSCs and d-hDPSCs with d-hDPSCs being more efficient. Since the number of seeded cells and the collagen concentration was identical for both cell types, the aforementioned difference in contractile ability is most likely to be attributed to differential expression of collagen-binding integrin receptors between hDPSCs and d-hDPSCs. In general, four integrin heterodimers are functioning as collagen receptors, namely $\alpha1\beta1$, $\alpha2\beta1$, $\alpha10\beta1$, and $\alpha11\beta1$. Since the integrin signature of hDPSCs and d-hDPSCs has not been studied so far, we built on previous research performed in human MSCs regarding the expression of collagen binding integrins [230, 232-234] in this first exploration. In that regard, the following integrin subunits were selected for further investigation in hDPSCs and d-hDPSCs: $\alpha1$, $\alpha2$, $\alpha11$ and $\beta1$.

At the mRNA level, no differences were observed in the expression of integrin $\alpha1$ and $\alpha2$. Although for d-hDPSCs from donor 2, the mRNA of $\alpha11$ and $\beta1$ integrin subunits was detected at unexpected molecular weights, this disparity was not detected by western blot analysis (donor 4), indicating normal protein formation. Interestingly, the protein level of integrin $\beta1$ was significantly upregulated in d-hDPSCs compared to hDPSCs as confirmed through both immunocytochemistry and western blot analysis. It is important to notice that integrins are heterodimeric receptors and require both subunits in order to be functionally active and participate in bi-directional signaling pathways. Many processes like cell motility, proliferation, morphology and differentiation are dependent on this continuous dialog between the exterior and interior of the cell [114, 225]. Since free α and β

subunits do not exist at the cell surface and the amount of functionally active integrin receptors present on the cell surface is determined by the amount of α -subunits available [114, 233], the difference in contractile ability cannot be explained by an increase in β 1 protein levels alone.

No change in expression at the mRNA and protein level was observed for the integrin α 1 subunit in hDPSCs before and after differentiation. Interestingly, a study performed by Rider *et al.* [235] reported that a human MSC subpopulation sorted for increased expression of integrin α 1 displayed enhanced plasticity. This could suggest that the upregulation of integrin α 1 is important for maintaining MSC, and thus possibly also for hDPSCs, stemness rather than differentiation.

In order to further corroborate the contribution of the integrin subunits α 1 and β 1 in the contraction process of a collagen type I hydrogel, an inhibition experiment was set up. The respective subunits were blocked using specific antibodies in 4 different concentrations. Following pre-incubation in the blocking antibody, hDPSCs and d-hDPSCs were allowed to contract within a collagen type I hydrogel and 8 h later contraction was measured. Blocking of the β 1 subunit considerably reduced contraction at the highest concentration of the blocking antibody in both hDPSCs and d-hDPSCs. As could be expected, integrin β 1 plays a major role in the contraction process due to the fact that every collagen-binding receptor incorporates a β 1 subunit. On the other hand, blocking of the integrin α 1 subunit had no effect whatsoever, not even at highest concentrations. This could be explained by the presence of functional redundancy between the α -subunits of collagen type I binding integrins. A mechanism of compensatory cross-talk between the collagen type I binding integrins in hMSCs has been described previously [233]. It was observed that the loss of the integrin α 1 subunit led to an increased expression of integrin α 2 and α 11 (as a compensatory mechanism), and loss of integrin α 2 stimulated the expression of integrin subunits α 1 and α 11. Furthermore, knockdown of integrin α 11 led to a slight increase only in integrin α 1, which resulted in impaired adhesion of hMSCs to collagen type I as there hardly was any compensation of other collagen type I binding integrins [233]. In our study, western blot analysis revealed a near 2-fold increase in α 11 expression in d-hDPSCs. Although not significant, integrin α 11 (forming a heterodimer with β 1) seems to be the most likely candidate to explain the difference in contraction between hDPSCs and d-hDPSCs. This careful notion is further supported by a

study in which Popova *et al.* [236] reported that integrin $\alpha 11$ deficiency in mice resulted in disorganized periodontal ligament formation and tooth-dependent dwarfism. Periodontal ligament is highly enriched with collagen type I and it appears that integrin $\alpha 11\beta 1$ is the only collagen receptor expressed. Based on these results, it would be interesting to investigate the contraction potential of hDPSCs and d-hDPSCs after antibody-based blocking of the integrin $\alpha 11$ subunit and whether or not compensation of other collagen-binding integrin subunits occurs.

With regard to measuring protein expression levels of integrin subunits in hDPSCs and d-hDPSCs by western blot analysis, future experiments should be optimized in two ways. First, the use of β -actin as a loading control should be avoided since noticeable differences in the β -actin signal intensity between hDPSCs and d-hDPSCs were observed. β -actin is a cytoskeletal protein, involved in cell motility, structure and contraction. As such, it is possible that the expression of the β -actin protein is altered after Schwann cell differentiation, potentially through integrin-mediated signaling pathways since members of the Rho family of GTPases have emerged as key regulators of the actin cytoskeleton, coordinated by integrin signaling [225]. So in retrospect, it would have been better to use a non-cytoskeletal related loading control such as GAPDH. Second, instead of looking at whole cell integrin expression levels, it would be more interesting to prepare cytoplasmic and membrane-bound protein fractions as this will allow discrimination between active integrin subunits on the cell surface and the intracellular pool of integrin-loaded vesicles.

In the present study, d-hDPSCs have shown to possess a larger contractile potential within a collagen type I hydrogel, compared to hDPSCs. These results were accompanied by a higher expression of the integrin $\beta 1$ subunit in hDPSCs as confirmed through both immunocytochemistry and western blot analysis. The importance of $\beta 1$ in the contraction process was confirmed through inhibition experiments. However, given the heterodimeric nature of integrin receptors, the contribution of specific integrin α subunits should be explored to reveal the precise molecular mechanism of differential contraction between hDPSCs and d-hDPSCs. These results are of high value in the development of self-aligned cellular hydrogels as a neuroregenerative therapy. Understanding the mechanisms that

control the behavior of cells in their 3D environment is of great value for successfully creating cellular self-aligned scaffolds such as EngNT.

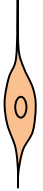
Chapter 6

General discussion and outlook

Tissue engineering is a multidisciplinary field that incorporates biology, engineering and clinical science in order to repair and/or regenerate body structures. The two building blocks of regenerative medicine are cells and scaffolds, which must be carefully selected in order to meet the requirements for specific tissue types. An ideal scaffold should be biocompatible and mimic the native architecture of the host tissue in terms of physical and mechanical properties. For the treatment of PNI, many researchers have aimed to recreate the bands of Büngner which provide trophic and guidance cues in the form of aligned Schwann cells and collagen type I fibrils. The disadvantages accompanied with the isolation and expansion of autologous Schwann cells sparked the search for alternative cell sources. One of the most important medical breakthroughs of the 20th century was the discovery of stem cells. Given their remarkable ability to self-renew and differentiate into multiple cell types, numerous studies have focused on the application of stem cells in tissue engineering approaches. Although a variety of stem cell populations have been postulated to promote nerve regeneration, hDPSCs have gained significant interest in the field of neural tissue engineering over the past decade. The more the transplanted cells resemble and behave as the host cells, the more effective and efficient the damaged tissue can be regenerated. Therefore, generation of Schwann cells from hDPSCs could significantly enhance peripheral nerve regeneration upon transplantation.

In this dissertation, we aimed to differentiate hDPSCs toward Schwann cells and assess their general characteristics and their neuroregenerative potential. First of all, we investigated the *in vitro* glial differentiation capacity of hDPSCs at the morphological, cytochemical and ultrastructural level and the neuroprotective, neurotrophic and angiogenic effects of hDPSCs and d-hDPSCs in 2D *in vitro* culture models. Table 6.1 summarizes these results and shows a comparison with the preferred Schwann cell phenotype, namely repair Schwann cells. Next, a 3D collagen type I hydrogel system was used to study the potency of d-hDPSCs to self-align and guide regrowing neurites *in vitro* and we examined the multifaceted neuroregenerative activities of d-hDPSCs in a rat sciatic nerve model (main results are summarized in Table 6.2), which is a well-established and widely used experimental procedure for the study of recovery from PNI. Finally, in order to gain more insight in the process of EngNT formation, the microstructural changes

Table 6.1. *In vitro* morphological, ultrastructural, cytochemical and functional properties of hDPSCs and d-hDPSCs compared to repair Schwann cells. *Most information on repair Schwann cells comes from *in vivo* studies.

	 hDPSCs	 d-hDPSCs	 Repair Schwann cells*
Morphology	Fibroblast-like	Spindle-shaped bipolar	Elongated bipolar
Ultrastructural properties	Euchromatic nuclei with prominent nucleoli, perinuclear organelles	Organelles throughout cytoplasm, cell-cell contacts	no <i>in vitro</i> data available
Marker expression			
Laminin	-	+	+++
p75NTR	-	+	+++
GFAP	-	+	+++
CD104	-	+	+++
Nestin	++	+	-
BDNF	+	+++	+++
GDNF	+	+++	+++
b-NGF	+	+++	+++
NT-3	+	++	+++
VEGF	+	++	+++
Integrin α 1	+	+	No <i>in vitro</i> data available
Integrin α 2	-	-	No <i>in vitro</i> data available
Integrin α 11	+	+	No <i>in vitro</i> data available
Integrin β 1	+	++	+++
Functional properties <i>in vitro</i>			
Neuronal survival	+	+++	+++
Neurite length	+	+++	+++
Endothelial cell proliferation	+	+	No <i>in vitro</i> data available
Endothelial cell migration	+	+	No <i>in vitro</i> data available
Endothelial tube formation	+	+	No <i>in vitro</i> data available
Collagen type I hydrogel contraction	+	+++	No <i>in vitro</i> data available

in the fibrillary hydrogel architecture were mapped in a label-free manner using a robust analysis model and we performed several test to reveal the molecular mechanisms responsible for collagen type I hydrogel contraction by hDPSCs and d-hDPSCs. In the following paragraphs, the most important results of this thesis are summarized and discussed.

Can hDPSCs differentiate toward Schwann cells *in vitro*?

Since the first successful differentiation of MSCs into functional Schwann cells [155], numerous studies have described the generation of Schwann-like cells from distinct MSC sources such as bone marrow [155, 237-242], adipose tissue [163, 243, 244] and umbilical cord [245-247]. DPSCs represent an MSC-like population derived from migrating neural crest cells. They share their developmental origin with Schwann cells and already express markers associated with neural phenotypes in an undifferentiated state. Accordingly, DPSCs could possess a predisposition for Schwann cell differentiation.

We investigated the *in vitro* differentiation potential of hDPSCs toward Schwann cells in chapter 2. After exposing hDPSCs to a step-by-step cytokine stimulation protocol, the basic method of Schwann cell induction from MSCs [248], they acquired the stereotypical Schwann cell bipolar morphology and expressed higher levels of glial markers such as p75NTR, laminin, GFAP, CD104, BDNF, GDNF, b-NFG and NT-3 (Table 6.1). Whereas p75NTR plays a role in many phases of the generation of Schwann cells, GFAP, NT-3 and laminin are only significantly expressed by immature and repair Schwann cells [4]. The neurotrophic factors BDNF and GDNF are main regulators of Schwann cell development. Furthermore, these signalling molecules secreted by Schwann cells or neurons promote myelination via mechanisms which remain to be determined. It has also been shown that the Schwann cell injury response is coupled with the upregulation of GDNF, BDNF, NT-3, NGF and VEGF [14, 249, 250]. So based on glial marker expression, our findings suggest that d-hDPSCs are very similar to repair Schwann cells. In line with this statement, we were able to demonstrate the functionality of the neurotropic growth factors *in vitro*, since d-hDPSCs exhibited enhanced neuronal survival and neurite elongation compared to undifferentiated hDPSCs (Table 6.1). *In vivo* studies revealed that this process is controlled by the

transcription factor c-Jun, since paracrine signalling via BDNF, GDNF and NGF was significantly downregulated in the absence of c-Jun, thereby impairing motor neuron survival and axonal growth [9, 14].

In chapter 3, we were able to confirm the positive effects of hDPSCs on endothelial cell migration and tube formation as described previously [185] and we showed that d-hDPSCs secreted significantly more VEGF compared to hDPSCs (Table 6.1). Interestingly, an important feature of repair Schwann cells *in vivo* is their increased VEGF production in response to nerve injury [250]. The fact that the pro-angiogenic actions of d-hDPSCs were comparable to but not better than those of hDPSCs could be explained by the pleiotropic effects of VEGF. Others have demonstrated that VEGF is not only involved in neovascularization but also in modulating physiological nerve repair. For example, studies have shown that damage to peripheral nerves induced increased expression of VEGF, which in turn accelerated growth and functional repair of the injured nerves [251, 252]. In addition, besides promoting Schwann cell survival, VEGF also exerts mitogenic actions on Schwann cells [253], thereby showing great potential for VEGF-secreting d-hDPSCs as a therapy for PNI.

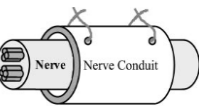
Integrins are known to play a major role during Schwann cell migration, proliferation and myelination during both development and peripheral nerve regeneration [254]. Focusing on the collagen-binding integrins $\alpha1\beta1$, $\alpha2\beta1$ and $\alpha11\beta1$ in chapter 5, we were able to detect the expression of the subunits $\alpha1$, $\alpha11$ and $\beta1$ but not $\alpha2$ in d-hDPSCs (Table 6.1). Previous *in vitro* and *in vivo* work has described the abundant presence of integrin $\alpha1\beta1$ but only low levels of $\alpha2\beta1$ in immature and non-myelinating Schwann cells [226, 255]. Furthermore, whereas axonal contact triggers downregulation of integrin $\alpha1\beta1$ in myelin-forming Schwann cells, axonal damage induces upregulation of this heterodimer in repair Schwann cells [254, 256-258], which supports our theory that *in vitro* cultured d-hDPSCs resemble repair Schwann cells. Although the expression of integrin $\alpha11\beta1$ in developing or mature Schwann cells has not been documented so far, this receptor regulates the survival of MSCs on collagen type I surfaces [233], pointing to the preservation of some stem cell characteristics by d-hDPSCs.

Besides evidence of successful differentiation of hDPSCs toward repair Schwann cells at the morphological and molecular level, which do not necessarily parallel cellular behaviour and actions, functional characterization of these cells *in vitro* is

indispensable. In addition to the angiogenic properties of d-hDPSCs as described before, these cells also promoted the survival and axonal outgrowth of *in vitro* 2D cultured neurons (Chapter 2) (Table 6.1). Furthermore, contraction assays performed in chapter 5 indicated the contractile capacity of d-hDPSCs within collagen type I hydrogels. This property allows d-hDPSC to self-align within a tethered hydrogel construct (Table 6.2), thereby mimicking the bands of Büngner in native peripheral nerves. Further exploration of the *in vitro* functionality of this 3D EngNT revealed that when neurons were seeded on top or within this construct, neurites were respectively guided unidirectional and myelinated by d-hDPSCs (Chapter 2) (Table 6.2). While numerous studies have reported the differentiation of MSCs toward Schwann cells that are neuroprotective and neuroregenerative, features that are important in the first phase of peripheral nerve regeneration, data on proper myelin formation, which is crucial for the recovery of neuronal function, by MSC-derived Schwann-like cells are limited [248]. Given the promising results obtained with d-hDPSC *in vitro*, their use as a potential treatment strategy for PNI can be considered.

Although d-hDPSCs possess favourable Schwann-like properties with regard to neurotrophic support and myelin production, the injury-induced plasticity that is observed in native Schwann cells [9] remains yet to be elucidated in d-hDPSCs. To this end, it would be very interesting to determine the phenotype of d-hDPSCs in a 3D coculture model at the different time points in the neuroregenerative process and determine if these cells possess the functional capacity to alter their phenotype accordingly in the setting of PNI to ensure optimal neural regeneration.

Table 6.2: Functional properties of d-hDPSCs in EngNT *in vitro* and *in vivo*.

<p><i>In vitro</i></p> <p>d-hDPSCs alignment Collagen type I alignment Neurite outgrowth guidance Neurite myelination</p>	
<p><i>In vivo</i></p> <p>Number of blood vessels ~ allograft Number of ingrowing neurites ~ allograft Number of myelinated neurites ~ empty conduit</p>	

Taken together, isolated hDPSCs were exposed to a step-by-step cytokine protocol to evaluate their glial differentiation capacity. The investigated morphological, ultrastructural, molecular and functional *in vitro* properties of d-hDPSCs are highly suggestive of successful differentiation into authentic (repair) Schwann cells. The preservation of some stem cell characteristics, such as the proliferative and collagen type I contractile capacity of d-hDPSCs, is advantageous when considering these cells for neural tissue engineering applications.

Does EngNT containing d-hDPSCs promote peripheral nerve regeneration *in vivo*?

Despite the spontaneous regenerative capacity of the PNS, large gap PNIs require bridging strategies. The disadvantages and suboptimal results associated with autografts in the clinic have sparked the search for alternative treatments. As recently reviewed, several tissue engineered constructs have been postulated as peripheral nerve grafts that connect the proximal and the distal nerve stump [259, 260]. Ideally, the most important aspects of nerve tissue must be incorporated in the device order to match the native regenerative potential. Via a combinatorial approach, a scaffold and a cellular component are often used to reconstruct peripheral nerves. In chapter 3, a NeuraWrap™ conduit was used to provide an interface between the nerve and the surrounding tissue comparable to the epineurium. The EngNT containing d-hDPSCs not only mimics the endoneurial microstructure by providing an anisotropic collagen type I matrix but also presents an alternative Schwann cell population in an aligned manner as described in chapter 2. A 15 mm gap in a rat sciatic model, which is most commonly described to study peripheral nerve regeneration [176], was used to assess the neuroregenerative potential of EngNT containing d-hDPSCs. Following 8 weeks of transplantation, the proximal part of the EngNT construct showed nerve tissue and vasculature comparable to that of the allograft transplants. However, the growth of neurites throughout the scaffold and myelination of these neurites was not up to the measures of the gold standard treatment (Table 6.2).

These results may be explained by the time frame of transplantation applied in this study. A recovery period of 8 weeks is relatively short for a 15 mm rat sciatic nerve gap, leading to only poor regeneration using empty conduits [143, 261].

Functional recovery of such large defects, so regeneration across the whole construct and profound myelination, is only observed after a longer period of time (10-12 weeks) [262-264]. In addition, since this was the first time that human cells were applied in EngNT *in vivo*, an immunosuppressant was administered to all animals in this study. However, the use of Cyclosporine A can have a direct growth inhibitory action on neurites [198], thereby hampering neuroregeneration. Therefore, we believe that future experiments should consider one of the two following options: (i) avoid the use of immunosuppressants in all groups to evaluate the immune response of the host tissue to human cells, which could both have beneficial or detrimental effects on neuroregeneration or (ii) use an animal model lacking cell-mediated immune response such as athymic nude rats, thereby facilitating xenograft transplantation [265, 266].

Taken together, this study was the first to report the *in vivo* formation of vascularized nerve tissue by EngNT containing d-hDPSCs. Adjustments of the transplantation protocol are required to optimize the cellular microenvironment and facilitate neurite growth and myelination from the proximal to the distal nerve stump.

Can SHG microscopy and ICS analysis be used to map local changes in self-aligning cellular collagen type I hydrogels?

Non-destructive imaging of fibrillar hydrogels has gained significant interest in the field of tissue engineering. Over the past decade, various label-free techniques have been applied to visualize collagen type I fibrils. In this work, the imaging tool of preference was SHG microscopy since it offers both high resolution and contrast. To circumvent the issues associated with manual data analysis, which is time-consuming and often dependent on subjective assessment, and to implement the polarization dependency of the SHG signal, our research group has recently proposed an alternative ICS model to quantify characteristics of randomly oriented collagen fibrils in a hydrogel imaged by SHG microscopy. We have now extended this approach to include the orientation distribution of fibrils in cellular hydrogels and showed the power of this model in two biologically relevant applications.

Since acellular collagen hydrogels possess a homogeneous microstructure, random SHG images can provide overall structural characterization of these matrix scaffolds [132]. However, hydrogels seeded with cells undergo contraction as a consequence of cell-generated tension. SHG microscopy and ICS analysis have been applied to predict bulk mechanical properties of such cellularized collagen hydrogels, obtaining smaller pores, larger fiber bundles and higher collagen concentrations during the course of cell-mediated hydrogel contraction [267]. However, detailed information on very local changes with respect to the collagen concentration and fibril orientation is important to understand how cells interact with their ECM. As described in chapter 4, we showed that the extended ICS model can be applied on SHG images to quantitatively capture very subtle temporal and spatial changes in collagen type I microstructure. Therefore, we believe that this technique is a valuable tool for non-invasive high-throughput screening of tissue engineered collagen type I hydrogels or to monitor ECM alterations during disease progression. For example, quantitative data on the main direction, density and microarchitecture of collagenous tissues has enabled researchers to make a distinction between healthy and skin or breast carcinomas [268, 269]. Furthermore, the capacity to image living cells in a 3D scaffold enhances the ability to understand fundamental cellular behaviour such as local ECM degradation or deformation to provide a more suitable environment for cell migration [270]. Insights in these general biophysical processes will also add to the understanding of matrix remodelling during inflammation, tissue repair and cancer metastasis.

What is the contractile capacity of hDPSCs and d-hDPSCs and which integrins are involved?

Contraction of collagen type I hydrogels is an essential step in the formation of EngNT. Encapsulated cells can interact with their surrounding ECM via membrane receptors, thereby exerting forces that can lead to substrate deformation or remodelling [217]. In chapter 5, we demonstrated that hDPSCs and d-hDPSCs have the same capacity to contract free-floating collagen type I hydrogels, with d-hDPSCs being more efficient. Protein levels of integrin $\beta 1$ were significantly higher in d-hDPSCs compared to hDPSCs, and blocking of this subunit markedly

affected hydrogel contraction by both cell types. The heterodimeric nature of integrin receptors suggests the involvement of another subunit. However, we did not find a difference in the expression of integrin $\alpha 1$, $\alpha 2$ and $\alpha 11$ subunits between hDPSCs and d-hDPSCs. Furthermore, inhibition of the $\alpha 1$ subunit has no effect whatsoever on hydrogel contraction. However, it has been demonstrated that PDGF $\alpha\alpha$, which is present in the full differentiation medium of d-hDPSCs, induces a significant decrease in the level of integrin $\alpha 1$ present on the cell surface [271]. Therefore, it might be interesting to investigate if d-hDPSCs maintain their Schwann-like phenotype and integrin expression levels upon withdrawal of PDGF $\alpha\alpha$ after the induction of differentiation. Furthermore, when culturing these cells in collagen type I hydrogels, spontaneous differentiation might be enhanced since soft substrates have been shown to affect integrin activity and trafficking to modulate stem cell lineage specification [272].

In order to get a more detailed view on the contribution of certain collagen-binding integrin receptors in the process of hydrogel contraction, it would be of interest to inhibit the functionality of heterodimers instead of integrin subunits. Antagonizing integrin function can take place at different levels: integrin activation, ligand binding, the formation of focal adhesions or intracellular signalling pathways [273]. The most common approach involves targeting the receptor binding site by for example antibodies or small molecules such as disintegrins or synthetic compounds. Via competitive inhibition or steric hindrance, chances of natural ligand binding are restricted to a minimum and the receptors are kept in a non-functional state. However, since the blocked receptors are still present at the cell surface, functional redundancy i.e. compensation or rescue by other integrins with similar ligand-binding sites does not occur [114, 273].

Conclusion

Our results demonstrate that hDPSCs can differentiate toward functional Schwann-like cells *in vitro*. Their contractile capacity allows self-alignment of d-hDPSCs in collagen type I hydrogels, thereby creating EngNT that has neuroregenerative capacities *in vivo*. Although this construct holds great potential as a treatment for PNI, optimization of EngNT containing d-hDPSCs is necessary in order to match the nerve's innate regenerative potential. In that regard, we

demonstrated that label-free optical imaging by SHG microscopy and robust ICS analysis are useful tools to assess the development of complex engineered tissues. The future of nerve repair is challenging and adventurous, but the combination of d-hDPSCs and collagen type I hydrogels might offer new avenues for PNI therapy.

Chapter 7

Nederlandse samenvatting

Weefseltechnologie is een multidisciplinair domein waarbij biologie, biotechniek en klinische wetenschappen worden gecombineerd met als doel lichaamsstructuren te herstellen en/of te regenereren. De twee bouwstenen van regeneratieve geneeskunde, namelijk cellen en substraten, moeten zorgvuldig geselecteerd worden om aan de vereisten van specifieke weefseltypes te kunnen voldoen. Een ideaal substraat moet biocompatibel zijn en de natuurlijke architectuur van het gastweefsel nabootsen in termen van fysische en mechanische eigenschappen. Voor de behandeling van perifere zenuwschade hebben tal van onderzoekers getracht om de banden van Büngner, die trofische en richtinggevende ondersteuning voorzien in de vorm van gealigneerde Schwann cellen en collageen type I fibrillen, te recreëren. De nadelen die gepaard gaan met de isolatie en expansie van autologe Schwann cellen hebben de zoektocht naar alternatieve celbronnen aangewakkerd. De ontdekking van stamcellen wordt beschouwd als één van de belangrijkste medische doorbraken van de 20^{ste} eeuw. Omwille van hun opmerkelijk capaciteit tot zelfvernieuwing en differentiatie tot verschillende celtypes hebben verschillende studies zich toegelegd op het gebruik van stamcellen voor weefseltechnologietoepassingen. Hoewel zenuwregeneratie bevorderd kan worden voor uiteenlopende stamcelpopulaties, heeft het domein van zenuwweefseltechnologie het afgelopen decennium beduidend veel interesse getoond in humane dentale pulpastamcellen (hDPSCs). Des te meer de getransplanteerde cellen gelijken op en zich gedragen als de gastcellen, des te effectiever en efficiënter kan het beschadigde weefsel geregenereerd worden. Daarom zou de transplantatie van Schwanncellen die voortkomen uit hDPSCs significant de regeneratie van perifere zenuwweefsel kunnen bevorderen.

Deze doctoraatsthesis had als doel om hDPSCs te differentiëren tot Schwanncellen (d-hDPSCs) en de algemene karakteristieken alsook het neuroregeneratief potentieel van deze d-hDPSCs na te gaan. In eerste instantie onderzochten we de *in vitro* gliale differentiatiecapaciteit van hDPSCs op het gebied van morfologie, cytochemie en ultrastructuur, alsook de neuroprotectieve, neurotrofische en angiogene effecten van hDPSCs en d-hDPSCs in 2D *in vitro* modellen (voornaamste resultaten zijn samengevat in Tabel 6.1). Vervolgens werd een 3D collageen type I hydrogel systeem gebruikt om te bestuderen in welke mate d-hDPSCs kunnen zelfaligneren en hergroei van zenuwuitlopers kunnen geleiden. Daarbij onderzochten we de veelzijdige neuroregeneratieve activiteiten van h-

DPSCs in een gevestigd en veelgebruikt diermodel dat zich perfect leent tot het bestuderen van perifeer zenuwherstel. De belangrijkste bevindingen hiervan zijn samengevat in Tabel 6.2. Om meer inzicht te krijgen in het proces van de totstandkoming van gefabriceerd zenuwweefsel (EngNT) werden de microstructurele veranderingen in de fibrillaire hydrogelarchitectuur in kaart gebracht en gekwantificeerd op een labelvrije beeldvormingsmanier en met behulp van een robuust analysemodel. Ten slotte hebben we verschillende experimenten uitgevoerd om de onderliggende mechanismen van collageen type I hydrogelcontractie door hDPSCs en d-hDPSCs te onthullen. De belangrijkste resultaten en bevindingen worden in onderstaande paragrafen samengevat en besproken.

Kunnen hDPSCs *in vitro* differentiëren tot Schwann cellen?

Sinds de eerste succesvolle differentiatie van mesenchymale stamcellen (MSCs) tot functionele Schwanncellen hebben talrijke studies beschreven hoe verschillende MSC-bronnen zoals beenmerg, vetweefsel en navelstreng Schwannachtige cellen kunnen genereren. DPSCs vertegenwoordigen een MSC-populatie die voortkomt uit migrerende cellen van de neurale lijst. Ze delen hun evolutionele oorsprong met Schwanncellen en brengen reeds in een ongedifferentieerde toestand merkers tot expressie die geassocieerd worden met neurale fenotypes. DPSCs zouden bijgevolg voorbeschikt kunnen zijn voor Schwannceldifferentiatie. We onderzochten het potentieel van hDPSCs om *in vitro* te differentiëren tot Schwanncellen in hoofdstuk 2. Na blootstelling van hDPSCs aan een stap-voor-stap cytokinestimulatieprotocol, tevens de basismethode voor Schwanncelinductie van MSCs, verworven deze cellen de stereotypische bipolaire Schwanncelmorfologie en brachten ze hogere levels van gliale merkers zoals p75NTR, laminine, GFAP, BDNF, GDNF, b-NGF en NT-3 tot expressie. Terwijl p75NTR een rol speelt tijdens verschillende fasen van Schwanncelontwikkeling, worden GFAP, NT-3 en laminine alleen beduidend tot expressie gebracht door immature en herstel-Schwanncellen. De neurotrofe factoren BDNF en GDNF zijn algemene regulatoren van Schwanncelontwikkeling. Daarnaast bevorderen deze signaalmoleculen, die gesecreteerd worden door Schwanncellen of neuronen, myelinisatie via mechanismen die nog onthuld moeten worden. Het is ook

aangetoond dat de reactie van Schwanncellen op zenuwschade gepaard gaan met de opregulatie van de eiwitten GDNF, BDNF, NT-3, NGF en VEGF. Dus gebaseerd op de expressie van gliale merkers wijzen onze gegevens erop dat d-hDPSCs het meest gelijken op herstel-Schwanncellen. Verder waren we, in overeenstemming met deze uitspraak, in staat om de functionaliteit van de neurotrofe groeifactoren *in vitro* aan te tonen: d-hDPSCs vertoonden namelijk een sterkere toename in de overleving van neuronen en de lengte van uitgroeiende neurieten in vergelijking met hDPSCs. *In vivo* studies hebben aan het licht gebracht dat dit proces gecontroleerd wordt door de transcriptiefactor c-Jun, aangezien paracrine signaaltransductie via BDNF, GDNF en NGF sterk verminderd was in de afwezigheid van c-Jun, waardoor de overleving en axonale groei van motorneuronen werd aangetast.

In hoofdstuk 3 konden we de reeds eerder beschreven positieve effecten van hDPSCs op endotheliale migratie en tubulogenese bevestigen en toonden we aan dat hDPSCs noemenswaardig meer VEGF secreteerden in vergelijking met hDPSCs. Opvallend is dat het verhogen van VEGF-productie als reactie op zenuwschade een belangrijke *in vivo* eigenschap is van herstel-Schwann cellen. Het feit dat de pro-angiogene acties van d-hDPSCs vergelijkbaar maar niet beter waren dan die van hDPSCs zou verklaard kunnen worden door de pleiotrope effecten van VEGF. Andere groepen hebben namelijk gedemonstreerd dat VEGF niet alleen betrokken is bij neovascularisatie maar ook bij het moduleren van fysiologisch zenuwherstel. Studies hebben bijvoorbeeld aangetoond dat schade aan perifere zenuwen verhoogde expressie van VEGF teweegbrengt, dat op zijn beurt zowel groei als functioneel herstel van de beschadigde zenuwen bevorderde. Bovendien komt dit niet enkel de overlevingskansen van Schwanncellen ten goede, maar oefent VEGF ook mitogene effecten uit op Schwanncellen, waardoor VEGF-secreterende d-hDPSCs vele mogelijkheden bieden als therapie voor perifere zenuwschade.

Het is reeds geweten dat integrines een belangrijke rol spelen tijdens Schwanncelmigratie, -proliferatie en -myelinisatie, zowel tijdens de ontwikkeling van Schwanncellen als tijdens perifere zenuwregeneratie. Hoofdstuk 5 richt zich voornamelijk op de collageen-bindende integrines $\alpha 1\beta 1$, $\alpha 2\beta 1$ en $\alpha 11\beta 1$. We waren in staat om de expressie van de subeenheden $\alpha 1$, $\alpha 11$ en $\beta 1$ maar niet $\alpha 2$ te detecteren in d-hDPSCs. Eerdere *in vitro* en *in vivo* studies beschreven reeds

de overvloedige aanwezigheid van integrine $\alpha 1\beta 1$ maar slechts lage levels van $\alpha 2\beta 1$ in immature en niet-myeliniserende Schwanncellen. Daarnaast werd aangetoond dat axonaal contact de expressie van integrine $\alpha 1\beta 1$ in myelinevormende Schwanncellen doet afnemen, terwijl axonale schade de opregulatie van dit heterodimeercomplex teweegbrengt. Dit ondersteunt onze theorie dat *in vitro* gekweekte d-hDPSCs vooral lijken op herstel-Schwanncellen. Hoewel de expressie van integrine $\alpha 1\beta 1$ in ontwikkelende of mature Schwanncellen tot nu toe nog niet gedocumenteerd is, reguleert deze receptor de overleving van MSCs op collageen type I oppervlakken, wat wijst op het behoud van bepaalde stamceleigenschappen bij d-hDPSCs.

Afgezien van het morfologisch en moleculair bewijs van succesvolle differentiatie van hDPSCs tot herstel-Schwanncellen, dat niet noodzakelijk overeenstemt met het gedrag en de werking van cellen, is *in vitro* functionele karakterisatie van deze cellen onontbeerlijk (Tabel 6.1). Naast de angiogene eigenschappen van d-hDPSCs zoals eerder beschreven, promoten deze cellen ook de overleving en axonale uitgroei van *in vitro* 2D gekweekte neuronen (Hoofdstuk 2). Daarnaast toonden de contractieassays die werden uitgevoerd in hoofdstuk 5 de contractiele capaciteit van d-hDPSCs in collageen type I hydrogelen aan. Deze eigenschap staat d-hDPSCs toe om te zelfaligneren in een vastgemaakt hydrogelconstruct (Tabel 6.2), waardoor de banden van Büngner zoals deze voorkomen in perifere zenuwen nagebootst worden. Verdere exploratie van de *in vitro* functionaliteit van dit 3D EngNT onthulde dat wanneer neuronen bovenop dit construct uitgezaaid werden, hun neurieten respectievelijk unidirectioneel geleid en ook gemyeliniseerd warden door d-hDPSCs (Hoofdstuk 2). Hoewel verscheidene studies de differentiatie van MSCs tot neuroprotectieve en neuroregeneratieve Schwanncellen hebben gerapporteerd, eigenschappen die zeer belangrijk zijn in de eerste fase van perifere zenuwregeneratie, zijn data met betrekking tot goede myelinevorming door deze MSC-afkomstige Schwann-achtige cellen, dat cruciaal is voor het herstel van zenuwfuncties, beperkt. Gezien de veelbelovende resultaten die *in vitro* bekomen werden met d-hDPSCs, kan hun gebruik als potentiële behandelingsstrategie voor perifere zenuwschade overwogen worden. Hoewel d-hDPSCs gunstige Schwannceleigenschappen hebben met betrekking tot neurotrofe ondersteuning en myelinevorming, is nog niet bekend of deze d-hDPSCs beschikken over de schade-geïnduceerde plasticiteit die wordt

waargenomen bij natuurlijk Schwanncellen. Daarom zou het erg interessant zijn om te het fenotype van d-hDPSCs in een 3D cocultuurmodel op verschillende tijdstippen van het neuroregeneratieve proces te bepalen en na te gaan of deze cellen effectief in staat zijn om hun fenotype te wijzigen in het kader van perifere zenuwschade om zo optimale neurale regeneratieve te verzekeren.

Samengevat werden geïsoleerde hDPSCs blootgesteld aan een stap-voor-stap cytokinestimulatieprotocol om hun gliale differentiatiecapaciteit te evalueren. De onderzochte morfologische, ultrastructurele, moleculaire en functionele *in vitro* eigenschappen van d-hDPSCs wijzen sterk in de richting van succesvolle differentiatie tot authentieke (herstel-) Schwanncellen. Het behoud van bepaalde stamceleigenschappen, zoals de proliferatieve en collageen type I contractiele capaciteit van d-hDPSCs, zijn erg voordelig wanneer deze cellen in overweging worden genomen voor zenuwweefsel technologie-toepassingen.

Wordt perifeer zenuwherstel bevorderd door EngNT dat d-hDPSCs bevat?

Ondanks de spontane regeneratieve capaciteit van het perifeer zenuwstelsel, vereisen grote defecten in perifere zenuwen overbruggingsstrategieën. De nadelen en suboptimale resultaten die men in het ziekenhuis bekommt met autografts hebben de zoektocht naar alternatieve behandelingen gestimuleerd. Zoals recentelijk werd besproken, zijn verschillende weefseltechnologie-constructen reeds gesuggereerd als perifere zenuwtransplantaten die het proximale en distale zenuwuiteinde met elkaar verbinden. Idealitair moeten de belangrijkste aspecten van zenuwweefsel geïncorporeerd worden in het construct om zo het normaal regeneratief potentieel te evenaren. Door middel van een combinatorische aanpak worden constructen en cellulaire componenten vaak gebruikt om perifere zenuwen te reconstrueren. In hoofdstuk 3 werd het gebruik van een NeuraWrap™ buisje als epineurium beschreven, waarmee het een interface vormt tussen de regenererende zenuw zelf en het omliggende weefsel. Het EngNT dat d-hDPSCs bevat bootst met zijn anisotropische collageen type I matrix niet alleen de endoneurale microstructuur na, maar biedt ook een alternatieve Schwanncelpopulatie aan op een gealigneerde manier zoals beschreven in hoofdstuk 2. Een diermodel dat in het kader van perifeer zenuwherstel vaak gebruikt wordt om de doeltreffendheid van alternatieve

behandelingen te onderzoeken, werd in deze studie gebruikt om het neuroregeneratief potentieel van EngNT dat d-hDPSCs bevat te evalueren. Na een herstelperiode van 8 weken na de transplantatie, vertoonde het proximale deel van het EngNT construct een vergelijkbare mate aan zenuwweefsel en vasculatuur als de allografttransplantaten. De groei van neurieten doorheen het construct en myelinisatie van deze neurieten was echter niet naar maatstaven van de huidige klinische voorkeursbehandeling.

Deze resultaten kunnen verklaard worden door de beperkte looptijd van deze studie. Een herstelperiode van 8 weken is relatief kort voor een 15 mm zenuwdefect en het gebruik van holle zenuwbuizen leidt hier slechts tot gebrekkige regeneratie. Functioneel herstel van zulke grote defecten, wat regeneratie en myelinisatie over de volledige lengte van het construct impliceert, wordt enkel waargenomen na langere herstelperiodes (10-12 weken). Aangezien het de eerste maal was dat humane cellen *in vivo* werden gebruikt in EngNT, werd ook een immunosuppressivum (Cyclosporine A) toegediend aan alle dieren in deze studie. Het gebruik van Cyclosporine A kan echter een rechtstreekse negatieve impact hebben op de groei van neurieten, waardoor het neuroregeneratieve proces wordt belemmerd. Daarom zijn we van mening dat toekomstige experimenten één van de volgende opties in overweging moet nemen: (i) het gebruik van immunosuppressiva vermijden in alle groepen om zo het effect van de immuunrespons van het gastweefsel op de toegediende humane cellen te kunnen evalueren of (ii) een diermodel gebruiken waarbij geen celgemedieerde immuunrespons mogelijk is zodat xenografttransplantatie wordt gefaciliteerd.

Dit was de eerste studie die de *in vivo* vorming van gevasculariseerd zenuwweefsel door EngNT met d-hDPSCs beschreef. Aanpassingen van het transplantatieprotocol zijn noodzakelijk om de cellulaire micro-omgeving te optimaliseren en om neurietuitgroei en myelinisatie van het proximale naar het distale zenuwuiteinde te bevorderen.

Kunnen *second harmonic generation* (SHG) microscopie en *image correlation spectroscopy* (ICS) analyse gebruikt worden om lokale veranderingen in zelfalignerende cellulaire collageen type I hydrogelen in kaart te brengen?

Niet-destructieve beeldvorming van fibrillaire hydrogelen heeft in het veld van weefseltechnologie veel belangstelling gewonnen. Tijdens het afgelopen decennium werden verschillende labelvrije technieken toegepast om collageen type I fibrillen te visualiseren. In dit werk is gekozen voor beeldvorming met SHG-microscopie omwille van de resolutie en het contrast. Omdat manuele gegevensanalyse vaak tijdsrovend is en tevens afhangt van een subjectief oordeel, en om de polarisatieafhankelijkheid van het SHG-signaal in rekening te brengen, stelde onze onderzoeksgroep recentelijk een alternatief ICS-model voor om de karakteristieken van willekeurig georiënteerde collageenfibrillen in een SHG-gevisualiseerde hydrogel te kwantificeren. Deze benadering hebben we nu uitgebreid zodat ook de niet-uniforme oriëntatieverdeling van fibrillen in cellulaire hydrogelen bepaald kan worden. De kracht en bruikbaarheid van dit model hebben we aangetoond in twee biologisch relevante toepassingen.

Aangezien acellulaire collageenhydrogelen over een homogene microstructuur beschikken, laten willekeurig genomen SHG-beelden algemene structurele karakterisatie van deze matrixplatformen toe. Cellulaire hydrogelen, daarentegen, ondergaan locale contractie als gevolg van spanningen gegenereerd door deze geïncorporeerde cellen. SHG-microscopie en ICS-analyse zijn reeds gebruikt om de algemene mechanische eigenschappen van zulke cellulaire collageenhydrogelen te voorspellen. Zo bepaalde men dat tijdens het verloop van celgedieerde hydrogelcontractie de poriën kleiner en de fiberbundels en collageenconcentraties groter werden. Om echter te kunnen begrijpen hoe cellen interactie aangaan met hun ECM is het belangrijk om lokale veranderingen met betrekking tot de collageenconcentratie en fibriloriëntatie gedetailleerd te bestuderen. Zoals beschreven in hoofdstuk 4, toonden we aan dat ons uitgebreide ICS-model toegepast kan worden op SHG-beelden om kwantitatief zeer subtiele temporele en spatiële veranderingen in collageen type I microstructuren te detecteren. Daarom geloven wij dat deze techniek potentieel heeft om op niet-invasieve manier weefseltechnologise collageen type I hydrogelen te screenen

op grote schaal of om ECM wijzigingen tijdens bepaalde ziektebeelden nauwgezet op te volgen. Zo zijn onderzoekers er bijvoorbeeld al in geslaagd om aan de hand van gegevens over de algemene ordening, dichtheid en microarchitectuur van collageuze structuren een onderscheid te maken tussen gezond weefsel en huid- en borstkankers. Verder kan de mogelijkheid om levende cellen in hun 3D matrix in beeld te brengen ook bijdragen tot de fundamentele kennis van cellulair gedrag, bijvoorbeeld om een meer geschikte omgeving te voorzien voor celmigratie zal vaak lokale ECM-afbraak of -vervorming plaatsvinden. Inzichten in deze algemene biofysische processen zullen dus ook leiden tot meer begrip van herschikking van de ECM tijdens inflammatie, weefselherstel en kankermetastase.

Wat is de contractiele capaciteit van hDPSCs en d-hDPSCs en welke integrines zijn hierin betrokken?

Contractie van collageen type I hydrogelen is een essentiële stap in de vorming van EngNT. Ingekapselde cellen kunnen in interactie treden met hun omringende ECM via membraanreceptoren, waardoor ze krachten uitoefenen die kunnen leiden tot hydrogelvervorming of -herschikking. In hoofdstuk 5 demonstreerden we dat hDPSCs en d-hDPSCs dezelfde capaciteit hebben om rondrijvende collageen type I hydrogelen te contraheren, maar dat d-hDPSCs hier efficiënter in zijn. Eiwitniveaus van integrine $\beta 1$ in d-hDPSCs waren beduidend hoger in vergelijking met hDPSCs, en het blokkeren van deze subeenheid had een sterke negatieve invloed op hydrogelcontractie door beide celtypes. De heterodimere aard van integrinereceptoren suggereert de betrokkenheid van een andere subeenheid. We konden echter geen verschil vinden in de expressie van integrine $\alpha 1$, $\alpha 2$ en $\alpha 11$ subeenheden tussen hDPSCs en d-hDPSCs. Ook had het inhiberen van de $\alpha 1$ subeenheid geen enkel effect op hydrogelcontractie. Wel werd er eerder aangetoond dat PDGF α , een groeifactor die aanwezig is in het complete differentiatie-medium van d-hDPSCs, een significante afname van integrine $\alpha 1$ in het celmembraan veroorzaakt. Om deze reden is het zeer interessant zijn om na te gaan of d-hDPSCs hun Schwanncel-achtig fenotype en integrine-expressieniveaus behouden wanneer PDGF α niet meer wordt toegevoegd na inductie van differentiatie. Daarnaast zou spontane differentiatie ook bevorderd kunnen worden wanneer deze cellen worden gekweekt in collageen type I

hydrogels aangezien men reeds heeft aangetoond dat zachte substraten de activiteit en circulatie van integrines beïnvloeden waardoor stamceldifferentiatie wordt gemoduleerd.

Om een gedetailleerder beeld te krijgen van de bijdrage van bepaalde collageenbindende integrinereceptoren in het proces van hydrogelcontractie, zou het interessant zijn om de functionaliteit van heterodimeren in plaats van integrinesubeenheden te inhiberen. Het tegenwerken van de integrinefunctie kan plaatsvinden op verschillende niveaus: integrineactivatie, ligandbinding, de vorming van focale adhesies of intracellulaire signalisatiecascades. De meest voorkomende aanpak omvat het doelgericht blokkeren van de receptorbindingsplaats met behulp van bijvoorbeeld antilichamen of kleine moleculen zoals disintegrines of synthetische moleculen. Door competitieve inhibitie of sterische belemmering zijn de kansen op natuurlijke ligandbinding beperkt tot een minimum en worden de receptoren in een niet-functionele staat gehouden. Aangezien de geblokkeerde receptoren nog steeds aanwezig zijn aan het celoppervlak, zullen andere integrines met gelijkaardige ligand bindingsplaatsen hier niet voor compenseren.

Algemene conclusie

Deze resultaten tonen aan dat hDPSCs in vitro kunnen differentiëren tot functionele Schwann-achtige cellen. Dankzij hun contractiele capaciteit is zelfalignering van deze d-hDPSCs in collageen type I hydrogelen mogelijk, waardoor een EngNT gegenereerd kan worden dat ook in vivo neuroregeneratief potentieel heeft. Hoewel dit construct zeer veelbelovend is als behandeling voor perifere zenuwschade, is het noodzakelijk om EngNT dat d-hDPSCs bevat te optimaliseren om uiteindelijk een vergelijkbare mate en kwaliteit van zenuwherstel te bekomen als het natuurlijke zenuwweefsel. In dat opzicht hebben we aangetoond dat labelvrije optische beeldvorming door SHG-microscopie en robuuste ICS-analyse bruikbare middelen zijn om de ontwikkeling van complexe weefseltechnologie te evalueren. De toekomst van zenuwherstel vormt een grote uitdaging, maar de combinatie van d-hDPSCs en collageen type I hydrogelen biedt nieuwe mogelijkheden voor de behandeling van perifere zenuwschade.

Reference list

1. Navarro, X., et al., *A critical review of interfaces with the peripheral nervous system for the control of neuroprostheses and hybrid bionic systems*. J Peripher Nerv Syst, 2005. **10**(3): p. 229-58.
2. Pabari, A., et al., *Modern surgical management of peripheral nerve gap*. J Plast Reconstr Aesthet Surg, 2010. **63**(12): p. 1941-8.
3. Jessen, K.R., R. Mirsky, and A.C. Lloyd, *Schwann Cells: Development and Role in Nerve Repair*. Cold Spring Harb Perspect Biol, 2015. **7**(7).
4. Jessen, K.R. and R. Mirsky, *The origin and development of glial cells in peripheral nerves*. Nat Rev Neurosci, 2005. **6**(9): p. 671-82.
5. Jessen, K.R., *Glial cells*. Int J Biochem Cell Biol, 2004. **36**(10): p. 1861-7.
6. Jessen, K.R. and R. Mirsky, *Negative regulation of myelination: relevance for development, injury, and demyelinating disease*. Glia, 2008. **56**(14): p. 1552-65.
7. Sango, K. and J. Yamauchi, *Schwann Cell Development and Pathology*, ed. K. Sango and J. Yamauchi. Vol. 1. 2014: Springer Japan. 174.
8. Lietz, M., et al., *Neuro tissue engineering of glial nerve guides and the impact of different cell types*. Biomaterials, 2006. **27**(8): p. 1425-36.
9. Arthur-Farraj, P.J., et al., *c-Jun reprograms Schwann cells of injured nerves to generate a repair cell essential for regeneration*. Neuron, 2012. **75**(4): p. 633-47.
10. Lee, H.J., Y.K. Shin, and H.T. Park, *Mitogen Activated Protein Kinase Family Proteins and c-jun Signaling in Injury-induced Schwann Cell Plasticity*. Exp Neurobiol, 2014. **23**(2): p. 130-7.
11. Lee, H.K., et al., *Proteasome inhibition suppresses Schwann cell dedifferentiation in vitro and in vivo*. Glia, 2009. **57**(16): p. 1825-34.
12. Holtzman, E. and A.B. Novikoff, *Lysosomes in the rat sciatic nerve following crush*. J Cell Biol, 1965. **27**(3): p. 651-69.
13. Gaudet, A.D., P.G. Popovich, and M.S. Ramer, *Wallerian degeneration: gaining perspective on inflammatory events after peripheral nerve injury*. J Neuroinflammation, 2011. **8**: p. 110.
14. Fontana, X., et al., *c-Jun in Schwann cells promotes axonal regeneration and motoneuron survival via paracrine signaling*. J Cell Biol, 2012. **198**(1): p. 127-41.
15. Seddon, H.J., *Three types of nerve injury*. Brain, 1943. **66**(4): p. 237-288.
16. Sunderland, S., *A classification of peripheral nerve injuries producing loss of function*. Brain, 1951. **74**(4): p. 491-516.
17. Mackinnon, S.E. and A.L. Dellon, *Surgery of the peripheral nerve*. 1988, New York: Thieme-Stratton Corp.
18. Gordon, T., N. Tyreman, and M.A. Raji, *The basis for diminished functional recovery after delayed peripheral nerve repair*. J Neurosci, 2011. **31**(14): p. 5325-34.

19. Millesi, H., *Bridging defects: autologous nerve grafts*. Acta Neurochir Suppl, 2007. **100**: p. 37-8.
20. Grinsell, D. and C.P. Keating, *Peripheral nerve reconstruction after injury: a review of clinical and experimental therapies*. Biomed Res Int, 2014. **2014**: p. 698256.
21. Daly, W., et al., *A biomaterials approach to peripheral nerve regeneration: bridging the peripheral nerve gap and enhancing functional recovery*. J R Soc Interface, 2012. **9**(67): p. 202-21.
22. di Summa, P.G., et al., *Adipose-derived stem cells enhance peripheral nerve regeneration*. J Plast Reconstr Aesthet Surg, 2010. **63**(9): p. 1544-52.
23. Murphy, M.B., K. Moncivais, and A.I. Caplan, *Mesenchymal stem cells: environmentally responsive therapeutics for regenerative medicine*. Exp Mol Med, 2013. **45**: p. e54.
24. Friedenstein, A.J., R.K. Chailakhjan, and K.S. Lalykina, *The development of fibroblast colonies in monolayer cultures of guinea-pig bone marrow and spleen cells*. Cell and Tissue Kinetics, 1970. **3**(4): p. 393-403.
25. Dominici, M., et al., *Minimal criteria for defining multipotent mesenchymal stromal cells. The International Society for Cellular Therapy position statement*. Cytotherapy, 2006. **8**(4): p. 315-7.
26. Lakshminpathy, U. and C. Verfaillie, *Stem cell plasticity*. Blood Reviews, 2005. **19**(1): p. 29-38.
27. Kopen, G.C., D.J. Prockop, and D.G. Phinney, *Marrow stromal cells migrate throughout forebrain and cerebellum, and they differentiate into astrocytes after injection into neonatal mouse brains*. Proceedings of the National Academy of Sciences of the United States of America, 1999. **96**(19): p. 10711-6.
28. Woodbury, D., et al., *Adult rat and human bone marrow stromal cells differentiate into neurons*. Journal of Neuroscience Research, 2000. **61**(4): p. 364-70.
29. Kamada, T., et al., *Transplantation of bone marrow stromal cell-derived Schwann cells promotes axonal regeneration and functional recovery after complete transection of adult rat spinal cord*. Journal of Neuropathology and Experimental Neurology, 2005. **64**(1): p. 37-45.
30. Zhao, C.P., et al., *Human mesenchymal stromal cells ameliorate the phenotype of SOD1-G93A ALS mice*. Cytotherapy, 2007. **9**(5): p. 414-26.
31. Tondreau, T., et al., *Gene expression pattern of functional neuronal cells derived from human bone marrow mesenchymal stromal cells*. BMC Genomics, 2008. **9**: p. 166.
32. Deng, J., et al., *Mesenchymal stem cells spontaneously express neural proteins in culture and are neurogenic after transplantation*. Stem Cells, 2006. **24**(4): p. 1054-64.

Reference list

33. Zuk, P.A., et al., *Human adipose tissue is a source of multipotent stem cells*. *Molecular Biology of the Cell*, 2002. **13**(12): p. 4279-95.
34. Erices, A., P. Conget, and J.J. Minguell, *Mesenchymal progenitor cells in human umbilical cord blood*. *British Journal of Haematology*, 2000. **109**(1): p. 235-42.
35. Estrela, C., et al., *Mesenchymal stem cells in the dental tissues: perspectives for tissue regeneration*. *Brazilian Dental Journal*, 2011. **22**(2): p. 91-8.
36. Sloan, A.J. and A.J. Smith, *Stem cells and the dental pulp: potential roles in dentine regeneration and repair*. *Oral Dis*, 2007. **13**(2): p. 151-7.
37. Jontell, M., et al., *Immune defense mechanisms of the dental pulp*. *Critical Reviews in Oral Biology and Medicine*, 1998. **9**(2): p. 179-200.
38. Smith, A.J., et al., *Reactionary dentinogenesis*. *International Journal of Developmental Biology*, 1995. **39**(1): p. 273-80.
39. Smith, A.J. and H. Lesot, *Induction and regulation of crown dentinogenesis: embryonic events as a template for dental tissue repair?* *Critical Reviews in Oral Biology and Medicine*, 2001. **12**(5): p. 425-37.
40. Gronthos, S., et al., *Postnatal human dental pulp stem cells (DPSCs) in vitro and in vivo*. *Proceedings of the National Academy of Sciences of the United States of America*, 2000. **97**(25): p. 13625-30.
41. Hilkens, P., et al., *Effect of isolation methodology on stem cell properties and multilineage differentiation potential of human dental pulp stem cells*. *Cell and Tissue Research*, 2013. **353**(1): p. 65-78.
42. Zhang, W., et al., *Multilineage differentiation potential of stem cells derived from human dental pulp after cryopreservation*. *Tissue Engineering*, 2006. **12**(10): p. 2813-23.
43. Woods, E.J., et al., *Optimized cryopreservation method for human dental pulp-derived stem cells and their tissues of origin for banking and clinical use*. *Cryobiology*, 2009. **59**(2): p. 150-7.
44. Lee, S.Y., et al., *Effects of cryopreservation of intact teeth on the isolated dental pulp stem cells*. *Journal of Endodontics*, 2010. **36**(8): p. 1336-40.
45. Pierdomenico, L., et al., *Multipotent mesenchymal stem cells with immunosuppressive activity can be easily isolated from dental pulp*. *Transplantation*, 2005. **80**(6): p. 836-42.
46. Tomic, S., et al., *Immunomodulatory properties of mesenchymal stem cells derived from dental pulp and dental follicle are susceptible to activation by toll-like receptor agonists*. *Stem Cells Dev*, 2011. **20**(4): p. 695-708.
47. Kerkis, I., et al., *Early transplantation of human immature dental pulp stem cells from baby teeth to golden retriever muscular dystrophy (GRMD) dogs: Local or systemic?* *J Transl Med*, 2008. **6**: p. 35.

48. Gronthos, S., et al., *Stem cell properties of human dental pulp stem cells*. Journal of Dental Research, 2002. **81**(8): p. 531-5.
49. Balic, A., et al., *Characterization of stem and progenitor cells in the dental pulp of erupted and unerupted murine molars*. Bone, 2010. **46**(6): p. 1639-51.
50. d'Aquino, R., et al., *Human postnatal dental pulp cells co-differentiate into osteoblasts and endotheliocytes: a pivotal synergy leading to adult bone tissue formation*. Cell Death and Differentiation, 2007. **14**(6): p. 1162-71.
51. Ishkitiev, N., et al., *High-purity hepatic lineage differentiated from dental pulp stem cells in serum-free medium*. Journal of Endodontics, 2012. **38**(4): p. 475-80.
52. Kiraly, M., et al., *Simultaneous PKC and cAMP activation induces differentiation of human dental pulp stem cells into functionally active neurons*. Neurochemistry International, 2009. **55**(5): p. 323-32.
53. Nakatsuka, R., et al., *5-Aza-2'-deoxycytidine treatment induces skeletal myogenic differentiation of mouse dental pulp stem cells*. Archives of Oral Biology, 2010. **55**(5): p. 350-7.
54. Paino, F., et al., *Ecto-mesenchymal stem cells from dental pulp are committed to differentiate into active melanocytes*. Eur Cell Mater, 2010. **20**: p. 295-305.
55. Stevens, A., et al., *Human dental pulp stem cells differentiate into neural crest-derived melanocytes and have label-retaining and sphere-forming abilities*. Stem Cells Dev, 2008. **17**(6): p. 1175-84.
56. Miura, M., et al., *SHED: stem cells from human exfoliated deciduous teeth*. Proc Natl Acad Sci U S A, 2003. **100**(10): p. 5807-12.
57. Huang, G.T., et al., *The hidden treasure in apical papilla: the potential role in pulp/dentin regeneration and bioroot engineering*. J Endod, 2008. **34**(6): p. 645-51.
58. Seo, B.M., et al., *Investigation of multipotent postnatal stem cells from human periodontal ligament*. Lancet, 2004. **364**(9429): p. 149-55.
59. Arthur, A., et al., *Adult human dental pulp stem cells differentiate toward functionally active neurons under appropriate environmental cues*. Stem Cells, 2008. **26**(7): p. 1787-95.
60. Janebodin, K., et al., *Isolation and characterization of neural crest-derived stem cells from dental pulp of neonatal mice*. PLoS One, 2011. **6**(11): p. e27526.
61. Martens, W., et al., *Expression pattern of basal markers in human dental pulp stem cells and tissue*. Cells Tissues Organs, 2012. **196**(6): p. 490-500.
62. Sakai, K., et al., *Human dental pulp-derived stem cells promote locomotor recovery after complete transection of the rat spinal cord by multiple*

- neuro-regenerative mechanisms*. Journal of Clinical Investigation, 2012. **122**(1): p. 80-90.
63. Nosrat, I.V., et al., *Dental pulp cells produce neurotrophic factors, interact with trigeminal neurons in vitro, and rescue motoneurons after spinal cord injury*. Developmental Biology, 2001. **238**(1): p. 120-32.
64. Nosrat, I.V., et al., *Dental pulp cells provide neurotrophic support for dopaminergic neurons and differentiate into neurons in vitro; implications for tissue engineering and repair in the nervous system*. European Journal of Neuroscience, 2004. **19**(9): p. 2388-98.
65. Mead, B., et al., *Intravitreally transplanted dental pulp stem cells promote neuroprotection and axon regeneration of retinal ganglion cells after optic nerve injury*. Investigative Ophthalmology and Visual Science, 2013. **54**(12): p. 7544-56.
66. Mead, B., et al., *Paracrine-mediated neuroprotection and neuritogenesis of axotomised retinal ganglion cells by human dental pulp stem cells: comparison with human bone marrow and adipose-derived mesenchymal stem cells*. PLoS One, 2014. **9**(10): p. e109305.
67. Ellis, K.M., et al., *Neurogenic potential of dental pulp stem cells isolated from murine incisors*. Stem Cell Res Ther, 2014. **5**(1): p. 30.
68. Aanismaa, R., et al., *Human dental pulp stem cells differentiate into neural precursors but not into mature functional neurons*. Stem Cell Discov., 2012. **2**: p. 85–91.
69. Osathanon, T., et al., *Neurogenic differentiation of human dental pulp stem cells using different induction protocols*. Oral Diseases, 2014. **20**(4): p. 352-8.
70. Gervois, P., et al., *Neurogenic maturation of human dental pulp stem cells following neurosphere generation induces morphological and electrophysiological characteristics of functional neurons*. Stem Cells Dev, 2015. **24**(3): p. 296-311.
71. Barnes, D. and G. Sato, *Serum-free cell culture: a unifying approach*. Cell, 1980. **22**(3): p. 649-55.
72. Tekkatte, C., et al., *"Humanized" stem cell culture techniques: the animal serum controversy*. Stem Cells Int, 2011. **2011**: p. 504723.
73. Hirata, T.M., et al., *Expression of multiple stem cell markers in dental pulp cells cultured in serum-free media*. J Endod, 2010. **36**(7): p. 1139-44.
74. Bonnamain, V., et al., *Human dental pulp stem cells cultured in serum-free supplemented medium*. Front Physiol, 2013. **4**: p. 357.
75. Zainal Ariffin, S.H., et al., *Differentiation of Dental Pulp Stem Cells into Neuron-Like Cells in Serum-Free Medium*. Stem Cells International, 2013.

76. Askari, N., et al., *Human Dental Pulp Stem Cells Differentiate into Oligodendrocyte Progenitors Using the Expression of Olig2 Transcription Factor*. *Cells Tissues Organs*, 2014. **200**(2): p. 93-103.
77. Apel, C., et al., *The neuroprotective effect of dental pulp cells in models of Alzheimer's and Parkinson's disease*. *Journal of Neural Transmission*, 2009. **116**(1): p. 71-8.
78. Nesti, C., et al., *Human dental pulp stem cells protect mouse dopaminergic neurons against MPP+ or rotenone*. *Brain Research*, 2011. **1367**: p. 94-102.
79. Huang, A.H., et al., *Putative dental pulp-derived stem/stromal cells promote proliferation and differentiation of endogenous neural cells in the hippocampus of mice*. *Stem Cells*, 2008. **26**(10): p. 2654-63.
80. Arthur, A., et al., *Implanted adult human dental pulp stem cells induce endogenous axon guidance*. *Stem Cells*, 2009. **27**(9): p. 2229-37.
81. Kiraly, M., et al., *Integration of neuronally predifferentiated human dental pulp stem cells into rat brain in vivo*. *Neurochem Int*, 2011. **59**(3): p. 371-81.
82. de Almeida, F.M., et al., *Human dental pulp cells: a new source of cell therapy in a mouse model of compressive spinal cord injury*. *Journal of Neurotrauma*, 2011. **28**(9): p. 1939-49.
83. Leong, W.K., et al., *Human adult dental pulp stem cells enhance poststroke functional recovery through non-neural replacement mechanisms*. *Stem Cells Transl Med*, 2012. **1**(3): p. 177-87.
84. Yang, K.L., et al., *A simple and efficient method for generating Nurr1-positive neuronal stem cells from human wisdom teeth (tNSC) and the potential of tNSC for stroke therapy*. *Cytherapy*, 2009. **11**(5): p. 606-17.
85. Sugiyama, M., et al., *Dental pulp-derived CD31(-)/CD146(-) side population stem/progenitor cells enhance recovery of focal cerebral ischemia in rats*. *Tissue Eng Part A*, 2011. **17**(9-10): p. 1303-11.
86. Sasaki, R., et al., *Tubulation with dental pulp cells promotes facial nerve regeneration in rats*. *Tissue Eng Part A*, 2008. **14**(7): p. 1141-7.
87. Sasaki, R., et al., *PLGA artificial nerve conduits with dental pulp cells promote facial nerve regeneration*. *J Tissue Eng Regen Med*, 2011. **5**(10): p. 823-30.
88. Yamamoto, T., et al., *Trophic Effects of Dental Pulp Stem Cells on Schwann Cells in Peripheral Nerve Regeneration*. *Cell Transplant*, 2015.
89. Young, F., A. Sloan, and B. Song, *Dental pulp stem cells and their potential roles in central nervous system regeneration and repair*. *J Neurosci Res*, 2013. **91**(11): p. 1383-93.
90. Gluck, T., *Ueber Neuroplastik auf dem Wege der Transplantation*. *Arch. Klin. Chir.*, 1880. **25**: p. 606-16.

91. Payr, E., *Beiträge zur Technik der Blutgefäss und Nervennaht nebst Mitteilungen über die Verwendung eines resorbibaren Metalles in der Chirurgie*. Arch. Klin. Chir., 1900. **62**: p. 67.
92. Kirk, E.G. and D. Lewis, *Fascial tubulization in the repair of nerve defects*. JAMA, 1915. **65**: p. 486-92.
93. Arslantunali, D., et al., *Peripheral nerve conduits: technology update*. Med Devices (Auckl), 2014. **7**: p. 405-24.
94. Bell, J.H. and J.W. Haycock, *Next generation nerve guides: materials, fabrication, growth factors, and cell delivery*. Tissue Eng Part B Rev, 2012. **18**(2): p. 116-28.
95. Chiono, V. and C. Tonda-Turo, *Trends in the design of nerve guidance channels in peripheral nerve tissue engineering*. Progress in Neurobiology, 2015.
96. Aurand, E.R., K.J. Lampe, and K.B. Bjugstad, *Defining and designing polymers and hydrogels for neural tissue engineering*. Neurosci Res, 2011.
97. Geckil, H., et al., *Engineering hydrogels as extracellular matrix mimics*. Nanomedicine (Lond), 2010. **5**(3): p. 469-84.
98. Levental, I., P.C. Georges, and P.A. Janmey, *Soft biological materials and their impact on cell function*. Soft Matter, 2007. **3**(3): p. 299-306.
99. Murphy, W.L., T.C. McDevitt, and A.J. Engler, *Materials as stem cell regulators*. Nature Materials, 2014. **13**(6): p. 547-557.
100. Balgude, A.P., et al., *Agarose gel stiffness determines rate of DRG neurite extension in 3D cultures*. Biomaterials, 2001. **22**(10): p. 1077-84.
101. Gunn, J.W., S.D. Turner, and B.K. Mann, *Adhesive and mechanical properties of hydrogels influence neurite extension*. J Biomed Mater Res A, 2005. **72**(1): p. 91-7.
102. Murugan, R. and S. Ramakrishna, *Design strategies of tissue engineering scaffolds with controlled fiber orientation*. Tissue Engineering, 2007. **13**(8): p. 1845-66.
103. Alberts, B., et al., *Molecular Biology of The Cell*. 2002, New York: Garland Science.
104. Friess, W., *Collagen--biomaterial for drug delivery*. Eur J Pharm Biopharm, 1998. **45**(2): p. 113-36.
105. Parenteau-Bareil, R., R. Gauvin, and F. Berthod, *Collagen-based biomaterials for tissue engineering applications*. Materials, 2010. **3**: p. 1863-1887.
106. Elsdale, T. and J. Bard, *Collagen Substrata for Studies on Cell Behavior*. Journal of Cell Biology, 1972. **54**(3): p. 626-&.
107. Lee, P., et al., *Microfluidic alignment of collagen fibers for in vitro cell culture*. Biomedical Microdevices, 2006. **8**(1): p. 35-41.

108. Cheng, X.G., et al., *An electrochemical fabrication process for the assembly of anisotropically oriented collagen bundles*. *Biomaterials*, 2008. **29**(22): p. 3278-3288.
109. Torbet, J., J.M. Freyssinet, and G. Hudry-Clergeon, *Oriented fibrin gels formed by polymerization in strong magnetic fields*. *Nature*, 1981. **289**(5793): p. 91-3.
110. Torbet, J. and M.C. Ronziere, *Magnetic Alignment of Collagen during Self-Assembly*. *Biochemical Journal*, 1984. **219**(3): p. 1057-1059.
111. Eastwood, M., et al., *Effect of precise mechanical loading on fibroblast populated collagen lattices: Morphological changes*. *Cell Motil Cytoskeleton*, 1998. **40**(1): p. 13-21.
112. Mudera, V.C., et al., *Molecular responses of human dermal fibroblasts to dual cues: Contact guidance and mechanical load*. *Cell Motil Cytoskeleton*, 2000. **45**(1): p. 1-9.
113. Hynes, R.O., *Integrins: bidirectional, allosteric signaling machines*. *Cell*, 2002. **110**(6): p. 673-87.
114. Barczyk, M., S. Carracedo, and D. Gullberg, *Integrins*. *Cell Tissue Res*, 2010. **339**(1): p. 269-80.
115. Takada, Y., X. Ye, and S. Simon, *The integrins*. *Genome Biol*, 2007. **8**(5): p. 215.
116. Goldman, R. and D. Spector, *Live Cell Imaging: A Laboratory Manual*. 2004, Cold Spring Harbor, NY: CSHL Press.
117. Teraski, M. and M.E. Dailey, *Confocal microscopy of living cells.*, in *Handbook of Biological Confocal Microscopy*. 1995, Plenum Press: New York.
118. Artym, V.V. and K. Matsumoto, *Imaging cells in three-dimensional collagen matrix*. *Curr Protoc Cell Biol*, 2010. **Chapter 10**: p. Unit 10 18 1-20.
119. Isobe, K., W. Watanabe, and K. Itoh, *Nonlinear optical microscopy*, in *Functional Imaging by Controlled Nonlinear Optical Phenomena*. 2013, John Wiley & Sons.
120. Helmchen, F. and W. Denk, *Deep tissue two-photon microscopy*. *Nat Methods*, 2005. **2**(12): p. 932-40.
121. Thomas, G., et al., *Advances and challenges in label-free nonlinear optical imaging using two-photon excitation fluorescence and second harmonic generation for cancer research*. *J Photochem Photobiol B*, 2014. **141**: p. 128-38.
122. Guo, H.W., et al., *Reduced nicotinamide adenine dinucleotide fluorescence lifetime separates human mesenchymal stem cells from differentiated progenies*. *J Biomed Opt*, 2008. **13**(5): p. 050505.

123. Konig, K., A. Uchugonova, and E. Gorjup, *Multiphoton fluorescence lifetime imaging of 3D-stem cell spheroids during differentiation*. *Microsc Res Tech*, 2011. **74**(1): p. 9-17.
124. Stringari, C., et al., *Label-free separation of human embryonic stem cells and their differentiating progenies by phasor fluorescence lifetime microscopy*. *J Biomed Opt*, 2012. **17**(4): p. 046012.
125. Croce, A.C., et al., *Diagnostic potential of autofluorescence for an assisted intraoperative delineation of glioblastoma resection margins*. *Photochem Photobiol*, 2003. **77**(3): p. 309-18.
126. Xylas, J., et al., *Noninvasive assessment of mitochondrial organization in three-dimensional tissues reveals changes associated with cancer development*. *Int J Cancer*, 2015. **136**(2): p. 322-32.
127. Zhuo, S., et al., *Label-free monitoring of colonic cancer progression using multiphoton microscopy*. *Biomed Opt Express*, 2011. **2**(3): p. 615-9.
128. Boulesteix, T., et al., *Second-harmonic microscopy of unstained living cardiac myocytes: measurements of sarcomere length with 20-nm accuracy*. *Opt Lett*, 2004. **29**(17): p. 2031-3.
129. Freund, I. and M. Deutsch, *Second-harmonic microscopy of biological tissue*. *Opt Lett*, 1986. **11**(2): p. 94.
130. Chen, X., et al., *Second harmonic generation microscopy for quantitative analysis of collagen fibrillar structure*. *Nat Protoc*, 2012. **7**(4): p. 654-69.
131. Kniazeva, E., et al., *Quantification of local matrix deformations and mechanical properties during capillary morphogenesis in 3D*. *Integr Biol (Camb)*, 2012. **4**(4): p. 431-9.
132. Raub, C.B., et al., *Image correlation spectroscopy of multiphoton images correlates with collagen mechanical properties*. *Biophys J*, 2008. **94**(6): p. 2361-2373.
133. Robertson, C. and S.C. George, *Theory and practical recommendations for autocorrelation-based image correlation spectroscopy*. *J Biomed Opt*, 2012. **17**(8).
134. Eichhorn, S.J. and W.W. Sampson, *Statistical geometry of pores and statistics of porous nanofibrous assemblies*. *Journal of the Royal Society Interface*, 2005. **2**(4): p. 309-318.
135. Mir, S.M., B. Baggett, and U. Utzinger, *The efficacy of image correlation spectroscopy for characterization of the extracellular matrix*. *Biomed Opt Express*, 2012. **3**(2): p. 215-224.
136. Paesen, R., et al., *Polarization second harmonic generation by image correlation spectroscopy on collagen type I hydrogels*. *Acta Biomater*, 2014. **10**(5): p. 2036-42.
137. Deumens, R., et al., *Repairing injured peripheral nerves: Bridging the gap*. *Prog Neurobiol*, 2010. **92**(3): p. 245-76.

138. Hall, S.M., *The effect of inhibiting Schwann cell mitosis on the re-innervation of acellular autografts in the peripheral nervous system of the mouse*. *Neuropathology and Applied Neurobiology*, 1986. **12**(4): p. 401-14.
139. Ichihara, S., Y. Inada, and T. Nakamura, *Artificial nerve tubes and their application for repair of peripheral nerve injury: an update of current concepts*. *Injury*, 2008. **39 Suppl 4**: p. 29-39.
140. Gu, X., et al., *Construction of tissue engineered nerve grafts and their application in peripheral nerve regeneration*. *Progress in Neurobiology*, 2011. **93**(2): p. 204-30.
141. Nectow, A.R., K.G. Marra, and D.L. Kaplan, *Biomaterials for the development of peripheral nerve guidance conduits*. *Tissue Eng Part B Rev*, 2012. **18**(1): p. 40-50.
142. Brown, R.A. and J.B. Phillips, *Cell responses to biomimetic protein scaffolds used in tissue repair and engineering*. *International Review of Cytology*, 2007. **262**: p. 75-150.
143. Georgiou, M., et al., *Engineered neural tissue for peripheral nerve repair*. *Biomaterials*, 2013. **34**(30): p. 7335-7343.
144. Ren, Z., et al., *Role of stem cells in the regeneration and repair of peripheral nerves*. *Rev Neurosci*, 2012. **23**(2): p. 135-43.
145. Terenghi, G., M. Wiberg, and P.J. Kingham, *Chapter 21: Use of stem cells for improving nerve regeneration*. *Int Rev Neurobiol*, 2009. **87**: p. 393-403.
146. Javazon, E.H., K.J. Beggs, and A.W. Flake, *Mesenchymal stem cells: paradoxes of passaging*. *Experimental Hematology*, 2004. **32**(5): p. 414-25.
147. Ross, J.J. and C.M. Verfaillie, *Evaluation of neural plasticity in adult stem cells*. *Philosophical Transactions of the Royal Society of London. Series B: Biological Sciences*, 2008. **363**(1489): p. 199-205.
148. Chai, Y., et al., *Fate of the mammalian cranial neural crest during tooth and mandibular morphogenesis*. *Development*, 2000. **127**(8): p. 1671-9.
149. Graham, A., J. Begbie, and I. McGonnell, *Significance of the cranial neural crest*. *Developmental Dynamics*, 2004. **229**(1): p. 5-13.
150. Miletich, I. and P.T. Sharpe, *Neural crest contribution to mammalian tooth formation*. *Birth Defects Res C Embryo Today*, 2004. **72**(2): p. 200-12.
151. Thesleff, I. and T. Aberg, *Molecular regulation of tooth development*. *Bone*, 1999. **25**(1): p. 123-5.
152. Papaccio, G., et al., *Long-term cryopreservation of dental pulp stem cells (SBP-DPSCs) and their differentiated osteoblasts: a cell source for tissue repair*. *Journal of Cellular Physiology*, 2006. **208**(2): p. 319-25.

153. Martens, W., et al., *Dental stem cells and their promising role in neural regeneration: an update*. Clinical Oral Investigations, 2013. **17**(9): p. 1969-83.
154. Struys, T., et al., *Ultrastructural and immunocytochemical analysis of multilineage differentiated human dental pulp- and umbilical cord-derived mesenchymal stem cells*. Cells Tissues Organs, 2011. **193**(6): p. 366-78.
155. Dezawa, M., et al., *Sciatic nerve regeneration in rats induced by transplantation of in vitro differentiated bone-marrow stromal cells*. Eur J Neurosci, 2001. **14**(11): p. 1771-6.
156. Wei, Y., et al., *An improved method for isolating Schwann cells from postnatal rat sciatic nerves*. Cell and Tissue Research, 2009. **337**(3): p. 361-9.
157. Bretschneider, A., W. Burns, and A. Morrison, "*Pop-off*" *technic. The ultrastructure of paraffin-embedded sections*. American Journal of Clinical Pathology, 1981. **76**(4): p. 450-3.
158. Phillips, J.B. and R.A. Brown, *Self-aligning tissue growth guide*. International Patent WO2004087231, 2004.
159. Brown, R.A., et al., *Ultrarapid engineering of biomimetic materials and tissues: Fabrication of nano- and microstructures by plastic compression*. Advanced Functional Materials, 2005. **15**(11): p. 1762-1770.
160. Phillips, J.B. and R. Brown, *Micro-structured materials and mechanical cues in 3D collagen gels*. Methods Mol Biol, 2011. **695**: p. 183-96.
161. East, E., J.P. Golding, and J.B. Phillips, *A versatile 3D culture model facilitates monitoring of astrocytes undergoing reactive gliosis*. J Tissue Eng Regen Med, 2009. **3**(8): p. 634-46.
162. Wright, K.E., et al., *Peripheral neural cell sensitivity to mTHPC-mediated photodynamic therapy in a 3D in vitro model*. British Journal of Cancer, 2009. **101**(4): p. 658-65.
163. Kingham, P.J., et al., *Adipose-derived stem cells differentiate into a Schwann cell phenotype and promote neurite outgrowth in vitro*. Experimental Neurology, 2007. **207**(2): p. 267-74.
164. Mantovani, C., G. Terenghi, and S.G. Shawcross, *Isolation of adult stem cells and their differentiation to Schwann cells*. Methods in Molecular Biology, 2012. **916**: p. 47-57.
165. Ibarretxe, G., et al., *Neural crest stem cells from dental tissues: a new hope for dental and neural regeneration*. Stem Cells Int, 2012. **2012**: p. 103503.
166. Deng, W., et al., *In vitro differentiation of human marrow stromal cells into early progenitors of neural cells by conditions that increase intracellular cyclic AMP*. Biochemical and Biophysical Research Communications, 2001. **282**(1): p. 148-52.

167. Fraichard, A., et al., *In vitro differentiation of embryonic stem cells into glial cells and functional neurons*. Journal of Cell Science, 1995. **108 (Pt 10)**: p. 3181-8.
168. Gage, F.H., et al., *Survival and differentiation of adult neuronal progenitor cells transplanted to the adult brain*. Proceedings of the National Academy of Sciences of the United States of America, 1995. **92(25)**: p. 11879-83.
169. Frostick, S.P., Q. Yin, and G.J. Kemp, *Schwann cells, neurotrophic factors, and peripheral nerve regeneration*. Microsurgery, 1998. **18(7)**: p. 397-405.
170. Ribeiro-Resende, V.T., et al., *Strategies for inducing the formation of bands of Bungner in peripheral nerve regeneration*. Biomaterials, 2009. **30(29)**: p. 5251-9.
171. East, E., et al., *Alignment of astrocytes increases neuronal growth in three-dimensional collagen gels and is maintained following plastic compression to form a spinal cord repair conduit*. Tissue Eng Part A, 2010. **16(10)**: p. 3173-84.
172. Phillips, J.B., et al., *Neural tissue engineering: a self-organizing collagen guidance conduit*. Tissue Engineering, 2005. **11(9-10)**: p. 1611-7.
173. Sherman, D.L. and P.J. Brophy, *Mechanisms of axon ensheathment and myelin growth*. Nat Rev Neurosci, 2005. **6(9)**: p. 683-90.
174. Nichols, C.M., et al., *Effects of motor versus sensory nerve grafts on peripheral nerve regeneration*. Exp Neurol, 2004. **190(2)**: p. 347-55.
175. Siemionow, M. and G. Brzezicki, *Chapter 8: Current techniques and concepts in peripheral nerve repair*. Int Rev Neurobiol, 2009. **87**: p. 141-72.
176. Angius, D., et al., *A systematic review of animal models used to study nerve regeneration in tissue-engineered scaffolds*. Biomaterials, 2012. **33(32)**: p. 8034-9.
177. O'Rourke, C., et al., *Optimising contraction and alignment of cellular collagen hydrogels to achieve reliable and consistent engineered anisotropic tissue*. J Biomater Appl, 2015.
178. Martens, W., et al., *Human dental pulp stem cells can differentiate into Schwann cells and promote and guide neurite outgrowth in an aligned tissue-engineered collagen construct in vitro*. FASEB J, 2014. **28(4)**: p. 1634-43.
179. Hoeben, A., et al., *Vascular endothelial growth factor and angiogenesis*. Pharmacol Rev, 2004. **56(4)**: p. 549-80.
180. Rosenstein, J.M., J.M. Krum, and C. Ruhrberg, *VEGF in the nervous system*. Organogenesis, 2010. **6(2)**: p. 107-14.
181. Aranha, A.M., et al., *Hypoxia enhances the angiogenic potential of human dental pulp cells*. J Endod, 2010. **36(10)**: p. 1633-7.

182. Tran-Hung, L., et al., *Quantification of angiogenic growth factors released by human dental cells after injury*. Arch Oral Biol, 2008. **53**(1): p. 9-13.
183. Tran-Hung, L., S. Mathieu, and I. About, *Role of human pulp fibroblasts in angiogenesis*. J Dent Res, 2006. **85**(9): p. 819-23.
184. Karaoz, E., et al., *Human dental pulp stem cells demonstrate better neural and epithelial stem cell properties than bone marrow-derived mesenchymal stem cells*. Histochem Cell Biol, 2011. **136**(4): p. 455-73.
185. Hilkens, P., et al., *Pro-angiogenic impact of dental stem cells in vitro and in vivo*. Stem Cell Res, 2014. **12**(3): p. 778-90.
186. Hata, M., et al., *Transplantation of cultured dental pulp stem cells into the skeletal muscles ameliorated diabetic polyneuropathy: therapeutic plausibility of freshly isolated and cryopreserved dental pulp stem cells*. Stem Cell Res Ther, 2015. **6**: p. 162.
187. Rice, J.J., et al., *Engineering the regenerative microenvironment with biomaterials*. Adv Healthc Mater, 2013. **2**(1): p. 57-71.
188. Hamid, R., et al., *Comparison of alamar blue and MTT assays for high through-put screening*. Toxicol In Vitro, 2004. **18**(5): p. 703-10.
189. Patel, H.D., et al., *Comparison of the MTT and Alamar Blue assay for in vitro anti-cancer activity by testing of various chalcone and thiosemicarbazone derivatives*. International Journal of Pharma and Bio Sciences, 2013. **4**(2): p. 707-716.
190. Gruber, R., et al., *Bone marrow stromal cells can provide a local environment that favors migration and formation of tubular structures of endothelial cells*. Tissue Eng, 2005. **11**(5-6): p. 896-903.
191. Iohara, K., et al., *A novel stem cell source for vasculogenesis in ischemia: subfraction of side population cells from dental pulp*. Stem Cells, 2008. **26**(9): p. 2408-18.
192. Potapova, I.A., et al., *Mesenchymal stem cells support migration, extracellular matrix invasion, proliferation, and survival of endothelial cells in vitro*. Stem Cells, 2007. **25**(7): p. 1761-8.
193. Duffy, G.P., et al., *Bone marrow-derived mesenchymal stem cells promote angiogenic processes in a time- and dose-dependent manner in vitro*. Tissue Eng Part A, 2009. **15**(9): p. 2459-70.
194. Rampersad, S.N., *Multiple applications of Alamar Blue as an indicator of metabolic function and cellular health in cell viability bioassays*. Sensors (Basel), 2012. **12**(9): p. 12347-60.
195. Yadav, K., et al., *Cell proliferation assays*. eLS, 2014.
196. Georgiou, M., et al., *Engineered neural tissue with aligned, differentiated adipose-derived stem cells promotes peripheral nerve regeneration across a critical sized defect in rat sciatic nerve*. Biomaterials, 2015. **37**: p. 242-51.

197. Benowitz, L.I. and P.G. Popovich, *Inflammation and axon regeneration*. *Curr Opin Neurol*, 2011. **24**(6): p. 577-83.
198. Namavari, A., et al., *Cyclosporine immunomodulation retards regeneration of surgically transected corneal nerves*. *Invest Ophthalmol Vis Sci*, 2012. **53**(2): p. 732-40.
199. D'Arpa, S., et al., *Vascularized nerve "grafts": just a graft or a worthwhile procedure?* *Plast Aesthet Res*, 2015. **2**(4): p. 183-194.
200. Lind, R. and M.B. Wood, *Comparison of the pattern of early revascularization of conventional versus vascularized nerve grafts in the canine*. *J Reconstr Microsurg*, 1986. **2**(4): p. 229-34.
201. Penkert, G., W. Bini, and M. Samii, *Revascularization of nerve grafts: an experimental study*. *J Reconstr Microsurg*, 1988. **4**(4): p. 319-25.
202. Kingham, P.J., et al., *Stimulating the neurotrophic and angiogenic properties of human adipose-derived stem cells enhances nerve repair*. *Stem Cells Dev*, 2014. **23**(7): p. 741-54.
203. Krock, B.L., N. Skuli, and M.C. Simon, *Hypoxia-induced angiogenesis: good and evil*. *Genes Cancer*, 2011. **2**(12): p. 1117-33.
204. Best, T.J., et al., *Revascularization of peripheral nerve autografts and allografts*. *Plast Reconstr Surg*, 1999. **104**(1): p. 152-60.
205. Chalfoun, C., et al., *Primary nerve grafting: A study of revascularization*. *Microsurgery*, 2003. **23**(1): p. 60-5.
206. Langer, R. and J.P. Vacanti, *Tissue Engineering*. *Science*, 1993. **260**(5110): p. 920-926.
207. Fratzl, P. and R. Weinkamer, *Nature's hierarchical materials*. *Progress in Materials Science*, 2007. **52**(8): p. 1263-1334.
208. Van Der Rest, M., R. Garrone, and D. Herbage, *Collagen A family of proteins with many facets*, in *Advances In Molecular And Cell Biology; Extracellular Matrix*, E. Bittar and H. Kleinman, Editors. 1993, Elsevier. p. 1-67.
209. Freund, I., M. Deutsch, and A. Sprecher, *Connective-Tissue Polarity - Optical 2nd-Harmonic Microscopy, Crossed-Beam Summation, and Small-Angle Scattering in Rat-Tail Tendon*. *Biophys J*, 1986. **50**(4): p. 693-712.
210. RichardsKortum, R. and E. SevickMuraca, *Quantitative optical spectroscopy for tissue diagnosis*. *Annual Review of Physical Chemistry*, 1996. **47**: p. 555-606.
211. Brown, E., et al., *Dynamic imaging of collagen and its modulation in tumors in vivo using second-harmonic generation*. *Nature Medicine*, 2003. **9**(6): p. 796-800.
212. Campagnola, P., *Second harmonic generation imaging microscopy: applications to diseases diagnostics*. *Analytical Chemistry*, 2011. **83**(9): p. 3224-31.

213. Matcher, S.J., *Applications of SHG microscopy in tissue engineering*, in *Optical Techniques in Regenerative Medicine*. 2013, CRC Press. p. 82-88.
214. Vielreicher, M., et al., *Taking a deep look: modern microscopy technologies to optimize the design and functionality of biocompatible scaffolds for tissue engineering in regenerative medicine*. *Journal of the Royal Society Interface*, 2013. **10**(86).
215. Grinnell, F. and W.M. Petroll, *Cell motility and mechanics in three-dimensional collagen matrices*. *Annual Review of Cell and Developmental Biology*, 2010. **26**: p. 335-61.
216. Brown, R.A., *In the beginning there were soft collagen-cell gels: towards better 3D connective tissue models?* *Experimental Cell Research*, 2013. **319**(16): p. 2460-2469.
217. Ahearne, M., *Introduction to cell-hydrogel mechanosensing*. *Interface Focus*, 2014. **4**(2).
218. Fernandez, P. and A.R. Bausch, *The compaction of gels by cells: a case of collective mechanical activity*. *Integr Biol (Camb)*, 2009. **1**(3): p. 252-9.
219. Matteini, P., et al., *Photothermally-induced disordered patterns of corneal collagen revealed by SHG imaging*. *Opt Express*, 2009. **17**(6): p. 4868-78.
220. Rao, R.A., M.R. Mehta, and K.C. Toussaint, Jr., *Fourier transform-second-harmonic generation imaging of biological tissues*. *Opt Express*, 2009. **17**(17): p. 14534-42.
221. Ghazaryan, A., et al., *Analysis of collagen fiber domain organization by Fourier second harmonic generation microscopy*. *J Biomed Opt*, 2013. **18**(3): p. 31105.
222. Gjorevski, N. and C.M. Nelson, *Mapping of mechanical strains and stresses around quiescent engineered three-dimensional epithelial tissues*. *Biophys J*, 2012. **103**(1): p. 152-62.
223. Winer, J.P., S. Oake, and P.A. Janmey, *Non-linear elasticity of extracellular matrices enables contractile cells to communicate local position and orientation*. *PLoS One*, 2009. **4**(7): p. e6382.
224. White, D.J., et al., *The collagen receptor subfamily of the integrins*. *Int J Biochem Cell Biol*, 2004. **36**(8): p. 1405-10.
225. Docheva, D., et al., *Human mesenchymal stem cells in contact with their environment: surface characteristics and the integrin system*. *J Cell Mol Med*, 2007. **11**(1): p. 21-38.
226. Milner, R., et al., *Division of labor of Schwann cell integrins during migration on peripheral nerve extracellular matrix ligands*. *Dev Biol*, 1997. **185**(2): p. 215-28.
227. Vader, D., et al., *Strain-induced alignment in collagen gels*. *PLoS One*, 2009. **4**(6): p. e5902.

228. Varas, L., et al., *Alpha10 integrin expression is up-regulated on fibroblast growth factor-2-treated mesenchymal stem cells with improved chondrogenic differentiation potential*. *Stem Cells Dev*, 2007. **16**(6): p. 965-78.
229. Chastain, S.R., et al., *Adhesion of mesenchymal stem cells to polymer scaffolds occurs via distinct ECM ligands and controls their osteogenic differentiation*. *J Biomed Mater Res A*, 2006. **78**(1): p. 73-85.
230. Foster, L.J., et al., *Differential expression profiling of membrane proteins by quantitative proteomics in a human mesenchymal stem cell line undergoing osteoblast differentiation*. *Stem Cells*, 2005. **23**(9): p. 1367-77.
231. Majumdar, M.K., et al., *Characterization and functionality of cell surface molecules on human mesenchymal stem cells*. *J Biomed Sci*, 2003. **10**(2): p. 228-41.
232. Heckmann, L., et al., *Mesenchymal progenitor cells communicate via alpha and beta integrins with a three-dimensional collagen type I matrix*. *Cells Tissues Organs*, 2006. **182**(3-4): p. 143-54.
233. Popov, C., et al., *Integrins alpha2beta1 and alpha11beta1 regulate the survival of mesenchymal stem cells on collagen I*. *Cell Death Dis*, 2011. **2**: p. e186.
234. Gronthos, S., et al., *Integrin-mediated interactions between human bone marrow stromal precursor cells and the extracellular matrix*. *Bone*, 2001. **28**(2): p. 174-81.
235. Rider, D.A., et al., *Selection using the alpha-1 integrin (CD49a) enhances the multipotentiality of the mesenchymal stem cell population from heterogeneous bone marrow stromal cells*. *J Mol Histol*, 2007. **38**(5): p. 449-58.
236. Popova, S.N., et al., *Alpha11 beta1 integrin-dependent regulation of periodontal ligament function in the erupting mouse incisor*. *Mol Cell Biol*, 2007. **27**(12): p. 4306-16.
237. Mimura, T., et al., *Peripheral nerve regeneration by transplantation of bone marrow stromal cell-derived Schwann cells in adult rats*. *J Neurosurg*, 2004. **101**(5): p. 806-12.
238. Brohlin, M., et al., *Characterisation of human mesenchymal stem cells following differentiation into Schwann cell-like cells*. *Neurosci Res*, 2009. **64**(1): p. 41-9.
239. Mahay, D., G. Terenghi, and S.G. Shawcross, *Schwann cell mediated trophic effects by differentiated mesenchymal stem cells*. *Exp Cell Res*, 2008. **314**(14): p. 2692-701.
240. Wang, X., et al., *Schwann-like mesenchymal stem cells within vein graft facilitate facial nerve regeneration and remyelination*. *Brain Res*, 2011. **1383**: p. 71-80.

241. Shimizu, S., et al., *Peripheral nerve regeneration by the in vitro differentiated-human bone marrow stromal cells with Schwann cell property*. Biochem Biophys Res Commun, 2007. **359**(4): p. 915-20.
242. Wakao, S., et al., *Long-term observation of auto-cell transplantation in non-human primate reveals safety and efficiency of bone marrow stromal cell-derived Schwann cells in peripheral nerve regeneration*. Exp Neurol, 2010. **223**(2): p. 537-47.
243. Radtke, C., et al., *Peripheral glial cell differentiation from neurospheres derived from adipose mesenchymal stem cells*. Int J Dev Neurosci, 2009. **27**(8): p. 817-23.
244. Razavi, S., et al., *Efficient transdifferentiation of human adipose-derived stem cells into Schwann-like cells: A promise for treatment of demyelinating diseases*. Adv Biomed Res, 2012. **1**: p. 12.
245. Matsuse, D., et al., *Human umbilical cord-derived mesenchymal stromal cells differentiate into functional Schwann cells that sustain peripheral nerve regeneration*. J Neuropathol Exp Neurol, 2010. **69**(9): p. 973-85.
246. Peng, J., et al., *Human umbilical cord Wharton's jelly-derived mesenchymal stem cells differentiate into a Schwann-cell phenotype and promote neurite outgrowth in vitro*. Brain Res Bull, 2011. **84**(3): p. 235-43.
247. Xu, Q., et al., *In vitro and in vivo magnetic resonance tracking of Sinerem-labeled human umbilical mesenchymal stromal cell-derived Schwann cells*. Cell Mol Neurobiol, 2011. **31**(3): p. 365-75.
248. Wakao, S., D. Matsuse, and M. Dezawa, *Mesenchymal stem cells as a source of Schwann cells: their anticipated use in peripheral nerve regeneration*. Cells Tissues Organs, 2014. **200**(1): p. 31-41.
249. Brushart, T.M., et al., *Schwann cell phenotype is regulated by axon modality and central-peripheral location, and persists in vitro*. Exp Neurol, 2013. **247**: p. 272-81.
250. Gupta, R., et al., *Schwann cells upregulate vascular endothelial growth factor secondary to chronic nerve compression injury*. Muscle Nerve, 2005. **31**(4): p. 452-60.
251. Guaiquil, V.H., et al., *VEGF-B selectively regenerates injured peripheral neurons and restores sensory and trophic functions*. Proc Natl Acad Sci U S A, 2014. **111**(48): p. 17272-7.
252. Pan, Z., et al., *Vascular endothelial growth factor promotes anatomical and functional recovery of injured peripheral nerves in the avascular cornea*. FASEB J, 2013. **27**(7): p. 2756-67.
253. Sondell, M., G. Lundborg, and M. Kanje, *Vascular endothelial growth factor has neurotrophic activity and stimulates axonal outgrowth, enhancing cell survival and Schwann cell proliferation in the peripheral nervous system*. J Neurosci, 1999. **19**(14): p. 5731-40.

254. Berti, C., et al., *Role of integrins in peripheral nerves and hereditary neuropathies*. Neuromolecular Med, 2006. **8**(1-2): p. 191-204.
255. Previtali, S.C., et al., *Expression of laminin receptors in schwann cell differentiation: evidence for distinct roles*. J Neurosci, 2003. **23**(13): p. 5520-30.
256. Fernandez-Valle, C., et al., *Actin plays a role in both changes in cell shape and gene-expression associated with Schwann cell myelination*. J Neurosci, 1997. **17**(1): p. 241-50.
257. Stewart, H.J., et al., *Expression and regulation of alpha1beta1 integrin in Schwann cells*. J Neurobiol, 1997. **33**(7): p. 914-28.
258. Toyota, B., S. Carbonetto, and S. David, *A dual laminin/collagen receptor acts in peripheral nerve regeneration*. Proc Natl Acad Sci U S A, 1990. **87**(4): p. 1319-22.
259. Johnson, P.J., et al., *Tissue engineered constructs for peripheral nerve surgery*. Eur Surg, 2013. **45**(3).
260. Marquardt, L.M. and S.E. Sakiyama-Elbert, *Engineering peripheral nerve repair*. Curr Opin Biotechnol, 2013. **24**(5): p. 887-92.
261. Fu, K.Y., et al., *Sciatic nerve regeneration by microporous nerve conduits seeded with glial cell line-derived neurotrophic factor or brain-derived neurotrophic factor gene transfected neural stem cells*. Artif Organs, 2011. **35**(4): p. 363-72.
262. Murakami, T., et al., *Transplanted neuronal progenitor cells in a peripheral nerve gap promote nerve repair*. Brain Research, 2003. **974**(1-2): p. 17-24.
263. Nijhuis, T.H., et al., *Natural conduits for bridging a 15-mm nerve defect: comparison of the vein supported by muscle and bone marrow stromal cells with a nerve autograft*. J Plast Reconstr Aesthet Surg, 2013. **66**(2): p. 251-9.
264. Zhao, Z., et al., *Improvement in nerve regeneration through a decellularized nerve graft by supplementation with bone marrow stromal cells in fibrin*. Cell Transplant, 2014. **23**(1): p. 97-110.
265. Leong, N.L., et al., *Athymic rat model for evaluation of engineered anterior cruciate ligament grafts*. J Vis Exp, 2015. **26**(97).
266. Rolstad, B., *The athymic nude rat: an animal experimental model to reveal novel aspects of innate immune responses?* Immunological Reviews, 2001. **184**: p. 136-144.
267. Raub, C.B., et al., *Predicting bulk mechanical properties of cellularized collagen gels using multiphoton microscopy*. Acta Biomater, 2010. **6**(12): p. 4657-65.
268. Provenzano, P.P., et al., *Nonlinear Optical Imaging of Cellular Processes in Breast Cancer*. Microscopy and Microanalysis, 2008. **14**(6): p. 532-548.

Reference list

269. Thrasivoulou, C., et al., *Optical delineation of human malignant melanoma using second harmonic imaging of collagen*. Biomed Opt Express, 2011. **2**(5): p. 1282-95.
270. Wolf, K. and P. Friedl, *Extracellular matrix determinants of proteolytic and non-proteolytic cell migration*. Trends in Cell Biology, 2011. **21**(12): p. 736-744.
271. Gailit, J., et al., *Platelet-derived growth factor and inflammatory cytokines have differential effects on the expression of integrins alpha 1 beta 1 and alpha 5 beta 1 by human dermal fibroblasts in vitro*. Journal of Cellular Physiology, 1996. **169**(2): p. 281-289.
272. Du, J., et al., *Integrin activation and internalization on soft ECM as a mechanism of induction of stem cell differentiation by ECM elasticity*. Proceedings of the National Academy of Sciences of the United States of America, 2011. **108**(23): p. 9466-9471.
273. Millard, M., S. Odde, and N. Neamati, *Integrin Targeted Therapeutics*. Theranostics, 2011. **1**: p. 154-188.

Curriculum Vitae

Kathleen Sanen werd geboren op 7 september 1988 te Hasselt. In 2006 behaalde ze haar diploma Algemeen Secundair Onderwijs (ASO) in de studierichting wetenschappen-wiskunde (6u) aan het Virga-Jessecollege te Hasselt. In hetzelfde jaar startte ze haar hogere studies aan de Universiteit Hasselt/transnationale universiteit Limburg (tUL) waar ze in 2011 met grote onderscheiding afstudeerde als master in de Biomedische Wetenschappen. Haar eindwerk, getiteld 'Differential involvement of COX-1 and COX-2 in chondrogenic differentiation' werd uitgevoerd in het departement Orthopaedic Surgery van Maastricht University Medical Center onder supervisie van dr. Tim J.M. Welting. Vervolgens startte ze in september 2011 haar doctoraat in de groep Biofysica aan het Biomedisch Onderzoeksinstituut van de Universiteit Hasselt. Tijdens deze periode volgde ze verschillende cursussen in het kader van de Doctoral School for Medicine and Life Sciences zoals project management, biosafety en effective writing for life sciences research, en was ze actief als lid in de onderwijsteams van verschillende vakken in de opleidingen Biomedische Wetenschappen, Geneeskunde en Biologie. Verder hielp ze mee aan de organisatie van het tweede μ FIBR symposium (2012) en behaalde ze een FWO aspirantenmandaat in 2013 en verschillende reisbeurzen. De resultaten die werden bekomen tijdens dit doctoraat werden deels gepubliceerd in internationale tijdschriften en werden tevens gepresenteerd op verschillende (inter)nationale meetings. Tijdens het symposium "Cell-based therapies in CNS pathology" aan de Universiteit Hasselt in 2013 ontving ze hiervoor de prijs voor beste mondelinge presentatie.

Bibliography

Publications

- Label-free mapping of microstructural organisation in self-aligning cellular collagen hydrogels using image correlation spectroscopy.
Sanen K, Paesen R, Luyck S, Phillips J, Lambrichts I, Martens W, Ameloot M.
Acta Biomaterialia (2015), doi:
<http://dx.doi.org/10.1016/j.actbio.2015.10.047>. IF = 6.025
- Human dental pulp stem cells can differentiate into Schwann cells and promote and guide neurite outgrowth in an aligned tissue-engineered collagen construct in vitro.
Martens W*, **Sanen K***, Georgiou M, Struys T, Bronckaers A, Ameloot M, Phillips J, Lambrichts I.
FASEB J. 2014 Apr;28(4):1634-43. IF(2013)=5.480
- Polarization second harmonic generation by image correlation spectroscopy on collagen type I hydrogels.
Paesen R, **Sanen K**, Smisdom N, Michiels L, Ameloot M.
Acta Biomater. 2014 May;10(5):2036-42. IF(2013)=5.684
- Impact of differently modified nanocrystalline diamond on the growth of neuroblastoma cells.
Vaitkuvienė A, McDonald M, Vahidpour F, Noben JP, **Sanen K**, Ameloot M, Ratautaite V, Kasetė V, Biziulevičienė G, Ramanavičienė A, Nesladek M, Ramanavicius A.
N Biotechnol. 2015 Jan 25;32(1):7-12. IF(2013)=2.884
- Impact of diamond nanoparticles on neural cells.
Vaitkuvienė A, Ratautaite V, Ramanavičienė A, **Sanen K**, Rik Paesen, Marcel Ameloot, Vladimira Petrakova, Matthew McDonald, Vahidpour F, Kasetė V, Ramanauskaite G, Biziulevičienė G, Nesladek M, Ramanavicius A.
Mol Cell Probes. 2015 Feb;29(1):25-30. IF(2013)=1.859

Oral presentations

- Label-free Optical Imaging in Biomedical Research.
Sanen K, Paesen R, Smisdom N, Michiels L, Ameloot M.
Biophysics school on bioimaging. Liège, Belgium. 18-19/04/2012.
- Introduction to dental pulp stem cells and label-free optical imaging.
Sanen K*, Martens W*, Lambrichts I, Ameloot M.
Invited Research Seminar, the Open University Milton Keynes, UK. 18/02/2013.
- Engineered neural tissue containing Schwann-cell like cells differentiated from dental pulp stem cells support directed neurite outgrowth in vitro.
Sanen K*, Martens W*, Georgiou M, Phillips J, Lambrichts I, Ameloot M.
Cell-based therapies in CNS pathology. Hasselt, Belgium. 12/04/2013.
- Label free optical imaging of engineered neural tissue formation by second harmonic signals from collagen type I.
Sanen K, Paesen R, Martens W, Lambrichts I, Phillips J, Ameloot M.
18th International Microscopy congress (IMC 2014). Prague, Czech Republic. 07-12/09/2014.

Selected poster presentations

- Exploring the potential of label-free optical techniques to characterize living Schwann cell differentiated human dental pulp stem cells.
Sanen K, Martens W, Smisdom N, Lambrichts I, Ameloot M.
Annual Dutch Meeting on Molecular and Cellular Biophysics. Veldhoven, the Netherlands. 01-02/10/2012.
- Aligned schwann cell differentiated human dental pulp stem cells to direct neurite outgrowth.
Sanen K*, Martens W*, Georgiou M, Phillips J, Lambrichts I, Ameloot M.
XI European Meeting on Glial Cells in Health and Disease (GLIA 2013). Berlin, Germany. 02-06/07/2013.
- Engineered neural tissue containing aligned Schwann cell-like cells differentiated from dental pulp stem cells supports directed neurite outgrowth in vitro.
Martens W*, **Sanen K***, Georgiou M, Struys T, Bronckaers A, Ameloot M, Phillips J, Lambrichts I.

2nd International symposium on peripheral nerve regeneration (ISPNR 2014). Torino, Italy. 23-25/01/2014

- Label-free monitoring of cell-seeded collagen type I hydrogels reveals marked changes in extracellular architecture over time.

Sanen K, Paesen R, Martens W, Luyck S, Phillips J, Lambrechts I, Ameloot M. *Tissue and cell engineering society (TCES 2015). Southampton, UK. 19-21/07/2015*

Best oral presentation award

- Engineered neural tissue containing Schwann-cell like cells differentiated from dental pulp stem cells support directed neurite outgrowth in vitro.

Sanen K*, Martens W*, Georgiou M, Phillips J, Lambrechts I, Ameloot M. *Cell-based therapies in CNS pathology. Hasselt, Belgium. 12/04/2013.*

Bursaries

- Hasselt University Doctoral School and Human Resources grant to attend the 3rd TERMIS World Congress 2012 in Vienna, Austria.
- FWO Short Stay Abroad to develop engineered neural tissue constructs using DPSCs at the Open University Milton Keynes, UK in February 2013.
- FWO PhD Fellowship entitled "Nerve regeneration by hDPSCs in hydrogel based scaffolds: characterization by label-free optical imaging" for 2 x 2 years starting at October 1, 2013.
- Boehringer Ingelheim Fonds travel grant for short stay abroad to perform in vivo experiments at the Open University Milton Keynes, UK in July 2013.
- European Microscopy Society grant to attend the 18th International Microscopy congress, IMC 2014 in Prague, Czech Republic.

Dankwoord

Eind-de-lijk! Laat nu net het allerlaaste schrijfsel van mijn doctoraatsthesis het hoofdstukje zijn dat effectief gelezen wordt door een significant aantal mensen ☺ En met rede, want er zijn veel mensen die mij de afgelopen jaren gesteund hebben en dus een dikke dankjewel verdienen!

Allereerst een woord van dank aan mijn promotor, **Prof. dr. Marcel Ameloot**. Marcel, toen ik mijn doctoraat mocht beginnen in de groep Biofysica van BIOMED, had u vast niet gedacht dat mijn boekje er zo biologisch uit zou zien. Ik wil u dan ook bedanken voor de vrijheid die u me hebt gegeven in het zoeken van een onderwerp waar ik mijn biomedische achtergrond op kon botvieren en de microscopische expertise van de groep op kon toepassen. Steeds kon ik bij u terecht met mijn vragen en bezorgdheden, en hoewel ik al gauw doorhad dat mijn figuren meestal te klein en titels vaak te kort waren, heeft u altijd de tijd genomen om mijn abstracts, artikels en beursaanvragen grondig na te lezen, waarvoor dank. En hoewel bescheidenheid siert, mogen uw Flintstone-evenarende bowlingvaardigheden best wat vaker in de verf gezet worden!

Ook mijn co-promotor, **Prof. dr. Ivo Lambrichts**, wil ik graag bedanken. Ivo, uw enthousiasme over dit project was (en is nog steeds) onvoorwaardelijk. Soms kon u dan ook gewoon niet wachten tot Wendy of ik tijd hadden om naar de elektronenmicroscop of de Mirax te gaan, en ging u zelf alvast even stiekem foto's nemen van onze cellen om ons vervolgens per email te "teasen" met de leukste en mooiste plaatjes – met succes! Ook bedankt voor de wetenschappelijke brainstormsessies en suggesties voor nieuwe experimenten of projecten. Ik ben er zeker van dat dentale pulpa stamcellen een mooie toekomst hebben onder uw supervisie.

I would also like to thank the **members of the jury** for critically reviewing my manuscript. A special word of gratitude to **dr. James Phillips** for his hospitality when visiting the Open University in Milton Keynes and University College London. I hope this very nice collaboration can be continued for many more years.

Verder wil ik **BioMIMedics, het FWO, het Boehringer Ingelheim Fonds, de Doctoral School van UHasselt en de European Microscopy Society** bedanken voor hun financiële steun tijdens mijn doctoraat.

Toen ik de Biofysica groep vervoegde, kwam ik terecht op de bureau van **Nick, Ben, Kristof en Rik**. In het begin moest ik dan ook letterlijk mijn mannetje staan, want hun initiële voornemen om 'het vanaf nu deftig te houden o.w.v. vrouwelijke aanwezigheid' werd al na één dag opgeschort. Als de flauwe moppen of de game-/sportanalyses me even te veel dreigden te worden, gaf **Miha** me steenvast een teken van I-know-how-you-feel-knipoog-of-oogrol. De eerste spelltjesavonden en teambuildings werden het leven ingeblazen, een traditie die ook het huidige Biofysica team (versterkt door **Sarah, Hannelore, Eli, Bart en Srujan**) in ere houdt. Bowlingen, boerengolfen, karten, lasergamen, botsvoetballen, walkie talkie fietsen,... We hebben samen toch veel plezier gehad! Dankzij de fijne sfeer in de groep was een mankement aan de confocale of een zoveelste mislukt experiment wat draagbaarder, bedankt daarvoor!

Hannelore en Eli, sorry voor mijn gezaag over artikels die te lang wegblijven en thesissen die niet vanzelf geschreven worden, en dankjewel voor jullie steun! Wat had ik toch zonder jullie moeten doen ☺. **Sarah**, heel veel succes met je thesis en toekomstig onderzoek, je gaat dat goed doen! **Nick**, voor alle keren dat ik een U Hasselt dienstwagenprobleem had: merci voor je hulp! **Daniel**, thanks for the out-of-the-box scientific discussions, good laughs and Czech tourism information. FYI: the Hasseltse Jeneverfeesten of 2016 are planned on October 15-16 ☺. **Rik en Kristof**, ik heb dan wel geen foto's (meer) van het congres in Praag, maar vergeten zal ik het niet gauw. Mercikes voor de vele leuke momenten die week! Rik, zonder u zou hoofdstuk 4 in dit boekje er niet zijn geweest. Hoewel ik niet heb kunnen volhouden dat ik nooit iets met MATLAB te maken wou hebben, heb jij gezorgd voor het programmeren en het maken van een Kathleen-vriendelijk interface – héél erg bedankt daarvoor!! **Martijn** (geen Biofysica-member, maar toch 'part of the gang'): jij weet wetenschap en humor te combineren als geen ander - merci voor de leuke pauzes!

Wendy, wat ben ik blij dat we zo nauw hebben mogen samenwerken! Je hebt me als grondlegger van dit project heel veel dingen geleerd en ik kon altijd bij je terecht met wetenschappelijke vragen. Maar ook buiten het labo kon ik op je rekenen: je mentale steun tijdens mijn eerste vlucht (STRESS!!), de urenlange babbels tijdens de vele Eurostar-ritten, de culturele uitstapjes op congres, het gedeelde "we-bevriezen-hier-want-de-chauffage-is-al-een-week-stuk" leed in

Milton Keynes, de solden-shoppings in Londen, enz. Wat was ik vereerd toen je me vroeg om te helpen met het haken van de uiltjes voor de suikerbonen van Lies! Zelfs na je vertrek op BIOMED (*klein paniekje*) stond je steeds voor me klaar, bedankt daarvoor! Ik ben er zeker van dat je met je met je passie voor onderwijs heel wat leerlingen warm kan maken voor biomedische wetenschappen en hoop dat we regelmatig kunnen blijven afspreken! **Petra H**, dankjewel voor je hulp/tips als ik weer eens vragen had over mijn boekje of verdediging. Ook gingen de uren in de CK12 een stuk sneller voorbij met jou, **Pascal, Jessica, Stefanie en Annelies** als gespreks- en celkweekpartners ☺. **Tim**, ik heb je de afgelopen maanden wat beter leren kennen en ben ervan overtuigd dat dit onderzoek in goede handen is bij jou. Veel succes ermee! **Nathalie**, tijdens je spinninglessen bedacht ik me wel eens dat er echt wel ergere dingen waren dan besmette cellen of mislukte PCRs... Grapje he! Dikke merci voor de leuke sportieve intermezzo's!

Omdat Biofysica de naam heeft een kluizenaarsleven te leiden in de kelder, begaf ik mij regelmatig naar hoger gelegen BIOMED-oorden om wat te 'socializen'. **Quirine**, jij hebt me vanaf dag 1 betrokken bij vanalles en nog wat. We hebben heel wat creatieve projectjes uitgewisseld (arts and crafts for the win, yeah!) en zijn zelfs een jaartje bureaugenootjes geweest. Ik heb meermaals de slappe lach gehad als je een conversatie van je kinderen met veel inleving navertelde, maar kon ook altijd bij je terecht met mijn verhaal. Bedankt en je weet: Alles komt altijd goed! **Sophie en Nina**, mede-organisatrices van μ FiBR 2012 – dat hebben we toen toch goed gedaan met ons drietjes he! Jullie zijn ook altijd te vinden voor een toffe babbel, een feestje, een beauty-night of een rondje karaoke. Samen met **Silke, Dorien en Winde** is ambiance verzekerd, dus laten we dat vooral blijven doen! Sophie, ik ben er zeker van dat jij over 2 jaar een pracht van een doctoraat zal afleveren, keep up the good work! **Petra B**, je enthousiasme lijkt wel onuitputtelijk en werkt vaak (neen, niet altijd...) aanstekelijk ☺ Bedankt ook voor je hulp met het maken van oplossingen en het opsporen van verdwenen labostuff. Ook een welgemeende dankjewel aan alle andere BIOMED collega's voor hun bijdrage en de gezellige en sportieve middagpauze's!

En de lijst gaat maar door: een dikke merci ook aan **Rosette, Jo, Leen, Igna, Katrien, Christel en Kim** voor de algemene introducties en troubleshooting van

protocols, aan **Jeanine** voor alle tips en tricks over immunokleuringen, aan **Marc** voor het snijden en contrasteren van véle coupes en je elektronenmicroscopereddingsacties, aan **Regine** voor het onderhouden van de voorraad zuiver glaswerk en het steriliseren van talloze tipjesdozen, aan **Joke, Eline en Paul** voor alle hulp in het animalium, aan **Rani en Veronique** voor alle administratieve ondersteuning, aan **Jean, Hilde en Jessica** voor het regelen en beheren van de financiën, aan **Kim en Stefanie** voor de hulp met onder andere Doctoral School formulieren en aan **Johan** voor het ontrafelen van mijn totaal niet-technische uitleg of tekeningen zodat ik custom-made tools van je kreeg die me enorm hebben geholpen met het uitvoeren van mijn experimenten!

Aan mijn ex-stagestudenten **Sander, Joren, Elke en Sebastiaan**: jullie hebben zeker jullie steentje bijgedragen aan dit doctoraat. Succes met jullie verdere opleiding/job en misschien komen we elkaar nog eens tegen ☺.

Melanie, Caitriona, Michelle and Elise, thanks for warm welcome in MK, the help in the lab, the numerous pub visits and the fun trip to Woburn Sarafi Park!

Omdat de boog natuurlijk niet altijd gespannen kan staan wil ik graag mijn vrienden en familie bedanken voor hun onvoorwaardelijke steun tijdens mijn doctoraat. **Ine, Ellen, Wendy, Muriel, Lise, Carola en Marion**, we kennen elkaar al een hele tijd en zouden ondertussen boeken kunnen schrijven over wat we al allemaal meegemaakt hebben ☺. Dankjewel voor jullie luisterend oor en voor de talloze uitstapjes, etentjes, spelletjesavonden en gezellig babbels!

De **Boezeroenen**... Om als 'buitenstaander' in zo een hechte vriendengroep opgenomen te worden, is heel bijzonder! De fijne oefenstondes en muziekgroeprepetities met aansluitende gezellige cafetaria-avonden/nachten, de demo-reizen, de themafeesjes (ref: Swammybal), enz. heeft zeker voor de nodige afleiding gezorgd, merci daarvoor!

Ook zangbuddie **Stefanie** en de rest van **Popkoor Horlecante**: de repetities op maandagavond waren vaak de perfecte uitlaatklep – zingen ontstrest écht!

Bram, Dieter, Lukas en Sita: dankjewel voor de superchille en zeer memorabele hitchhiking-couchsurfing-Denemarken-roadtrip!

Lieve **tantes, nonkels, neven en nichten**, voor onze "samen" momenten geldt: kwaliteit boven kwantiteit! Gelukkig doet zot zijn geen zeer ☺. **Oma en moemoe**, ik vind het súper dat jullie er vandaag bij zijn, dankjewel!

De laatste pagina, dus tijd voor de belangrijkste mensen in mijn leven...

Matthias, met je humor wist je me af te leiden als ik weer eens aan het piekeren was over vreemde laboresultaten, en ik heb meer dan eens de overwinning aan mijn neus voorbij moeten laten gaan omdat ik je tactische 'moves' tijdens gezelschapsspelen probeerde te doorgronden. Ik ben dan ook heel benieuwd naar de definitieve versie van je eigen ontworpen board game, waarvoor ik nu meer tijd ga hebben om het te spelen ☺!

Aline, jij lijkt elke week wel iets te beleven dat rechtstreeks uit Geronimo Stilton boeken komt ☺ Met je eigen one-liners en je enthousiasme over je schattige maar eigenzinnige huisdiertjes zorgde je al voor ontelbare fijne en gezellige momenten! Je bent dan wel mijn kleine zus, maar je bent echt mijn groot voorbeeld! **Michaël**, ik was heel vereerd dat ik je verlovingsringshoppende partner-in-crime mocht zijn! Binnenkort ben je officieel mijn schoonbroer, ik kijk er al naar uit ☺.

En over 'schoonfamilie' gesproken: **Linda, Eric, Rosalien, Sander en Berbe**: bedankt om mij op te nemen in jullie familie en voor jullie bemoedigende woorden!

Mama en papa, een héle dikke merci voor alle steun de afgelopen jaren. Alles in het Engels leren, 8 weken pure chemie terwijl ik toch voor *BIO*medische had gekozen, 3u durende sneeuwritten naar Maastricht tijdens mijn seniorstage, nachtje doordoen voor mijn eerste FWO-aanvraag, eenzaamheid en ijskoude handen tijdens lange confocale experimenten,... Jullie hebben elk klaagje en zaagje aanhoord, mij gemotiveerd en met raad en daad bijgestaan. Bedankt voor alle kansen die jullie mij gegeven hebben en voor de warme en gezellige thuis!

Maarten, je hebt mij de afgelopen weken vaak gezegd dat je geen bijdrage hebt gehad aan mijn doctoraat, maar niets is minder waar! Je nuchtere kijk op zaken, je begrip voor (en hulp tijdens) het vele avond- en weekendwerk, je luisterend oor, je enthousiasme over mijn stamcelletjes, je geduld (!!), je kleine en grote verrassingen om mijn gedachten te verzetten, je troostende en motiverende woorden, je oneindige inspanningen om zoveel mogelijk van Delft naar huis te komen,... Zonder jou was ik hier niet geraakt! Je steunt me in alles wat ik doe en maakt mij altijd aan het lachen, zelfs met je flauwe mopjes ☺. Bedankt lieverd, gewoon om te zijn wie je bent. Ik hou van je!